UQAC

Université du Québec à Chicoutimi

Precipitation behaviors of Mn-bearing dispersoids and $Al_3(Sc,Zr)$ precipitates and their impacts on the microstructure and mechanical properties of rolled Al-Mg-Mn 5xxx alloys

By

Ahmed Algendy

Under supervision of Prof. X.-Grant Chen and co-supervision of Prof. Kun Liu

Manuscript-Based Thesis Presented to Université du Québec à Chicoutimi in Partial Fulfillment of the Requirements for the Degree of Doctor of Philosophy Ph.D.

Defended on 25 October 2022

BOARD OF EXAMINERS:

Professor Dilip Sarkar, department of Applied Sciences at UQAC, President of the board of examiners
Dr. Alexandre Maltais, Rio Tinto Aluminum, Saguenay, Quebec, External Member of examiners
Professor Emad Elgallad, department of Applied Sciences at UQAC, Internal Member of examiners
Professor X.-Grant Chen, department of Applied Sciences at UQAC, Internal Member of examiners
Professor Kun Liu, department of Applied Sciences at UQAC, Internal Member of examiners

Québec, Canada

Comportement des précipitations des dispersoïdes Mn et des précipités $Al_3(Sc,Zr)$ et leurs impacts sur la microstructure et les propriétés mécaniques des alliages Al-Mg-Mn 5xxx laminés

Résumé

La grande exigence technologique au développement d'une nouvelle génération d'alliages d'aluminium légers est significativement augmentée, en particulier dans les applications qui servent à des températures élevées. Par conséquent, l'amélioration des propriétés mécaniques à des températures élevées s'avère un défi à relever. Les alliages Al-Mg-Mn 5xxx sont l'un des candidats potentiels pour des applications à haute température pour le fait que son durcissement primaire par solution solide de Mg dans l'alliage n'est pas susceptible d'être affecté à haute température. En outre, le renforcement par dispersion est considéré comme une voie prometteuse pour améliorer les propriétés mécaniques des alliages non traitables thermiquement, en particulier à haute température. Par conséquent, dans cette étude, la formation de dispersoïdes et l'évolution des propriétés mécaniques à des températures ambiantes et élevées en modifiant les traitements thermiques et le microalliage avec Sc et Zr dans les alliages Al-Mg-Mn 5xxx ont été étudiés. Le présent travail est divisé sur des parties, comme le suivant:

Dans la première partie, le comportement de précipitation des dispersoïdes en Mn dans un alliage Al-5% Mg-0,8% Mn après différents traitements thermiques à une/plusieurs étapes et leur influence sur les performances de laminage ainsi que sur les propriétés de traction a été évalué. Les résultats ont montré que la conductivité électrique (CE) et la microdureté (HV) ont considérablement augmenté en raison de la précipitation des dispersoïdes submicroniques de Mn après tous les traitements thermiques. Deux types de dispersoïdes portant du Mn avec des morphologies cubiques et en forme de tige ont été identifiés à l'aide de l'analyse (TEM). La taille et la densité des dispersoïdes contenant du Mn sont fortement liées à la température et au temps de maintien du traitement thermique. En outre, les traitements thermiques en plusieurs étapes ont montré une microdureté plus élevée et une fraction plus grande de zones dispersoïdes (DZ) que les traitements en une seule étape. Le traitement thermique en deux étapes à basse température (275 °C/12 h + 375 °C/48 h) a introduit la plus forte densité de dispersoïdes parmi tous les traitements thermiques étudiés, mais de graves défauts ont été créés pendant le laminage à chaud. Le traitement thermique en trois étapes modifié (275 °C/12 h + 375 °C/48 h + 500 °C/4 h) a fourni la meilleure combinaison de caractéristiques dispersoïdes et de performance au laminage. Les propriétés de traction des tôles laminées/recuites soumises au traitement thermique en trois étapes ont été remarquablement améliorées par rapport à celles traitées par homogénéisation industrielle, en raison de la densité plus élevée de dispersoïdes de taille plus fine.

Dans la seconde partie, l'influence des additions de Sc et de Zr sur la microstructure et les propriétés mécaniques des tôles laminées à chaud à des températures ambiantes et élevées a été étudiée. Avec l'ajout de Sc et de Zr à l'alliage AA5083, deux populations de particules de renforcement (dispersoïdes AlMn de taille submicronique et précipités $Al_3(Sc,Zr)$ de taille nanométrique ont précipité pendant le traitement thermique en trois étapes. Toutefois, l'ajout

de Sc/Zr a entraîné une réduction de la densité des dispersoïdes AlMn, mais une augmentation de la superficie des zones exemptes de dispersoïdes. De plus, les dispersoïdes d'AlMn et les précipités d'Al_3(Sc,Zr) ont montré un grossissement important pendant le laminage à chaud à 500 °C. En ce qui concerne l'évolution des propriétés mécaniques avec la température d'essai, les propriétés des tôles laminées à température moyenne (25-200 °C) dans les alliages contenant du Sc/Zr ont été significativement améliorées par rapport à l'alliage de base exempt de Sc/Zr, en raison du fort effet d'épinglage des précipités Al_3(Sc,Zr), mais la contribution des dispersoïdes AlMn a été réduite. Cependant, l'(YS) à des températures plus élevées (de 300 à 400 °C) des alliages contenant du Sc/Zr chute à une valeur inférieure à celle de l'alliage de base, ceci est due, fort probablement, des pertes de dislocations et de l'accélération de la recristallisation dynamique (DRX) résultant des ajouts Sc/Zr et du glissement des joints des grains (GBS) pendant la traction à chaud. Les propriétés mécaniques des alliages de base et des alliages contenant du Sc/Zr étaient thermiquement stables pendant une exposition thermique à long terme à 300 °C pendant 500 h, ce qui indique le grand potentiel des alliages Al-Mg-Mn AA5083 pour diverses applications à haute température. L'(YS) à 25 °C et 300 °C a été analysée quantitativement à l'aide d'équations de durcissement constitutives et comparée à des valeurs mesurées expérimentalement. L'(YS) analytique prédite à 25 °C était en bon accord avec les valeurs mesurées expérimentalement. En revanche, il y avait un écart entre l'indice YS prédit et l'indice YS mesuré à 300 °C, en particulier dans les alliages contenant du Sc, principalement en raison du mécanisme d'adoucissement du GBS basé sur les résultats de l'EBSD.

Dans la troisième partie, on a étudié l'évolution des précipitations discontinues et continues d'Al_3(Sc,Zr) au cours d'un processus thermomécanique dans un alliage Al-Mg-Mn AA5083 avec addition supérieure de Sc (~0,4 %). Les résultats ont révélé qu'une densité plus élevée de précipités discontinus Al_3(Sc,Zr) avec une structure en forme de ligne et d'éventail a été formée pendant la solidification avec l'ajout d'un niveau élevé de Sc (0,43% en poids), alors qu'elle est rarement observée avec une faible addition de Sc (0,15% en poids). Au cours d'un traitement thermique en trois étapes (275 °C/12h + 375 °C/48h + 425 °C/12h), deux types de phase de renforcement (dispersoïdes Mn et précipités sphériques continus Al_3(Sc,Zr) se sont formés à l'intérieur de la cellule. En outre, les précipités discontinus d'Al_3(Sc,Zr) ont été en grande partie dissous, et leur taille a diminué dans l'alliage de Sc élevé, tandis que le nombre de précipités sphériques d'Al_3(Sc,Zr) était significativement inférieur à celui de l'alliage de Sc faible, ce qui a réduit la réponse au durcissement par vieillissement. Pendant le laminage à chaud, les précipités discontinus ont été complètement dissous avec un grossissement remarquable en précipités sphériques continus. La densité des Al_3(Sc,Zr) sphériques et fins était beaucoup moins élevée dans l'alliage à Sc élevé que dans l'alliage à faible Sc. En conséquence, les propriétés de traction des alliages contenant du Sc ont été significativement améliorées par rapport à l'alliage de base, en raison de l'effet de renforcement des Al_3(Sc,Zr) sphériques. Néanmoins, le rendement et la résistance à la traction de l'alliage Sc élevé étaient nettement inférieurs à ceux de l'alliage à faible Sc, ce qui indique l'effet délétère des précipités discontinus sur les propriétés mécaniques.

Dans la dernière partie, le rôle des dispersoïdes Mn sur les propriétés de traction et la résistance à la recristallisation de l'alliage Al3Mg0.8Mn laminé à chaud et à froid a été

étudié. Pendant le traitement thermique, le traitement thermique modifié en trois étapes 3S (275 ^{o}C / 12h + 375 ^{o}C / 48 h + 425 ^{o}C / 12h) a révélé une densité plus élevée de dispersoïdes de Mn plus fins que le traitement thermique industriel (Ind : 275 °C / 12 h + 375 °C / 48 h + 500 °C / 4 h). En conséquence, les propriétés mécaniques après 3S sont considérablement améliorées après le laminage à chaud / froid et recuit. Le YS a atteint 196,1 et 233 MPa après le laminage à chaud /recuit (500 ^{o}C/5h) et le laminage à froid/recuit (300 ^{o}C/1h), respectivement, montrant une amélioration de 30% par rapport aux échantillons avec traitement thermique industriel. En outre, l'alliage traité par traitement 3S présente une résistance à la recristallisation plus forte après laminage à chaud et à froid, en raison de la fraction supérieure des dispersoïdes de Mn et de la fraction inférieure de la zone libre de dispersoïdes (DFZ). Les contributions au YS de divers mécanismes de renforcement après laminage à chaud et à froid ont été analysées quantitativement à l'aide des équations constitutives. Les AS prédites étaient en bon accord avec les valeurs mesurées expérimentalement.

Precipitation behaviors of Mn-bearing dispersoids and $Al_3(Sc,Zr)$ precipitates and their impacts on the microstructure and mechanical properties of rolled Al-Mg-Mn 5xxx alloys

Abstract

The vast technological requirements in developing a new generation of lightweight aluminum-alloys are noticeably increased, particularly in applications that serve at elevated temperatures. Therefore, improving the mechanical properties at elevated temperatures turns out as a challenging issue. Al-Mg-Mn 5xxx alloys are one of the potential candidates for high-temperature applications because of the fact that its primary solid solution hardening of Mg in the alloy is not prone to fade at high temperatures. In addition, dispersion strengthening is considered as a promising avenue to improve the mechanical properties of non-heat-treatable alloys, specifically at high temperatures. Hence, in this study, the formation of dispersoids and evolution of mechanical properties at both room and elevated temperatures by modifying the heat treatments and microalloying with Sc and Zr in Al-Mg-Mn 5xxx alloys have been investigated, which can be divided into the following parts:

In the first part, the precipitation behavior of Mn-dispersoids in an Al-5% Mg-0.8% Mn alloy after various single-/multi-step heat treatments and their influence on rolling performance as well as tensile properties was assessed. Results showed that the electrical conductivity (EC) and the microhardness (HV) significantly increased due to the precipitation of submicron Mn-dispersoids after all heat treatments. Two kinds of Mn-bearing dispersoids with cube- and rod-like morphologies were identified with the aid of TEM analysis. The size and the density of Mn-bearing dispersoids are strongly related to the temperature and holding time of heat treatment. Furthermore, the multi-step heat treatments showed higher microhardness and a larger fraction of dispersoid zones (DZ) than single-step treatments. The two-step heat treatment at low temperature (275 °C/12 h + 375 °C /48 h) introduced the highest density of finest dispersoids among all the studied heat treatments, but severe defects were created during hot-rolling. The modified three-step heat treatment (275 °C/12 h + 375 °C/48 h + 500 °C/4 h) provided the best combination of dispersoid characteristics and rolling performance. The tensile properties of rolled/annealed sheets subjected to the three-step heat treatment were remarkably improved compared to those treated using industrial homogenization treatment, owing to the higher density of dispersoids with finer size.

In the second part, the influence of Sc and Zr additions on the microstructure and mechanical properties of hot-rolled sheets at ambient and elevated temperatures was investigated. With the addition of Sc and Zr to AA5083 alloy, two populations of strengthening particles (submicron-sized AlMn dispersoids and nanosized $Al_3(Sc,Zr)$ precipitate) precipitated during three-step heat treatment. However, the Sc/Zr addition caused a reduction in the density of AlMn dispersoids but an increase on the area of the dispersoid-free zones. In addition, both AlMn dispersoids and $Al_3(Sc,Zr)$ precipitates exhibited a significant coarsening during hot rolling at 500 °C. For the evolution of mechanical properties with testing temperature, the rolled sheets' middle-temperature

properties of Sc/Zr containing alloys (25–200 °C) were significantly improved compared with base of Sc/Zr-free alloy, owing to the strong pining effect of Al_3(Sc,Zr) precipitate though the contribution from AlMn dispersoids was reduced. However, the YS of the Sc/Zr-containing alloys at higher temperatures (300–400 °C) dropped to a lower value than the base alloy, most likely due to dislocation losses and the accelerating of dynamic recrystallization (DRX) resulting from Sc/Zr additions and more preferred grain boundary sliding (GBS) during the hot-tensile. The mechanical properties of both the base and Sc/Zr-containing alloys were thermally stable during long-term thermal exposure at 300 °C for 500 h, indicating the great potential of Al-Mg-Mn AA5083 alloys for various elevated-temperature applications. The YS at 25 °C and 300 °C were quantitatively analyzed with the aid of constitutive strengthening equations and compared with experimentally measured values. The analytical predicted YS at 25 ^{o}C was in good agreement with the experimentally measured values. By contrast, there was a discrepancy between the predicted and the measured YS at 300 ^{o}C, particularly in Sc-containing alloys, predominantly due to the GBS softening mechanism based on the EBSD results.

In the third part, the evolution of discontinuous and continuous Al_3(Sc,Zr) precipitation during a thermomechanical process in Al-Mg-Mn AA5083 alloy with higher Sc addition (~0.4%) was investigated. The results revealed that a higher density of rod-like discontinuous Al_3(Sc,Zr) precipitates with line and fan-shape structure was formed during solidification with the addition of high Sc level (0.43 wt.%), while it is rarely observed with low Sc addition (0.15 wt.%). During a three-step heat treatment (275^{o}C/12h + 375^{o}C/48h + 425^{o}C/12h), two kinds of strengthening phase (Mn-dispersoids and spherical continuous Al_3(Sc,Zr) precipitates) were formed in the cell interior. In addition, the discontinuous Al_3(Sc,Zr) precipitates were mostly dissolved, and their size decreased in the high Sc alloy, while the number of spherical Al_3(Sc,Zr) precipitates was significantly lower than in the low Sc alloy, lowering the aging hardening response. During the hot rolling, the discontinuous precipitates were completely dissolved with a remarkable coarsening in spherical continuous precipitates. The density of fine, spherical Al_3(Sc,Zr) was much less in the high Sc alloy than that in the low Sc alloy. As a result, the tensile properties of Sc-containing alloys were significantly improved relative to the base alloy, owing to the strengthening effect of spherical Al_3(Sc,Zr). Nevertheless, the high Sc alloy's yield and ultimate tensile strengths were significantly lower than those of the low Sc alloy, indicating the deleterious effect of discontinuous precipitates on the mechanical properties.

In the last part, the role of Mn-dispersoids on the tensile properties and recrystallization resistance of hot and cold rolled Al3Mg0.8Mn alloy was investigated. During heat treatment, the modified three-step heat treatment 3S (275 ^{o}C / 12h + 375 ^{o}C / 48 h + 425 ^{o}C / 12h) revealed a higher density of finer Mn-dispersoids compared to Industrial-heat treatment (Ind: 275 °C/12 h + 375 °C/48 h + 500 °C/4 h). As a result, the mechanical properties after 3S are significantly improved after hot/cold rolling and annealing. The YS reached 196.1 and 233 MPa after hot rolling/annealing (500 ^{o}C/5h) and cold rolling/annealing (300 ^{o}C/1h), respectively, showing an improvement of 30% over samples with Ind-heat treatment. In addition, the alloy treated with 3S-treatment shows a stronger recrystallization resistance after hot and cold rolling, owing to the higher fraction of Mn-dispersoids and the lower area fraction of dispersoid free zone (DFZ). The YS contributions of various strengthening

mechanisms after hot and cold rolling were quantitatively analyzed using the constitutive equations. The predicted YSs were in good agreement with the experimentally measured values.

Table of Contents

List of Tables

List of Figures

List of Abbreviations

PM	Permanent Mold
Wt%	Weight percent
at%	Atomic percent
OES	Optical Emission Spectrometer
SS	Single-step heat treatment
2S-LT	Two-step heat treatment at low temperature
2S-HT	Two-step heat treatment at high temperature
3S-LT54	Three-step heat treatment
I-homo (Ind)	Industrial heat treatment
OM	Optical Microscope
DSC	Differential scanning calorimetry
SEM	Scanning Electron Microscope
EDS	Energy-Dispersive X-ray Spectrometer
EBSD	Electron backscattered Diffraction
LAGB	Low angle grain boundaries
HAGB	High angle grain boundaries
TEM	Transmission Electron Microscope
CBED	Convergent beam electron diffraction
HV	Hardness Vickers
EC	Electrical Conductivity
IACS	International annealed copper standard

ASTM	American Society for Testing and Materials
IMCs	Intermetallic phases
DZ	Disppersoid Zone
DFZ	Dispersoid Free Zone
PZ	Precipitation Zone
PFZ	Precipitation Free Zone
Eq	Equations
RT	Room Temperature
YS	Yield strength
UTS	Ultimate tensile strength
El	Elongation
SPD	Superplastic deformation
DRX	Dynamic recrystallization
GBS	Grain Boundary Sliding
CP	Continuous precipitates
DCP	Discontinuous Precipitates

List of Symbols

Al	Aluminum
Mg	Magnesium
Mn	Manganese
Fe	Iron
Si	Silicon
Cr	Chormium
Cu	Copper
Ti	Titanium
B	Boron
Ar	Argon
Sc	Scandinum
Zr	Zirconum
β'	Beta prime precipitate
^{o}C	Centigrade degree
h	Hours
kV	Kilovolt
ND (N_d)	Number density
N	Number of precipitated particles
$\overline{D}$	Diameter/Equivalent Diameter
t	TEM foil Thickness
V_f	Volume fraction of precipitated particles

A	Total area
A_A	Area fraction of dispersoids
K	Shape factor
A_{PFZ}	Area fraction of precipitation free zone
µm	Micrometer
nm	Nanometer
MPa	MegaPascal
$\Delta\sigma_{ys}$	Overall Yield strength
σ_o	Strength of Al-matrix
$\Delta\sigma_{SS}$	Solid solution strengthening
$\Delta\sigma_{Mn-dispersoids}$	Strengthening due to Mn-dispersoids
$\Delta\sigma_{\mathrm{Al3(Sc,Zr)}\ precipitates}$	Strengthening due to precipitates
$\Delta\sigma_{gb}$	Grain boundary strengthening
$\Delta\sigma_{MMC}$	Modulus mismatch strength
$\Delta\sigma_{LMC}$	Lattice mismatch strength
b	Burger's vector
M	Taylor factor
χ	Mathematical constant (2.6)
m	Mathematical constant (0.85)
π	Mathematical constant (3.14159)
υ	Poisson's ratio
λ	The effective inter-particle spacing
M'	Mean matrix orientation factor

ΔG	Modulus increments between the matrix and precipitates
G	Shear modulus of the matrix
G_p	Shear modulus of precipitates
r	Mean radius of precipitates
r_c	Critical radius

DEDICATION

I am dedicated this thesis to my beloved parents, Yehia Algendy, Hana Awad, and my respectful brother, Mohammed Algendy, who have meant and continue to mean so much to me. Although my dad is no longer in this world, his memories continue to regulate my life.

At the same time, this thesis is dedicated to my respectful, beloved wife, Yasmin; without her constant support, this work would not have been possible.

Finally, my special dedication is toward my lovely and blessed daughters, Dima and Diala, which enlighten our life path.

ACKNOWLEDGMENT

First and foremost, I would like to thank the Almighty God, by whose mercy I live, have my sustenance, inspiration, and direction for life.

Secondly, I would like to express my deepest sincere thanks to Professor X. Grant Chen for the rare opportunity to be one of his group members. Your supervision, invaluable contributions, support, scientific insights, suggestions, guidance, scientific and technical criticisms, and confidence reposed in me throughout this project; continuously helped shape me into a productive and a good researcher. Furthermore, he has always gone above and beyond to help me get through this challenging journey.

Thirdly, I would also like to extend my deepest gratitude to my academic co-supervisor, Prof. Kun Liu, for his help in the experimental, technical, and scientific discussions, counsel, comments, patience, and support at each step of this long journey that ended up with the improvements in my research skills and qualifications.

Fourthly, I am grateful to Rio Tinto company for their help and for providing the equipment. In addition, I am grateful for the financial support NSERC provided for this work.

I am deeply grateful to my committee members, Prof. Dilip Sarkar, Prof. Emad Elgallad, and Dr. Alexandre Maltais, for their valuable comments, guidance, and support.

Special thanks to Mr. Dany Racine, Mr. Samuel Dessureault, and Mr. Felix Tremblay for their innumerable technical support during my PhD journey.

Then, I would like to express my thankfulness to Prof. Zhan Zhang and Mr. Zhixing Chen for their help in characterization analysis in SEM, TEM.

My gratitude goes to Prof. Emad Elgallad for his valuable help in the experimental and technical-scientific discussions during my PhD life.

I would like to express my heartfelt appreciation to Prof. Khaled Ragab for his support, mentorship, counsel, and encouragement during this long journey. I would also like to thank him for his valuable time from when we left Cairo until we arrived in Chicoutimi and provided us with all the resources we need to live comfortably here.

Meanwhile, I am also intensely indebted to all my colleagues for their collaboration, insightful and fruitful scientific and experimental discussions, and for sharing their experiences with me: Mohamed Qassem, Siamak Nikzad Khangholi, Ali Elashery, Mohammadreza Mofarrehi, Chaima Hajji, Mohamed Ahmed, Henry Agbe, Mohamed Attia, Amara Belkacem, Peng Hu, Liying Cui, Karthikeyan Rajan, Lanfeng Jin, Jovid Rakhmonov, Esmaeil Pourkhorshid, Shuai Wang, Cong Li, Zimeng Wang, Dong Li, and Redouane Farid.

I am extremely grateful to express my appreciation to my dear friends Amin Bouaicha, Laurence Claveau, and Oussama Beroual for their help while living in Chicoutimi.

Best for last, I am indebted to all the sacrifices and love my family made (especially Mom, my beloved wife, my elder brother, sisters, and my beloved daughters), without which I could not even imagine this long journey.

Finally, I would like to express my gratitude to everyone who has helped in numerous ways to complete this thesis successfully. I apologize for not being able to thank you all individually.

Chapter 1: Introduction

The exceptional properties of aluminum and its alloys such as high strength, good formability, weldability, and excellent corrosion resistance make them one of the most multilateral, economical, and desirable materials for various applications (structural and transportation, and aerospace). Among the various applications, the substantial interest in developing a new generation of lightweight aluminum alloys that could be used in a wider range of temperatures, especially for elevated temperatures (250-350 ^{o}C), has significantly increased [1-4].

Generally, the application temperature of traditional age-hardenable Al-alloys (2xxx, 6xxx, 7xxx) is limited to up 150-200 ^{o}C due to the higher coarsening rate of strengthening phases (Al_2Cu, Mg_2Si, and $MgZn_2$) at higher temperatures [5, 6]. Therefore, non-heat treatable aluminum alloys are drawing more interests for elevated-temperature applications. Among them, non-heat treatable Al-Mg-Mn (5xxx) alloys are excellent candidates for a broad range of applications, especially transportation (automotive, shipbuilding, etc.) and structural components [7-10] because of their high strength-to-weight ratio, good forming performance, weldability, toughness, and excellent corrosion resistance.

However, unlike precipitation-strengthening alloys such as 2xxx, 6xxx, and 7xxx, Al-Mg-Mn (5xxx) alloys derive their strength mainly from work hardening [9, 11, 12] and (Mg) solid solution strengthening [11, 13]. Therefore, the strength of this group is limited compared to other heat-treatable high-strength Al-alloys, thus restricting their performance in various applications. In recent decades, dispersion strengthening has been considered as a

promising avenue in improving the mechanical properties at room and elevated temperatures of non-age-hardenable alloys, such as AA3xxx alloys [2, 3, 14, 15].

The industrial production of sheet metal of Al-Mg 5xxx alloys includes casting, homogenization treatment, and deformation [16]. The homogenization is generally applied after casting to reduce the element segregation produced during solidification [17]. During homogenization, some submicron Mn-dispersoids precipitate in the dendritic cells and grains, significantly improving the deformed structure. However, in Al-Mg-Mn AA5xxx alloys, the beneficial effect of the pre-formed Mn-dispersoids before the deformation process is limited to their role in recrystallization resistance [18-20]. Therefore, their influence on improving the alloy properties at ambient and elevated temperatures is less concentrated and limited. Furthermore, the homogenization treatment of Al-Mg alloys is usually conducted at a relatively higher temperature (500–550 °C), resulting in a lower density but coarse Mn-dispersoids, which showed little strengthening effect [17, 18, 20-22].

The precipitation behavior of Mn-dispersoids in Al-Mg-Mn 5xxx alloys was previously studied in different aspects. Different kinds of Mn-bearing dispersoids such as Al_6Mn, α-Al(Mn,Fe)Si, and ν-$Al_{18}(Cr,Mn)_2Mg_3$ were reported in Al-Mg-Mn alloys, the type of Mn-dispersoids enormously depends on the alloy chemistry and treatment temperature [17, 18, 21-26]. For example, ν-$Al_{18}(Cr,Mn)_2Mg_3$ dispersoids are reported to form during homogenization at relatively low temperatures in alloy with higher Cr content [22, 27]. In addition, Engler *et al.* [21] reported that the type of Mn-dispersoids was strongly controlled by the alloy composition Mg and Si content during homogenization treatment at (480-550^{o}C). Furthermore, their size and volume fraction play a significant role in the recrystallization resistance and the flow stress. Osman *et al.* [24] studied the evolution of

second-phase particles in AA5454 alloy after various homogenization cycles, including single and two-step treatment with a minimum treatment temperature of (500-560 ^{o}C), showing the precipitation of coarser and less dense dispersoids. They reported that the characteristics of Mn-dispersoids strongly depend on homogenization practices. Furthermore, Ratchev *et al.* [25] reported that two different morphologies of Al_6(Mn,Fe) dispersoids with high and low aspect ratios occurred in AA5182 alloy at different preheating temperatures during homogenization and their influence on recrystallization and hot ductility.

In the study by Nikulin [28] found that the size and distribution of Al_6Mn phases significantly affect the grain refinement of the Al-Mg–Mn alloy during the ECAB process. Furthermore, Engler *et al.* [18] found that the degree of recrystallization is controlled by the volume and size of dispersoids formed during heat treatment (Zener drag Pz).

From the reviewed literature, in Al-Mg-Mn AA5xxx alloys, the beneficial effect of the pre-formed Mn-dispersoids before the deformation process is limited to their role in recrystallization resistance [18-20] and their influence on improving the alloy properties at ambient and elevated temperatures is less concentrated and limited. Besides, the homogenization treatment of Al-Mg alloys is usually conducted at a relatively higher temperature (500–550 °C), resulting in a lower density but coarse Mn-dispersoids, which showed little strengthening effect [17, 18, 20-22].

In recent years, the mechanical properties of Al-alloys are further improved by introducing transition and rare-eart element (Mn, Zr, Sc, etc.) [29-32]. Microalloying additions of transition and rare earth elements to Al-alloys offer a new challenge for producing a new generation of alloys with excellent performance. For example, as an

effective microalloying element, Sc has often been introduced in aluminum alloys to enhance mechanical properties and recrystallization resistance [33-38]. In addition, cost-effective Zr is usually added with Sc and can substitute Sc and form a core-shell $L1_2$-Al_3(Sc,Zr) precipitates with better-coarsening resistance than Al_3Sc, improving the recrystallization resistance and elevated temperature properties [33, 39-41].

In Al-Sc/Al-Sc-Zr systems, Al_3Sc/Al_3(Sc, Zr) precipitates are formed continuously and discontinuously [42-45]. Continuous precipitation usually occurs during aging treatment (300–425 °C), introducing a fine, spherical $L1_2$-Al_3Sc/Al_3(Sc,Zr) as a main strengthening phase. Nano-sized, fine, coheren, thermally stable $L1_2$-Al_3Sc/Al_3(Sc,Zr) precipitates effectively inhibit the dislocation and grain boundary movements and significantly improve the alloy properties [33, 36, 46, 47]. On the other hand, discontinuous precipitation can also occur during solidification or aging treatment [45, 48-50]. The tendency of Al-Sc alloys to form Al_3Sc discontinuous precipitates is strongly related to their Sc level (often in high-Sc hyper-eutectic alloys) [43, 45, 51, 52], solidification rate (slower cooling rate) [43, 48, 49, 53], and annealing temperature (at intermediate aging temperatures of 300-400 ^oC) [43, 50].

The influence of the discontinuous precipitates on the alloy properties has been studied, and the results were conflicting. For example, Lohar *et al.* [53] reported the negative effect of Al_3(Sc, Zr) discontinuous precipitates and showed that the aged sample has the lowest hardness value. On the other hand, S. Lathabai, P.G. Lloyd [49] stated the positive effect of the discontinuous precipitation strengthening in Al-4.5%Mg-0.7Mn-(0.17-0.26%) Sc cast structure. The results significantly improve the hardness and tensile properties via nano Al_3Sc discontinuous precipitates. On the other hand, W.G. Zhang *et al*. [50] reported the

deterioration effect of discontinuous precipitates on the microhardness of heat-treated Al-0.7 wt.% Sc.

Furthermore, the primary $Al_3(Sc,Zr)$ phase could refine the grain with addition exceeding the eutectic point (0.55 wt.%), improving the mechanical properties [43, 54, 55]. Teng's research [37] demonstrates that with the addition of 0.25 wt.% Sc, the grain size was reduced from 30 μm to 10 μm, proving a significant grain refining with a trace of Sc addition. Likewise, substantial grain refining is accomplished with the binary additions of Sc and Zr [55, 56].

In several other studies, Sc and Zr were added to traditional heat-treatable alloys to improve the mechanical properties, such as in 2xxx, 6xxx, and 7xxx alloys [57-59]. The results showed a significant improvement of microhardness and mechanical properties at room temperature mainly due to the combined strengthening effect of aging strengthening phases (Al_2Cu, Mg_2Si, and $MgZn_2$) and nano $Al_3(Sc,Zr)$ precipitates. For instance, the tensile strength and high cycle fatigue strength of AA6106 alloys increased with Sc and Zr additions [57]; a noticeable increase in the hardness level was obtained in AA2219 alloy due to Sc and Zr additions [58]. However, owing to the high coarsening rate of strengthening phases (Al_2Cu, Mg_2Si, and $MgZn_2$) of heat-treatable alloys at elevated temperatures, most studies with Sc or Sc and Zr mainly focus on the ambient-temperature properties [37, 60]. In addition, the aging temperatures for precipitating conventional strengthening phases (Al_2Cu, Mg_2Si, and $MgZn_2$) were very different from $Al_3(Sc,Zr)$, making the heat treatment of both types phases incompatible. Therefore, the benefits of microalloying with Sc and Zr and precipitation of fine and thermally stable $Al_3(Sc,Zr)$ could not be fully applied.

Until now, the open literature on improving the precipitation behavior of Mn-dispersoids in Al-Mg-Mn 5xxx alloys is very scarce according to the knowledge of the author. In addition, the influence of the Mn-dispersoids on the mechanical properties at room and elevated temperatures are rarely reported. Furthermore, very little information in the literature can be found on the synergetic effects of these two types of strengthening phases (Mn-dispersoids and $Al_3(Sc,Zr)$ precipitates) on the tensile properties Al-Mg-Mn 5xxx alloys at room and elevated-temperatures.

Therefore, the present research focused on improving the precipitation behavior of Mn-dispersoids in Al-Mg-Mn AA5xxx alloys by introducing the novel heat treatment and microalloying with Sc/Zr as well as their influence on the room- and elevated-temperature properties.

1.1 Problem statement

To improve the mechanical properties of Al-Mg-Mn alloys at room and elevated temperatures, it is necessary to optimize the precipitation of the strengthening particles (Mn-dispersoids) before the deformation process and find out the role of alloying elements and additions (transition elements e.g. Sc and Zr).

Until now, there is no open literature on improving the precipitation behavior of Mn-dispersoids in Al-Mg-Mn 5xxx alloys. In addition, the impact of the Mn-dispersoids on the mechanical properties at room and elevated temperatures and recrystallization resistance of rolled Al-Mg sheet are rarely reported. Previous reports on Al-Mg study the precipitation of dispersoids at higher temperatures (500–550 °C), showing a lower density of coarse

dispersoids. Therefore, the effect of these dispersoids on improving the mechanical properties is relatively limited, owing to their large size and low volume fraction.

Furthermore, earlier research studied the role of Sc and Zr addition on high-temperature properties of Al-alloys, mainly focusing on the creep property of the cast alloys [40, 61] or superplastic deformation (SPD) of processed alloys [62, 63]. By contrast, there is limited data about their influence on the hot tensile properties. In addition, the influence of various Sc-level on the microstructure and mechanical properties is still lacking and the results were conflicting in the Al-Mg-Mn alloys. Therefore, it would be worth investigating the synergetic effects of these two types of strengthening phases (Mn-dispersoids and Al_3(Sc,Zr) precipitate) on microstructure and the tensile properties at room and elevated temperatures of this Al-Mg alloy.

1.2 Objectives

The main objective of this project is to improve the mechanical properties Al-Mg-Mn 5xxx alloys under various parameters (heat treatments and microalloying with Sc, Zr elements). The research project is divided in to three topics with the following specific sub-objectives:

1. Optimize the heat treatment parameters and study the evolution of dispersoids in Al-5%Mg-0.8%Mn (AA5083) alloy

I. Study the evolution of dispersoids during a broad range of heat treatments involving single- and- multistep heat treatments.
II. Optimize the rolling parameter to get a sheet metal.
III. Investigate the evolution of the mechanical properties after various heat treatment.

2. Study the effect of Sc and Zr additions on the microstructural evolution and mechanical properties at room and elevated temperature of hot rolled AA5083 alloy

(a) Effects of AlMn dispersoids and Al_3(Sc,Zr) precipitates on the microstructure and ambient/elevated-temperatures mechanical properties of hot-rolled AA5083

In this part, Sc was added with a lower level compared with the second part with Zr by a 1:1 ratio.

I. Investigate the evolution of microstructure during the process under as-cast, heat treated and hot-rolled conditions.

II. Evaluate the evolution of mechanical properties with testing temperatures

III. Apply the constitutive equations and calculate the strengthening mechanisms at ambient/elevated temperatures.

(b) Evolution of discontinuous/continuous Al_3(Sc,Zr) precipitates during thermalmechanical process and its impact on tensile properties in Al-Mg-Mn 5083 alloy

In this part, Sc was added with two different levels (low Sc 0.15 wt.% and high Sc 0.4 wt.%).

I. Investigate the precipitation behavior of discontinuous and continuous Al3(ScZr) during the process.

II. Study the influence of Sc-precipitates on the mechanical properties.

3. Role of Mn-bearing dispersoids on the tensile properties and recrystallization resistance of Al-3Mg-0.8Mn alloy

I. Investigate the evolution of dispersoids after a modified three-step heat-treatment and hot-rolled samples in Al-3Mg alloy.

II. Study the evolution of mechanical properties at room temperature after hot and cold rolling.

III. Discover the influence of dispersoids on recrystallization resistance after hot rolling and the annealing process.

1.3 Originality statement

In this project, we focused on dispersion strengthening as a promising way to improve the mechanical properties of Al-Mg-Mn alloys at room and elevated temperatures. Our strategy focused on optimizing the heat treatment parameters, modifying the rolling route, microalloying with Sc and Zr, and changing the Mg levels.

The first part is about the evolution of dispersoids during multistep heat treatments and their effect on rolling performance in an Al-5% Mg-0.8% Mn alloy. This study suggested that the three-step heat treatment (275 °C/12 h + 375 °C/48 h + 500 °C/4 h) provided the best combination of higher density of fine dispersoid characteristics and rolling performance with higher tensile properties than the industrial approach.

In the second part, the combined effect of two populations (AlMn-dispersoids and Al_3(Sc,Zr) precipitate) on the mechanical properties at ambient and elevated temperatures was investigated. Results showed that Sc and Zr additions have a negative effect on the evolution of AlMn-dispersoids, lowering their densities with increasing their size. In addition, the tensile properties at 25-200 ^{o}C significantly improved with Sc and Zr additions. By contrast, the tensile properties at elevated temperature (250-400 ^{o}C) deteriorated with Sc and Zr additions compared with Sc-free alloy. In addition, the results showed the superior thermal stability of AlMn dispersoids and Al_3(Sc,Zr) precipitates, providing great potential for various applications at high temperatures. Finally, the yield strength (YS) was modeled

using the constitutive equations at ambient and elevated temperatures to reveal promising strengthening mechanisms.

In the third part, Sc level was increased to 0.4 wt.% and compared the results with Sc-free alloy and low-Sc alloy (0.15 wt.%) . By increasing the Sc content, a large volume fraction of primary Al_3(Sc,Zr) and many discontinuous Al_3(Sc, Zr) precipitates (DCP) formed during solidification, lowering the hardening efficiency of fine Al_3(Sc, Zr) precipitates during heat treatment. These DCPs gradually decreased with increasing temperature and disappeared after hot rolling. Sc released from dissolved DCP in higher Sc alloy coarsened the continuous Al_3(Sc,Zr) precipitates (CP) and then lower the resultant mechanical properties.

In the fourth part, we focused on the role of the Mn dispersoids on the mechanical properties and recrystallization resistance in Al-3Mg alloy. This study showed the tensile properties and recrystallization resistance after modified three-step heat treatments significantly improved compared to the industrial treatment, reflecting the efficiency of Mn-dispersoids, which is also confirmed by the prediction from constitutive calculations.

1.4 Thesis outline

The current PhD thesis comprises six chapters:

The first chapter presents a brief introduction to the current project, followed by defining the problem statement and the originality of this study.

In the chapter 2, I focused the evolution of dispersoids during multistep heat treatments and their effect on rolling performance in an Al-5%Mg-0.8%Mn alloy, which was published in *Material Characterization*. This chapter is based on the findings of the first stage of this project,

showing the optimum heat treatment parameters in terms of higher density of fine dispersoids and excellent rolling performance. In addition, the optimized heat treatment shows a remarkable improvement in the tensile properties of AA5xxx compared to industrial ones, showing the promising effect of Mn-dispersoids.

In the chapter 3, I worked the effects of AlMn dispersoids and Al_3(Sc,Zr) precipitates on the microstructure and ambient/elevated-temperature mechanical properties of hot-rolled AA5083 alloys, and the results was submitted to *Material Science and Engineering A* . In this chapter, the effect of Sc and Zr additions on the microstructure of as-cast, heat-treated, and hot-rolled conditions in AlMgMn AA5xxx alloy was studied. Then, the impact of two populations (AlMn dispersoids and Al_3(Sc,Zr) precipitates) on the mechanical properties at ambient and elevated temperatures as well as their thermal stability after long-term thermal exposure was discovered . In addition, their combined contributions toward the YS at 25 and 300 °C were analyzed with the aid of constitutive strengthening equations and compared with experimentally measured values.

In the chapter 4, the evolution of Discontinuous/Continuous Al_3(Sc, Zr) precipitates during the thermal process in Al-Mg-Mn 5083 alloy with higher Sc addition was investigated, and the results was submitted to *Material Characterization* for publication. This chapter addresses the evolution of different Sc-precipitates by increasing the Sc content during the thermal process, from the as cast to the hot-rolled structure. In addition, the impact of these precipitates on the mechanical properties was assessed in AlMgMn alloy. This chapter aims to maximize the benefits of Sc-addition to AlMgMn AA5xxx alloys.

In the chapter 5, the role of Mn-bearing dispersoids on the tensile properties and recrystallization resistance of rolled Al-3Mg-0.8Mn alloys was studied. The results of this

chapter are intended to be published as a journal paper but still under internal review. In this work, we addressed the impact of Mn on the mechanical properties and recrystallization resistance after hot and cold rolling and annealing, and the results were compared with industrial heat treatment. In addition, the mechanical properties were correlated using quantitative equations to understand the strengthening mechanisms.

Finally, the chapter 6 contains conclusions and recommendations for future work. Besides the main chapters, appendix I is also listed at the end of this thesis, providing the general description of the sample preparation before hot rolling. In addition, Appendix II, III, and IV present the supplementary data for chapters 2, 3, and 4, respectively.

1.5 References

[1] C. Li, K. Liu, X. Chen, Improvement of elevated-temperature strength and recrystallization resistance via Mn-containing dispersoid strengthening in Al-Mg-Si 6082 alloys, Journal of Materials Science & Technology 39 (2020) 135-143.
[2] Z. Li, Z. Zhang, X. Chen, Microstructure, elevated-temperature mechanical properties and creep resistance of dispersoid-strengthened Al-Mn-Mg 3xxx alloys with varying Mg and Si contents, Material Sciencr & Engineering A 708 (2017) 383-394.
[3] K. Liu, X.G. Chen, Development of Al-Mn-Mg 3004 alloy for applications at elevated temperature via dispersoid strengthening, Materials and Design 84 (2015) 340-350.
[4] J. Rakhmonov, K. Liu, P. Rometsch, N. Parson, X.G. Chen, Effects of Al(MnFe)Si dispersoids with different sizes and number densities on microstructure and ambient/elevated-temperature mechanical properties of extruded Al–Mg–Si AA6082 alloys with varying Mn content, Journal of Alloys and Compounds 861 (2021) 157937-157937.
[5] J.G. Kaufman, Properties of aluminum alloys: tensile, creep, and fatigue data at high and low temperatures, ASM international1999.
[6] I. Polmear, M. Couper, Design and development of an experimental wrought aluminum alloy for use at elevated temperatures, Metallurgical transactions A 19(4) (1988) 1027-1035.
[7] J.R. Davis, Aluminum and Aluminum Alloys, Light Metals and alloys (2001) 66-66.
[8] J.A.V.D. Hoeven, L. Zhuang, A New 5xxx Series Alloy Developed for Automotive Applications, SAE TECHNICAL PAPER SERIES (724) (2002) 1-8.
[9] H. Fang, H. Liu, Y. Yan, Y. Li, X. Xu, X. Chu, Y. Lu, K. Yu, Microstructural and textural evolution of Al-4.5 Mg-0.7 Mn-0.2 Sc alloys during hot rolling, Materials Letters 292 (2021) 129600.
[10] M.E. McMahon, R.L. Haines, P.J. Steiner, J.M. Schulte, S.E. Fakler, J.T. Burns, Beta phase distribution in Al-Mg alloys of varying composition and temper, Corrosion Science 169 (2020) 108618.

[11] E. Huskins, B. Cao, K. Ramesh, Strengthening mechanisms in an Al–Mg alloy, Materials Science and Engineering: A 527(6) (2010) 1292-1298.
[12] L. Tang, X. Peng, J. Huang, A. Ma, Y. Deng, G. Xu, Microstructure and mechanical properties of severely deformed Al-Mg-Sc-Zr alloy and their evolution during annealing, Materials Science and Engineering: A 754 (2019) 295-308.
[13] Ø. Ryen, B. Holmedal, O. Nijs, E. Nes, E. Sjölander, H.-E. Ekström, Strengthening mechanisms in solid solution aluminum alloys, Metallurgical and Materials Transactions A 37(6) (2006) 1999-2006.
[14] Y.J. Li, A.M.F. Muggerud, A. Olsen, T. Furu, Precipitation of partially coherent α-Al(Mn,Fe)Si dispersoids and their strengthening effect in AA 3003 alloy, Acta Materialia 60(3) (2012) 1004-1014.
[15] K. Liu, H. Ma, X.G. Chen, Improving the Elevated-Temperature Properties by Two-Step Heat Treatments in Al-Mn-Mg 3004 Alloys, Metallurgical and Materials Transactions B: Process Metallurgy and Materials Processing Science 49(4) (2018) 1588-1596.
[16] J. Hirsch, Aluminium Sheet Fabrication and Processing, Fundamentals of Aluminium Metallurgy: Production, Processing and Applications, R. Lumley, Ed, CSIRO, Australia, Woodhead Publishing Ltd., UK, 2010.
[17] O. Engler, Z. Liu, K. Kuhnke, Impact of homogenization on particles in the Al-Mg-Mn alloy AA 5454-Experiment and simulation, Journal of Alloys and Compounds 560 (2013) 111-122.
[18] O. Engler, S. Miller-Jupp, Control of second-phase particles in the Al-Mg-Mn alloy AA 5083, Journal of Alloys and Compounds 689 (2016) 998-1010.
[19] K. Kannan, J.S. Vetrano, C.H. Hamilton, Effects of alloy modification and thermomechanical processing on recrystallization of Al-Mg-Mn alloys, Metallurgical and Materials Transactions A: Physical Metallurgy and Materials Science 27(10) (1996) 2947-2957.
[20] Y.J. Li, W.Z. Zhang, K. Marthinsen, Precipitation crystallography of plate-shaped Al6(Mn, Fe) dispersoids in AA5182 alloy, Acta Materialia 60 (2012) 5963-5974.
[21] O. Engler, K. Kuhnke, J. Hasenclever, Development of intermetallic particles during solidification and homogenization of two AA 5xxx series Al-Mg alloys with different Mg contents, Journal of Alloys and Compounds 728 (2017) 669-681.
[22] T. Radetić, M. Popović, E. Romhanji, Microstructure evolution of a modified AA5083 aluminum alloy during a multistage homogenization treatment, Materials Characterization 65 (2012) 16-27.
[23] Y. Li, W. Zhang, K. Marthinsen, Precipitation crystallography of plate-shaped Al6 (Mn, Fe) dispersoids in AA5182 alloy, Acta materialia 60(17) (2012) 5963-5974.
[24] M. Osman, O. Engler, K. Karhausen, L. Löchte, A. McLaren, Effect of homogenisation conditions on recrystallisation in Al–Mg–Mn alloy AA 5454, Materials science and technology 23(6) (2007) 688-698.
[25] P. Ratchev, B. Verlinden, P. Van Houtte, Effect of preheat temperature on the orientation relationship of (Mn,Fe)Al6 precipitates in an AA 5182 Aluminium-Magnesium alloy, Acta Metallurgica Et Materialia 43(2) (1995) 621-629.
[26] J. Grasserbauer, I. Weißensteiner, G. Falkinger, T.M. Kremmer, P.J. Uggowitzer, S. Pogatscher, Influence of Fe and Mn on the Microstructure Formation in 5xxx Alloys—Part I: Evolution of Primary and Secondary Phases, Materials 14(12) (2021) 3204.

[27] O. Engler, K. Kuhnke, K. Westphal, J. Hasenclever, Impact of chromium on the microchemistry evolution during solidi fi cation and homogenization of the Al-Mg alloy AA 5052, Journal of Alloys and Compounds 744 (2018) 561-573.
[28] I. Nikulin, A. Kipelova, S. Malopheyev, R. Kaibyshev, Effect of second phase particles on grain refinement during equal-channel angular pressing of an Al–Mg–Mn alloy, Acta materialia 60(2) (2012) 487-497.
[29] M. Mofarrehi, M. Javidani, X.-G. Chen, Effect of Mn content on the hot deformation behavior and microstructure evolution of Al–Mg–Mn 5xxx alloys, Materials Science and Engineering: A (2022) 143217.
[30] Z. Zhou, J. Chen, F. Wen, S. Han, S. Zhong, L. Qi, R. Guan, Optimization of heat treatment for an Al–Mg–Sc–Mn–Zr alloy with ultrafine grains manufactured by laser powder bed fusion, Materials Characterization (2022) 111977.
[31] O. Trudonoshyn, O. Prach, P. Randelzhofer, K. Durst, C. Körner, Heat treatment of the new high-strength high-ductility Al–Mg–Si–Mn alloys with Sc, Zr and Cr additions, Materialia 15 (2021) 100981.
[32] Y. Wang, B. Yang, M. Gao, E. Zhao, R. Guan, Microstructure evolution, mechanical property response and strengthening mechanism induced by compositional effects in Al–6Mg alloys, Materials & Design (2022) 110849.
[33] C.B. Fuller, J.L. Murray, D.N. Seidman, Temporal evolution of the nanostructure of Al(Sc ,Zr) alloys:Part I -Chemical compositions of Al3(Sc1-xZrx) precipitates, Acta Materialia 53 (2005) 5401-5413.
[34] W. Lefebvre, F. Danoix, H. Hallem, B. Forbord, A. Bostel, K. Marthinsen, Precipitation kinetic of Al3(Sc, Zr) dispersoids in aluminium, Journal of Alloys and Compounds 470 (2009) 107-110.
[35] E.A. Marquis, D.N. Seidman, Nanoscale structural evolution of Al 3 Sc precipitates in Al(Sc) alloys, Acta Materialia 49(11) (2001) 1909-1919.
[36] D.N. Seidman, E.A. Marquis, D.C. Dunand, Precipitation strengthening at ambient and elevated temperatures of heat-treatable Al (Sc) alloys, Acta Materialia 50(16) (2002) 4021-4035.
[37] G.B. Teng, C.Y. Liu, Z.Y. Ma, W.B. Zhou, L.L. Wei, Y. Chen, J. Li, Y.F. Mo, Effects of minor Sc addition on the microstructure and mechanical properties of 7055 Al alloy during aging, Materials Science and Engineering A 713 (2018) 61-66.
[38] P. Xu, F. Jiang, M. Tong, Z. Tang, J. Jiang, N. Yan, Y. Peng, Precipitation characteristics and morphological transitions of Al3Sc precipitates, Journal of Alloys and Compounds 790 (2019) 509-516.
[39] C. Booth-Morrison, D.C. Dunand, D.N. Seidman, Coarsening resistance at 400 °c of precipitation-strengthened Al-Zr-Sc-Er alloys, Acta Materialia 59(18) (2011) 7029-7042.
[40] C.B. Fuller, D.N. Seidman, D.C. Dunand, Mechanical properties of Al (Sc, Zr) alloys at ambient and elevated temperatures, Acta materialia 51(16) (2003) 4803-4814.
[41] J. Qin, Z. Zhang, X.G. Chen, Mechanical Properties and Strengthening Mechanisms of Al-15 Pct B4C Composites with Sc and Zr at Elevated Temperatures, Metallurgical and Materials Transactions A: Physical Metallurgy and Materials Science 47(9) (2016) 4694-4708.
[42] A.K. Lohar, B. Mondal, D. Rafaja, V. Klemm, S.C. Panigrahi, Microstructural investigations on as-cast and annealed Al-Sc and Al-Sc-Zr alloys, Materials Characterization 60(11) (2009) 1387-1394.

[43] J. Røyset, N. Ryum, Scandium in aluminium alloys, International Materials Reviews 50(1) (2005) 19-44.
[44] J. Røyset, N. Ryum, Kinetics and mechanisms of precipitation in an Al-0.2wt.% Sc alloy, Materials Science and Engineering A 396(1-2) (2005) 409-422.
[45] Y. Sun, Q. Pan, Y. Luo, S. Liu, W. Wang, J. Ye, Y. Shi, Z. Huang, S. Xiang, Y. Liu, The effects of scandium heterogeneous distribution on the precipitation behavior of Al3(Sc, Zr) in aluminum alloys, Materials Characterization 174(February) (2021).
[46] S. Ikeshita, A. Strodahs, Z. Saghi, K. Yamada, P. Burdet, S. Hata, K.-i. Ikeda, P.A. Midgley, K. Kaneko, Hardness and microstructural variation of Al – Mg – Mn – Sc – Zr alloy, Micron 82 (2016) 1-8.
[47] S.M. Anijdan, D. Kang, N. Singh, M. Gallerneault, Precipitation behavior of strip cast Al–Mg–0.4 Sc–0.15 Zr alloy under single and multiple-stage aging processes, Materials Science and Engineering: A 640 (2015) 275-279.
[48] Q. Dong, A. Howells, D.J. Lloyd, M. Gallerneault, V. Fallah, Effect of solidification cooling rate on kinetics of continuous/discontinuous Al3(Sc,Zr) precipitation and the subsequent age-hardening response in cold-rolled AlMgSc(Zr) sheets, Materials Science and Engineering A 772 (2020) 138693-138693.
[49] S. Lathabai, P.G. Lloyd, The effect of scandium on the microstructure, mechanical properties and weldability of a cast Al-Mg alloy, Acta Materialia 50(17) (2002) 4275-4292.
[50] W. Zhang, Y. Wu, H. Lu, G. Lao, K. Wang, Y. Ye, P. Li, Discontinuous Precipitation of Nano-Al3Sc Particles in Al-Sc Alloy and its Effect on Mechanical Property, International Journal of Nanoscience 19(1) (2020).
[51] A. Norman, P. Prangnell, R. McEwen, The solidification behaviour of dilute aluminium–scandium alloys, Acta materialia 46(16) (1998) 5715-5732.
[52] N.B. Hopkins, A. M, Constitution and age hardening of Al-Sc alloys, Journal of Materials Science 20 (1985) 2861-2867.
[53] A.K. Lohar, B.N. Mondal, S.C. Panigrahi, Influence of cooling rate on the microstructure and ageing behavior of as-cast Al–Sc–Zr alloy, Journal of Materials Processing Tech. 210(15) (2010) 2135-2141.
[54] X. Zhang, H. Wang, B. Yan, C. Zou, Z. Wei, The effect of grain refinement and precipitation strengthening induced by Sc or Er alloying on the mechanical properties of cast Al-Li-Cu-Mg alloys at elevated temperatures, Materials Science and Engineering: A 822 (2021) 141641.
[55] S.a. Zhou, Z. Zhang, M. Li, D. Pan, H. Su, X. Du, P. Li, Y. Wu, Effect of Sc on microstructure and mechanical properties of as-cast Al-Mg alloys, Materials and Design 90 (2016) 1077-1084.
[56] D. Pan, S. Zhou, Z. Zhang, M. Li, Y. Wu, Effects of Sc(Zr) on the microstructure and mechanical properties of as-cast Al–Mg alloys, Materials Science and Technology (United Kingdom) 33(6) (2017) 751-757.
[57] P. Cavaliere, M. Cabibbo, Effect of Sc and Zr additions on the microstructure and fatigue properties of AA6106 produced by equal-channel-angular-pressing, Materials Characterization 59(3) (2008) 197-203.
[58] T. Dorin, M. Ramajayam, J. Lamb, T. Langan, Effect of Sc and Zr additions on the microstructure/strength of Al-Cu binary alloys, Materials Science and Engineering A 707(July) (2017) 58-64.

[59] G. Li, N. Zhao, T. Liu, J. Li, C. He, C. Shi, E. Liu, J. Sha, Effect of Sc/Zr ratio on the microstructure and mechanical properties of new type of Al-Zn-Mg-Sc-Zr alloys, Materials Science and Engineering A 617 (2014) 219-227.
[60] C. Xu, W. Xiao, R. Zheng, S. Hanada, H. Yamagata, C. Ma, The synergic effects of Sc and Zr on the microstructure and mechanical properties of Al–Si–Mg alloy, Materials & Design 88 (2015) 485-492.
[61] Z. Li, Z. Zhang, X.G. Chen, Improvement in the mechanical properties and creep resistance of Al-Mn-Mg 3004 alloy with Sc and Zr addition, Materials Science and Engineering A 729(December 2017) (2018) 196-207.
[62] M. Li, Q. Pan, Y. Shi, X. Sun, H. Xiang, High strain rate superplasticity in an Al–Mg–Sc–Zr alloy processed via simple rolling, Materials Science and Engineering A 687(January) (2017) 298-305.
[63] F. Liu, Z. Ma, Achieving exceptionally high superplasticity at high strain rates in a micrograined Al–Mg–Sc alloy produced by friction stir processing, Scripta Materialia 59(8) (2008) 882-885.

Chapter 2: Evolution of dispersoids during multistep heat treatments and their effect on rolling performance in an Al-5% Mg-0.8% Mn alloy (Article 1)

Ahmed Y. Algendy[1], Kun Liu[1], X.-Grant Chen[1]
[1] Department of Applied Science, University of Quebec at Chicoutimi, Saguenay (QC), G7H 2B1, Canada

This article has been published in:
Material Characterization 181 (2021) 111487

Abstract

The precipitation behavior of dispersoids in an Al-5% Mg-0.8% Mn alloy after various single-and multistep heat treatments and their effect on rolling performance were investigated. The results show a significant increase in the electrical conductivity and microhardness caused by the precipitation of submicron dispersoids after all heat treatments. In addition, the multistep heat treatments resulted in higher microhardness and a larger fraction of dispersoid zones than single-step treatments. Two types of Mn-bearing dispersoids with cube- and rod-like morphologies were identified. The low-temperature two-step heat treatment (275 °C/12 h + 375 °C /48 h) produced the highest number density of dispersoids with the finest size among all the studied heat treatments but severe defects were created during hot-rolling. The three-step heat treatment (275 °C/12 h + 375 °C/48 h + 500 °C/4 h) provided the best combination of dispersoid characteristics and rolling performance. The mechanical properties of rolled sheets subjected to the three-step heat treatment were improved compared to those treated using industrial homogenization treatment, owing to the higher number density and finer size of the dispersoids.

Keywords: Al-Mg-Mn alloy, Dispersoids, Multistep heat treatment, Microstructure, Rolling performance, Mechanical properties

2.1 Introduction

Owing to their attractive combination of high strength, good formability, weldability, and excellent corrosion resistance, Al-Mg-Mn alloys are widely used in the automotive industry and in marine applications [1, 2]. Unlike heat-treatable alloys such as 2xxx, 6xxx, and 7xxx, Al-Mg 5xxx alloys derive their strength mainly from work hardening and solid solution strengthening due to Mg, which has substantial solid solubility in aluminum [3, 4]. Currently, considerable efforts are being made to improve the mechanical properties of aluminum alloys, which can help achieve weight reduction in automotive and aerospace applications. In recent years, dispersion strengthening has attracted considerable attention as a promising avenue for improving the mechanical properties of non-heat-treatable aluminum alloys [5-8]. Several studies have demonstrated that precipitation of fine, thermally stable dispersoids using appropriate heat treatments can be an effective way to enhance the room- and elevated-temperature properties of aluminum alloys, such as in 3xxx wrought alloys [7, 9, 10]. The dispersoid strengthening effect is strongly dependent on their type, size, volume fraction, and distribution, which are in turn related to the alloy chemistry and heat treatment conditions [6, 7, 11, 12].

In Al-Mg-Mn 5xxx alloys, it has long been recognized that the precipitation of submicron dispersoids plays an important role in recrystallization resistance during the hot deformation process by retarding both the movement of dislocations and grain boundary migration [5, 13, 14]. Ratchev *et al.* [15] reported that two different morphologies of Al_6(Mn,Fe) dispersoids with high and low aspect ratios occurred in AA5182 alloy at different

preheating temperatures during homogenization. Engler *et al.* [14, 16, 17] found that two major types of dispersoids $Al_6(Mn,Fe)$ and α-Al(Fe,Mn)Si, could precipitate in 5xxx alloys and that the type of dispersoids was strongly controlled by the Mg and Si contents. In other studies [18, 19], it was found that Cr-bearing dispersoids could be formed during homogenization at relatively low temperatures, which were identified as ν-$Al_{18}(Cr,Mn)_2Mg_3$. In general, the contribution of these dispersoids to improving the mechanical properties is rather limited owing to their large size and low volume fraction.

Many efforts have been made in Al-Mg-Mn 5xxx alloys to study the precipitation of dispersoids at relatively high temperatures because 5xxx alloys are generally subjected to conventional high-temperature homogenization (500–550 °C) prior to hot rolling. However, homogenization treatment at high temperature resulted in the precipitation of only a few coarse dispersoids, which showed little strengthening effect [17, 18].Therefore, it is necessary to significantly decrease the size of the dispersoids and increase their volume fraction to improve the mechanical properties of 5xxx alloys. Recent studies on 3xxx and 6xxx alloys indicated that heat treatment at relatively low temperatures (i.e., 350–450 °C) could promote dispersoid precipitation and produce a large volume fraction of finer dispersoids [7, 8, 20]. However, limited information in the literature has been found on how to improve the precipitation of dispersoids through heat treatment in 5xxx alloys.

The present study was undertaken to investigate the evolution of dispersoids in a typical as-cast Al-5% Mg-0.8% Mn alloy alloy after a broad range of heat treatments. Several characterization techniques, including optical microscopy, scanning electron microscopy with energy dispersive X-ray spectrometry, transmission electron microscopy, electrical conductivity, and microhardness measurements were used to characterize the as-cast and

heat-treated microstructures. The rolling performance and tensile properties of the rolled sheets after various heat treatments were also evaluated.

2.2 Experimental procedures

The experimental Al-5% Mg-0.8% Mn alloy was prepared by batching commercially pure Al (99.7 wt.%), pure Mg (99.9 wt.%), Al-25% Fe, Al-50% Si, Al-25%Mn, Al-50%Cu and Al-20% Cr master alloys. The chemical composition of the experimental alloy, which is close to AA5083 and AA5183 alloys, was analyzed using an optical emission spectrometer, and the result is shown in Table 2.1. Approximately 3 kg of the material was melted in a graphite crucible using an electrical resistance furnace. The melt temperature was maintained at 780 °C for 30 min, followed by Ar-degassing for 15 min. The melt was then grain-refined using Al-5% Ti-1% B master alloy and finally poured into a preheated steel mold at 250 °C. The dimensions of the cast ingots were 30 mm × 40 mm× 80 mm.

Table 2.1: Chemical composition of experimental alloy (wt.%)

Mg	Mn	Si	Fe	Cu	Cr	Ti	Al
5.23	0.78	0.26	0.31	0.11	0.18	0.11	Bal.

To study the precipitation behavior of the dispersoids, the as-cast ingots were heat-treated at different temperatures for various time periods, followed by water quenching; the details of the procedures are shown in Table 2.2. The first three single-step treatments were used to examine the precipitation behavior of the dispersoids at different temperatures. Multistep heat treatments (2S-LT, 2S-HT, and 3S-LT54) were designed not only to further optimize the dispersoid characteristics (size, number density, and distribution), but also to adapt to the rolling process. The last treatment (I-Homo) represents a common industrial homogenization

practice for Al-Mg-Mn 5xxx alloys prior to hot rolling [21]. The heat treatments were conducted in a programmable electrical air circulating furnace at a heating rate of 60 °C /h. Subsequently, the ingots were hot-rolled using a lab-scale rolling unit in the temperature range of 460–500 °C. When the temperature of the rolled strip fell below 460 °C, the strip was placed back in the furnace to reheat to 500 °C between the rolling passes. After multiple passes, the block was reduced to a final sheet thickness of 3.2 mm with an area reduction of 88%. All rolled sheets were further annealed at 300 °C for 5 h to relieve the rolling-induced thermal stress prior to tensile testing.

Table 2.2: Heat treatments applied in experimental alloy

Code	Parameters
SS3	375 ^{o}C/6, 12, 24, 48 h
SS4	425 ^{o}C/2, 6, 12, 24 h
SS5	500 ^{o}C/2, 6, 12, 24 h
2S-LT	275 ^{o}C/12 h + 375 ^{o}C/48 h
2S-HT	425 ^{o}C/24 h + 500 ^{o}C /4 h
3S-LT54	275 ^{o}C/12 h + 375 ^{o}C/48 h + 500 ^{o}C/4 h
I-Homo	430 ^{o}C/2 h + 480 ^{o}C/2 h + 525 ^{o}C/2 h

The grain structure was characterized under polarized-light optical microscopy after electro-etching using Barker's reagent (3 vol.% HBF4 solution) at 15 V for 3 min. The average grain size was measured using the linear intercept method according to ASTM E112-12 on electro-etched samples in optical microscopy with polarized light. At least 10 fields containing ~ 500 grains each under 50X were analyzed. To observe the dispersoid zones (DZs) and dispersoid-free zones (DFZs), the heat-treated samples were etched in 0.5% HF for 35 s. Image analysis with Clemex PE 4.0 software was used to measure the DZ and DFZ area fractions as well as the area fraction of various intermetallic particles. More than 50

fields were randomly chosen and analyzed, and the average area fraction of intermetallic particles was calculated with those measurements. A scanning electron microscope (SEM, JSM-6480LV) equipped with an energy-dispersive X-ray spectrometer (EDS) was used to identify the composition of the intermetallics. To reveal the details of the dispersoids, a transmission electron microscope (TEM, JEM-2100) operating at 200 kV was used. TEM foils were prepared in a twin-jet electro-polisher using a solution of 30% HNO_3 in methanol at a temperature of −20 °C. The thickness of the observed area in the TEM was measured using convergent electron beam diffraction. All TEM images were taken along the $[001]_{Al}$ zone axis. The size and number density of the dispersoids were measured using image analysis software (ImageJ) on the TEM images. The number density of the dispersoids was determined using the following equation:

$$ND = \frac{N}{A*(D+t)} \quad (1)$$

where *N* is the number of particles in the TEM image, *A* is the total area, *D* is the equivalent diameter, and *t* is the thickness of the TEM foil, which was measured using convergent electron beam diffraction (CBED) method [22].

The precipitation behavior of dispersoids was also evaluated through electrical conductivity measurements using a Sigmascope SMP 10 device at room temperature. Vickers microhardness was determined both after heat treatment and after rolling using an NG-1000 CCD machine with a 25-g load and a 20-s dwell time. Twenty measurements were performed to determine the average value of each sample. To evaluate the mechanical properties after hot rolling, tensile tests at room temperature were conducted using an Instron 8801 servo-hydraulic unit at a strain rate 0.5 mm/min. The tensile sheet samples were

machined according to ASTM E8/E8M-16A in the rolling direction with a gauge area of 3 × 6 mm.

2.3 Results and discussion

2.3.1 As-cast to heat-treated microstructural evolution

Fig. 2.1 shows the grain structure and evolution of the intermetallic particles from the as-cast condition through heat treatment. The as-cast grain structure of the experimental alloy was characterized as equiaxed grains with an average size of 63.8 ± 7.7 μm (Fig. 2.1a). At a higher magnification (Fig. 2.1b), the microstructure is composed of aluminum dendrite cells surrounded by a number of different intermetallics, which were discussed in detail in our previous work [23]. In brief, the dominant intermetallic phases are Fe/Mn-rich $Al_6(Mn,Fe)$ and $Al_m(Mn,Fe)$, in addition to primary Mg_2Si (Fig. 1b). Meanwhile, a minor fraction of Cr-rich α-$Al_{15}(Fe,Mn,Cr)_3Si_2$, ε-$Al_{18}(Cr,Mn)_2Mg_3$, and $Al_6(Mn,Cr)$ phases as well as $Al_7(Cr,Ti)$ (not shown in Fig. 2.1b) were observed [23]. Low melting-point eutectic phases of τ-Al_6CuMg_4 and β-Al_5Mg_2 were also detected in the interdendritic regions, which were formed during the last stage of solidification.

SEM backscattered images (Fig. 2.1c-g) show typical intermetallic phase distributions after single-and multistep treatments. It can be seen that after heat treatment, especially at higher temperature, such as 525 ^oC in industrial homogenization, the majority of the Fe/Mn-rich intermetallics were changed to α-$Al_{15}(Fe,Mn)_3Si_2$ and $Al_6(Mn,Fe)$ with Chinese script morphologies. During heat treatment, primary Mg_2Si was partially or fully dissolved into matrix. As a result, the Si solute level in aluminum matrix becomes higher, which can

stabilize the transformation of Fe-rich intermetallics to α-$Al_{15}(Fe,Mn)_3Si$ [24-27]. Moreover, low melting-point eutectic phases such as τ-Al_6CuMg_4 and β-Al_5Mg_2 were mostly dissolved in all heat treatments except SS348 and 2S-LT samples, where a small fraction remained (Fig. 2.1c and e) because of the low heat treatment temperature. It should be mentioned that τ-Al_6CuMg_4 and β-Al_5Mg_2 are stable at relatively low temperatures [14]. However, the large diffusion coefficients of Cu and Mg enhance the dissolution rate of these phases at relatively high temperatures [28, 29]. Therefore, they were mostly dissolved after heat treatment. Furthermore, the minor Cr-rich ε-$Al_{18}(Cr,Mn)_2Mg_3$ and $Al_6(Mn,Cr)$ phases were stable after all heat treatments (Fig. 2.1c to 2.1g), which can be attributed to their higher formation temperature and the slow diffusion rate of Cr at high temperatures ($D_{400\,°C} = 1.29\times10^{-21}$ [19, 28, 29]. Table 2.3 displays the quantitative results for the area fractions of the major and minor intermetallic phases in the as-cast and heat-treated conditions, showing a general trend of partial dissolution of all intermetallic phases after various heat treatments. It is evident that the amount of intermetallics decreases with increasing heat treatment temperature. Compared to all heat treatments, I-Homo showed the lowest area fraction of the Fe/Mn-rich phase as well as Mg_2Si (Fig. 2.1g), which is likely due to the higher treatment temperature.

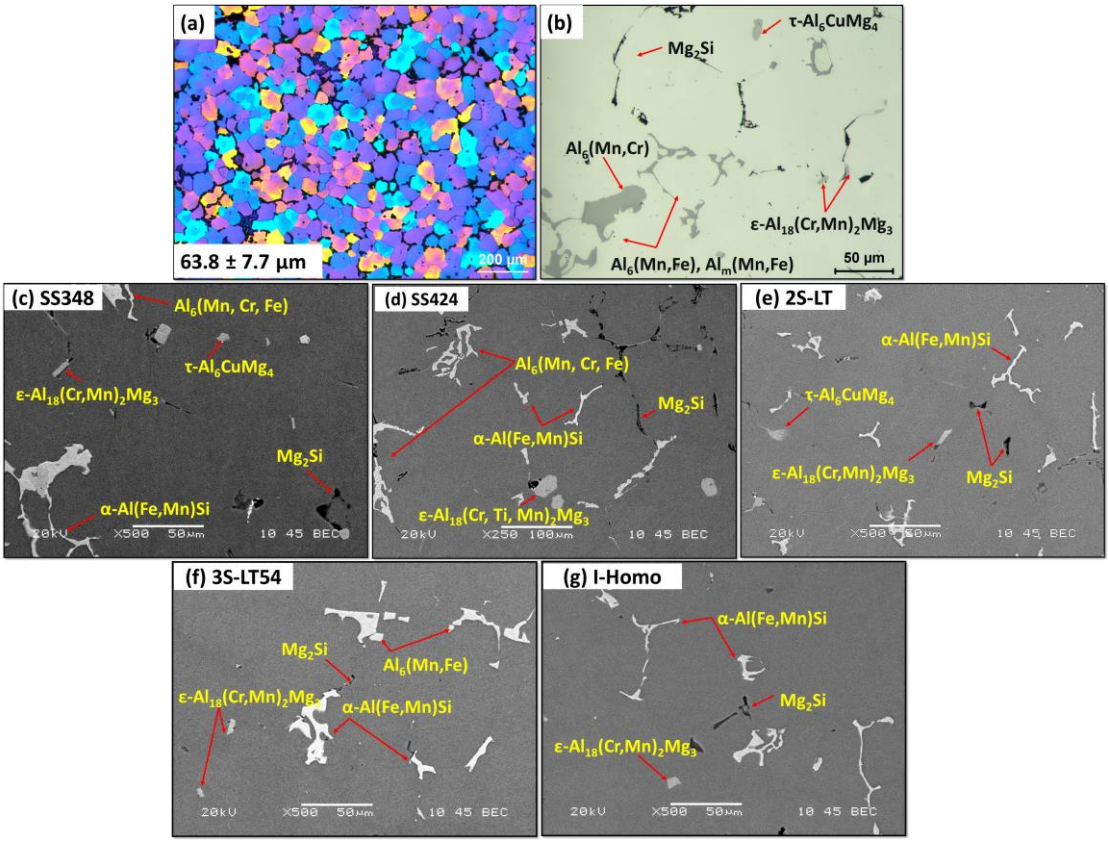

Figure 2.1: Optical images for (a): grain structure and (b): distribution of intermetallic phases in as-cast condition while SEM backscattered images for the distribution of intermetallics after various heat treatments: (c) SS348, 375 °C /48 h, (d) SS424, 425 °C /12 h, (e) 2S-LT, 275 °C /12 h + 375 °C /48 h, (f) 3S-LT52, 275 °C /12 h + 375 °C /48 h + 500 °C /4 h and (g) industrial homogenization (I-Homo), 430 °C /2 h + 480 °C /2 h + 525 °C /2 h.

Table 2.3: Area fraction of intermetallic phases (%) in as-cast and heat-treated conditions

Conditions	Fe/Mn-rich phases	Mg_2Si	Others	Total
As-cast	2.78±1.6	0.82±0.3	0.12±0.1	3.72
SS348	2.45±1.2	0.76±0.4	0.09±0.1	3.3
SS424	2.46±2	0.69±0.5	0.05±0.1	3.2
SS524	2.07±1.6	0.6±0.3	0.04±0.1	2.71
2S-LT	2.18±0.4	0.62±0.1	0.05±0.04	2.85
3S-LT54	1.85±0.7	0.6±0.2	0.05±0.04	2.45
I-Homo	1.46±0.6	0.56±0.2	0.001±0.004	2.021

Note: the last one or two numbers of SS3xx, SS4xx and SS5xx represent the soaking time in h.

2.3.2 Evolution of dispersoids

2.3.2.1 Industrial homogenization treatment

Fig. 2.2 shows the dispersoid distribution after the industrial homogenization treatment (I-Homo sample). As shown in the optical image (Fig. 2.2a), a number of dispersoids formed in the dendrite cells during homogenization, appearing as the dark DZ regions. In addition, large DFZ areas, appearing as light regions, can be observed surrounding the intermetallic phases. DFZ formation is reported to be due to the depletion of Mn content near the Fe/Mn-rich intermetallics [7]. The area fractions of DFZs and DZs were measured to be 35.9% and 60.7%, respectively. It is assumed that the volume fractions are roughly equivalent to the measured area fractions.

As observed by SEM (Fig. 2.2b), the dispersoid number density was small while their average size was large in the DZ. In addition to the normal precipitation of dispersoids, another type of rod-like dispersoid precipitated mostly at the edge of the DZ (Fig. 2.2c). Detailed information about the dispersoids is revealed in the TEM image (Fig. 2.2d). Two different types of dispersoids with cube- and rod-like morphologies co-existed in the DZ (indicated by red crosses). The selected area diffraction patterns (SADP) of cube- and rod-like dispersoids are shown in Fig. 2.2e and 2.2f respectively, while their TEM-EDS results from more than 50 particles are listed in Table 4.2. It can be found that the cube-like dispersoids have a higher Mn content than that of rod-like ones. Combined the results of SADP and their TEM-EDS as well as information from the literature [5, 13, 17, 29, 30], the cube-like dispersoids seem mostly to be Al_4Mn (Hexagonal, $a=b=2.812$ nm, $c=1.274$ nm, $\gamma=120^o$) [31], while the rod-like ones are believed to be Al_6Mn (Orthorhombic, $a=0.6498$ nm $b=0.7574$ nm, $c=0.887$ nm) [5, 32]. However, α-Al(Mn,Fe)Si dispersoids were hardly

detected in the experimental alloy, which is likely contributed to the higher Mg and Mn contents in the present work [5, 14, 17].

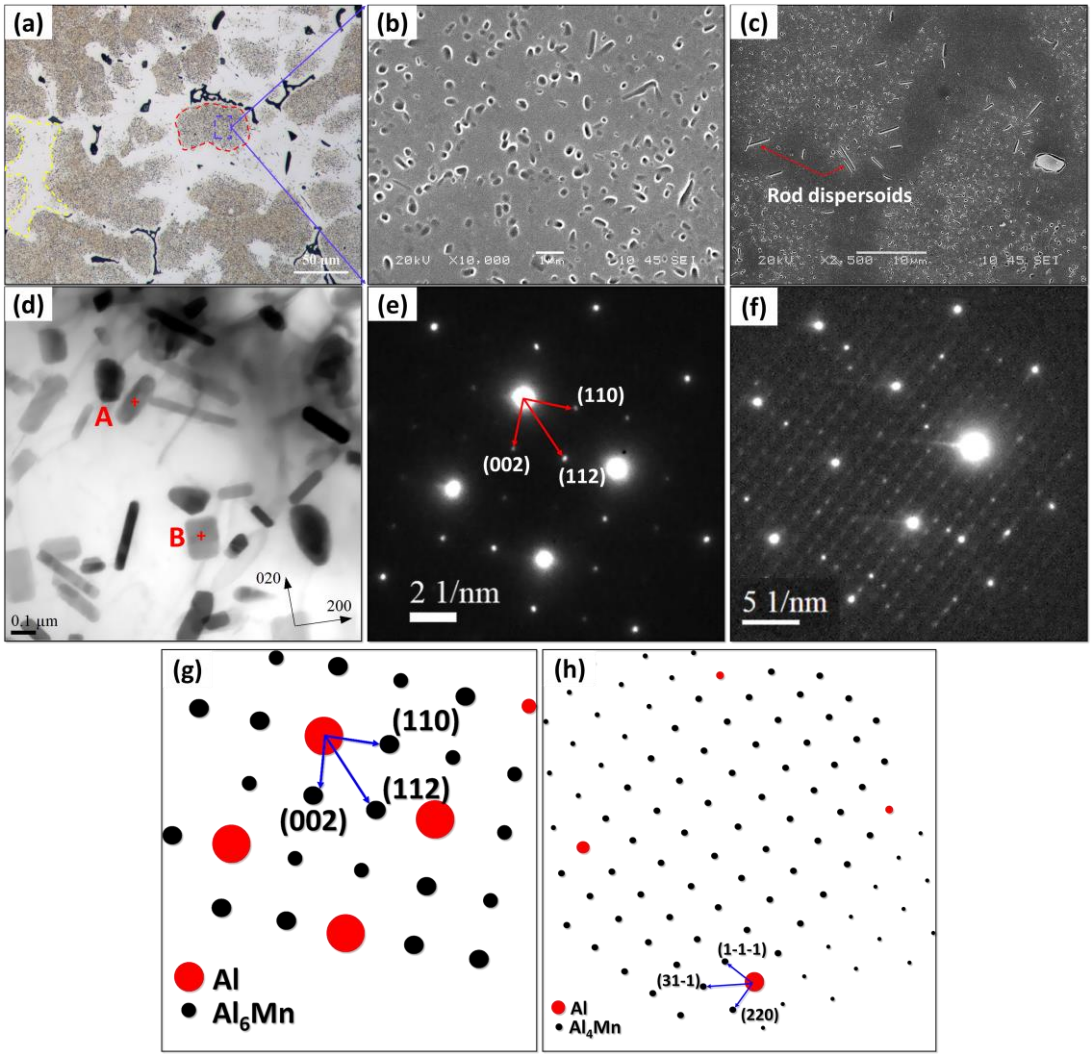

Figure 2.2: Microscopy results after industrial homogenization treatment (I-Homo): (a) OM image of DZ and DFZ distributions, (b) dispersoids in DZs under SEM, (c) rod-like dispersoids under SEM, (d) type and morphology of dispersoids revealed by TEM, and (e) TEM-SADP for rod-like particle "A" as Al_6Mn and (f) TEM-SADP for cube-like particle "B" as Al_4Mn as well as Simulated SADP in (g) for Al_6Mn and (h) for Al_4Mn . All the TEM images and SADP are obtained in <001> zone axis of Al

Fe and Cr can easily replace Mn in the dispersoids because of (1) the similar bcc crystal structures of Fe, Cr, and Mn, and (2) their comparable atomic radii. The presence of Cr may

improve the thermal stability of dispersoids owing to the slow diffusivity of Cr in Al at relatively high temperatures [28, 29]. Quantitative image analysis showed that the number density of the dispersoids was approximately 66.8 μm^{-3} and the equivalent diameter was ~63 nm, as shown in Table 5.2.

Table 2.4: Statistical TEM-EDS results of the chemical compositions of Al_6Mn and Al_4Mn

	At. %				
	Mg	Mn	Cr	Fe	Al
Al_6Mn	5.58±0.5	1.85±0.8	0.36±0.2	0.07±0.2	92.14±0.8
Al_4Mn	3.69±0.9	7.42±1.8	1.04±0.5	0.24±0.3	87.61±1.9

As illustrated in Fig. 2.2, the dispersoids has a relatively low number density in addition to a large DFZ area fraction after industrial homogenization at high temperature. A large volume fraction of finer dispersoids is vital for improving the mechanical properties of 5xxx alloys. Consequently, various single- and multistep heat treatments were applied to study the precipitation behavior of dispersoids.

2.3.2.2 Single-step heat treatment

To determine the formation behavior of dispersoids in the experimental alloy, single-step heat treatments (SS3xx, SS4xx, and SS5xx in Table 2.2) with different soaking times were initially performed. In general, electrical conductivity (EC) and microhardness measurements are two essential methods for evaluating the precipitation behavior of dispersoids [7, 33]. Fig. 2.3 shows the values of EC and microhardness after various single-step heat treatments. As shown in Fig. 2.3a, the lowest EC (19.1% IACS) was obtained in the as-cast condition, indicating that a high level of supersaturation in the aluminum matrix was reached. For the heat-treated samples, EC rapidly increases with increasing treatment

temperature and time, signifying the decomposition of the α-Al supersaturated solid solution and the formation of dispersoids.

When heat-treated at 375 °C (Fig. 2.3a), the EC continued to increase even after 48h, indicating the continuous decomposition of the solid solution and precipitation of dispersoids. With increasing treatment temperature (425 and 500 °C), the EC reached its peak value within a short time (24 h at 425 °C and 12 h at 500 °C), indicating the complete precipitation of dispersoids. In addition, the EC slightly decreased after 12 h at 500 °C, which is mainly attributed to the dissolution of low eutectic melting phases (τ-Al_6CuMg_4/β-Al_5Mg_2) and primary Mg_2Si phase at high treatment temperatures, as shown in Table 2.3.

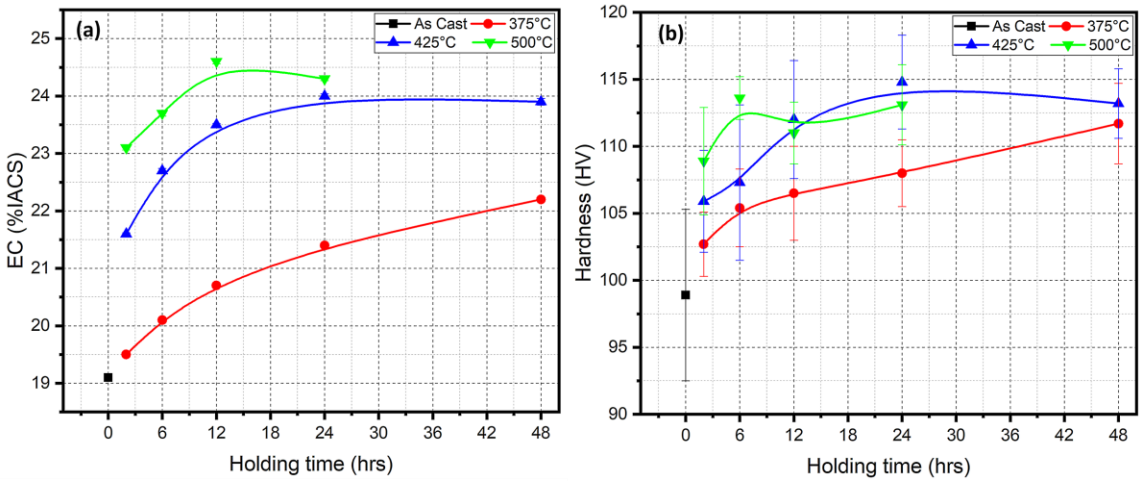

Figure 2.3: (a) Electrical conductivity and (b) microhardness after single step heat treatments

Fig. 2.3b shows the microhardness after single-step heat treatments. As observed, the microhardness after all heat treatments was generally higher than that of the as-cast condition. Furthermore, a similar tendency with EC also exists. When treated at 375 °C, the microhardness shows a continuous increase with increasing holding time, indicating a strengthening effect by the precipitation of dispersoids. At high treatment temperatures (425

and 500 °C), the microhardness values first increased with the holding time and reached a maximum value after 24 h at 425 °C and 6 h at 500 °C, followed by a slight decrease with a further increase in the soaking time. This implies that the maximum strengthening effect of the dispersoid precipitation is reached at a certain soaking time at both temperatures. When further treated at 500 °C for a prolonged time (24 h), a slight increase in the microhardness was observed, which is likely due to the increase in solid solution strengthening by the dissolution of low melting-point eutectic phases, as confirmed by the 500 °C EC values.

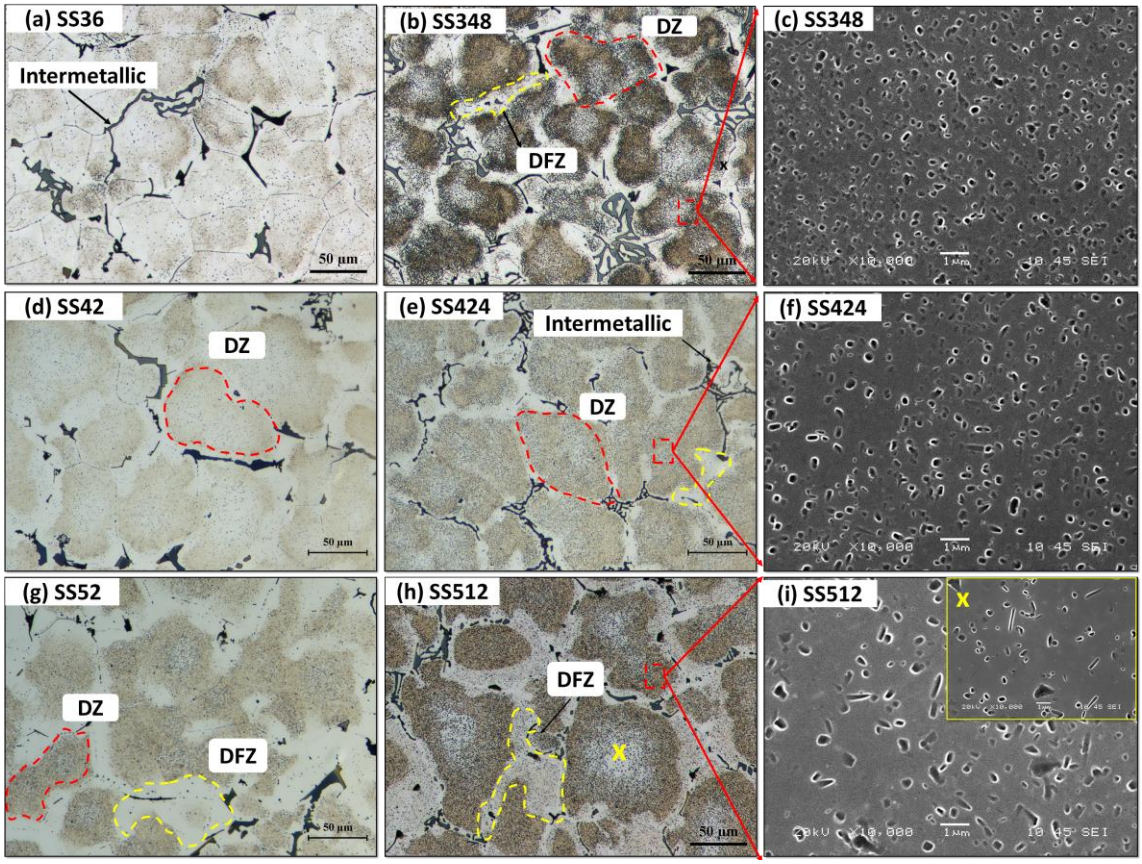

Figure 2.4: Typical microstructures showing the dispersoid distribution after single step heat treatments: (a-c) SS3xx treatment at 375 °C: (a) optical image for 6 h, (b)optical image for 48 h and (c) SEM image for 48 h ; (d-f) SS4xx treatment at 425 °C: (d) optical image for 2 h, (e) optical image for 24 h and (f) SEM image for 24 h; (g-i) SS5xx treatment at 500 °C (g–i): (g) optical image for 2 h, (h) optical image for 12 h and (i) SEM image for 12 h

The Evolution of EC and microhardness in Fig. 2.3 is likely ascribed to the precipitation behavior of the dispersoids during various heat treatments. Fig. 2.4 displays typical microstructures showing the distribution of dispersoids after the three single-step heat treatments. Table 2.5 summarizes the quantitative image analysis of DZs, DFZs, and dispersoids. When treated at 375 °C for 6 h (Fig. 2.4a), the precipitation of dispersoids was not obvious, and the dispersoids appeared sparsely within the matrix. After 48 h at 375 °C, the DZ and DFZ became more visible (Fig. 2.4b), and continuous precipitation of fine dispersoids from the matrix was observed (Fig. 2.4c). As shown in Table 2.5, the volume fraction of DZ significantly increased from 33.3 vol.% after 375 °C/6 h to 64.4 vol.% after 375 °C/48 h with a remarkable decrease in the volume fraction of DFZ. The number density of the dispersoids after 375 °C/6 h is only 87 μm^{-3}, which increased significantly to 325 μm^{-3} after 375 °C/48 h.

Table 2.5: Characteristics of DZ, DFZ and dispersoids during precipitation heat treatments

Conditions	**Volume fraction %**		**Equivalent diameter, nm**	**Number density, μm^{-3}**
	DZ	**DFZ**		
SS36	33.3 ± 1.7	62.5 ± 1.5	14.4 ± 2.3	87 ± 24.3
SS348	64.4 ± 2.7	30.2 ± 1.6	24.4 ± 2	325 ± 47
SS424	68.8 ± 1	26.2 ± 1	35.6 ± 3	188.1± 24
SS56	65.1 ± 1.1	30.8 ± 1.7	47.2 ± 5	137 ± 35.5
SS512	62.4 ± 1.2	35.1 ± 1.3	51.4 ± 9	90.4 ± 27.9
I-Homo	60.7±2.1	35.9±3.4	63±12.5	66.8±12.7

With increasing treatment temperature, the DZ and DFZ were already visible after 2 h at 425 °C (Fig. 4d) and 500 °C (Fig. 2.4g), indicating the efficient precipitation of dispersoids from the decomposition of the supersaturated solid solution. When treated at 425 °C for 24 h (Fig. 4e), the full precipitation of dispersoids was reached (Fig. 4f). The distribution of

dispersoids is more uniform than that of the sample treated at low temperature (375 °C for 48 h), as indicated by the increase in DZ (68.8 vol.% after 425 °C/24 h vs. 64.4 vol.% after 375 °C/48 h) and the corresponding decrease in DFZ. However, the size of the dispersoids increased and the number density decreased relative to that of the sample treated at 375 °C for 48 h (Table 2.5).

When treated at a high temperature with a longer soaking time (500 °C/12 h), some dispersoid-depleted zones appeared in the center of the dendrite cells, as marked with an X in Fig. 2.4h, where the number density of the dispersoids was considerably lower than the surrounding areas of the dendrite cells. This suggests that after the full precipitation (6 h, see Fig. 3), dissolution and coarsening of dispersoids occurred with prolonged soaking time at high treatment temperature. This was confirmed by the decrease in the microhardness after treatment at 500 °C/6 h (Fig. 2.3b). SEM observations (Fig. 2.4i) show that the dispersoids were much larger in size and lower in number density than those treated at 375 °C/48 h and 425 °C/24 h.

Detailed information on the dispersoids in the DZ after various heat treatments was studied using TEM, and the results are shown in Fig. 2.5. In general, two types of dispersoids with cube- and rod-like morphologies were observed under all heat treatment conditions. As illustrated in Fig. 2.5a, only a small number of fine dispersoids was observed after 375 °C/6 h, which explains the slight increase in the EC and microhardness (Fig. 2.3). When the holding time was increased to 48 h (Fig. 2.5b), a large number density of the dispersoids appeared. The number density increased from 87 μm^{-3} at 375 °C/6 h to 325 μm^{-3} at 375 °C/48 h (Table 2.5). With increasing treatment temperature (425 and 500 °C), the dispersoids precipitated out with a larger size and lower number density, as depicted in Fig. 2.5c-d, when

compared with the sample at 375 °C/48 h (Fig. 2.5b). This can be attributed to the fast growth and coarsening of dispersoids owing to the high diffusion rate of Mn and Fe at relatively high temperatures [28, 29]. For instance, the equivalent diameter of dispersoids increases from 24.4 nm after 375 °C/48 h to 35.6 nm after 425 °C/24 h and further to 47.2 nm after 500 °C/6 h. However, the number density of the dispersoids was reduced from 325 μm^{-3} after 375 °C/48 h to 188 μm^{-3} after 425 °C/24 h and further to 137 μm^{-3} after 500 °C/6 h. With heat treatment at a high temperature of 500 °C, the coarsening of the dispersoids was significant (Fig. 2.5e). The number density further decreased to 90.4 μm^{-3} and the size increased to 51.4 nm after 500 °C/12 h.

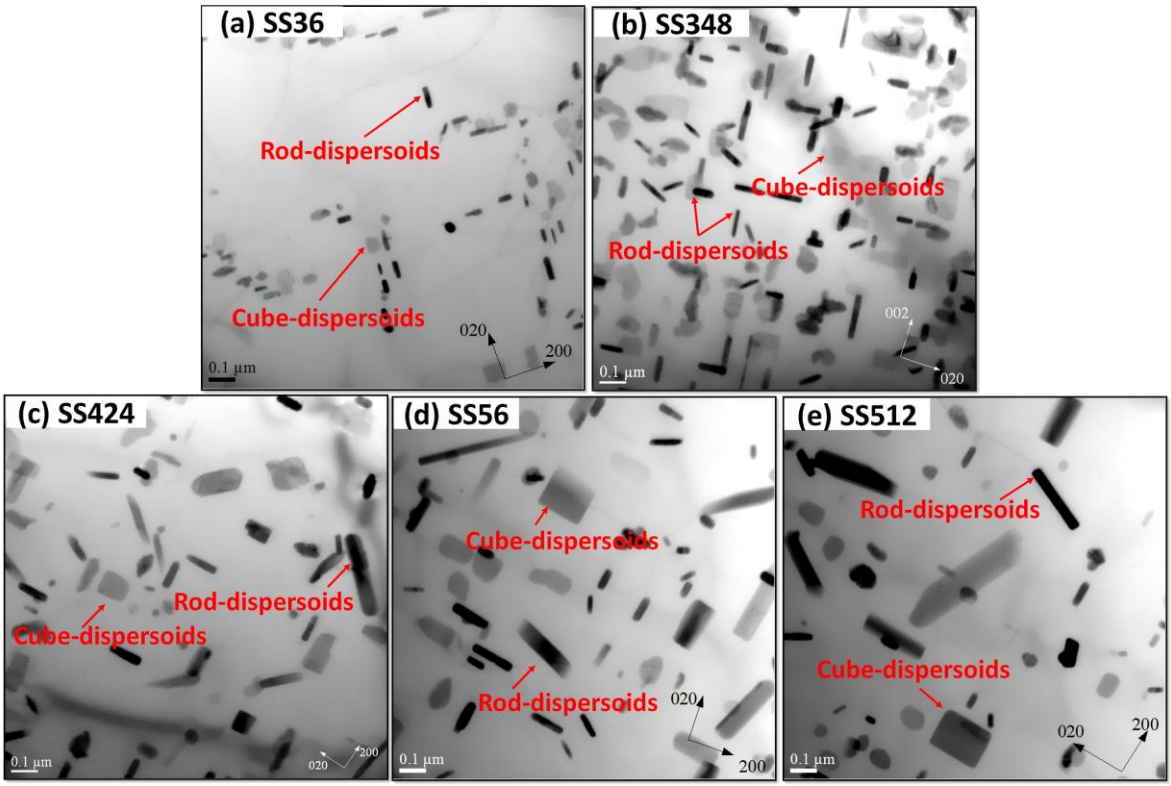

Figure 2.5: Bright-field TEM images showing the size, type and morphology of dispersoids after single-step heat treatments: (a) 375 °C/6 h, (b) 375 °C/48 h, (c) 425 °C/24 h, (d) 500 °C/6 h and (e) 500 °C/12 h.

2.3.2.3 Multistep heat treatments

To improve the mechanical properties of 5xxx alloys, it is necessary to reduce the size of the dispersoids as well as increase their volume fraction. Therefore, the concept of multistep heat treatments is introduced to optimize the formation of dispersoids and to adapt to the rolling process.

Previous studies have reported that the pre-existing metastable β'-MgSi that formed during the first step (250 °C/24 h) could act as nucleation sites for Mn-bearing dispersoids, and therefore, the precipitation of dispersoids after the second step (375 °C/48 h) was greatly promoted in 3xxx alloys [10, 11]. In the present study, a similar two-step treatment approach (2S-LT, 275 °C/12 h + 375 °C/48 h) was first explored with the aim of achieving a high nucleation rate of dispersoids at a relatively low temperature (the first step) followed by the decomposition of the supersaturated solid solution and the precipitation of dispersoids in the second step at 375 °C/48 h.

Fig. 2.6 shows the distribution of the dispersoids during the 2S-LT heat treatment. Fig. 6a shows a bright-field TEM image after the first-step treatment (275 °C/12 h), where a large number of plate-like precipitates appeared with a length range of 280–430 nm and a width of 24–32 nm, which were identified as β'-MgSi [10, 34]. When the samples continued to be treated at 375 °C/48 h, the formation of dispersoids became more obvious with a large fraction of DZ (marked with a red dotted line) in addition to a small fraction of DFZ (marked with a yellow line), as shown in the optical image in Fig. 2.6b. Most β'-MgSi was dissolved during the second step, and fine dispersoids precipitated along $[001]_{Al}$, which is the preferred orientation of metastable β'-MgSi (Fig. 2.6c). The dispersoids were finer with an equivalent diameter of 22.4 nm, and their number density was higher (741.8 μm^{-3}), as shown in Table

2.5, compared with those after the single-step treatment (SS348 in Table 4, 375 °C/48 h). This confirms the promotion effect of the dispersoid precipitation resulting from the pre-formed β' in the first step. As a result, the microhardness after 2S-LT was remarkably higher (121.5 HV) than that of the single-step treatment (112 HV in SS348).

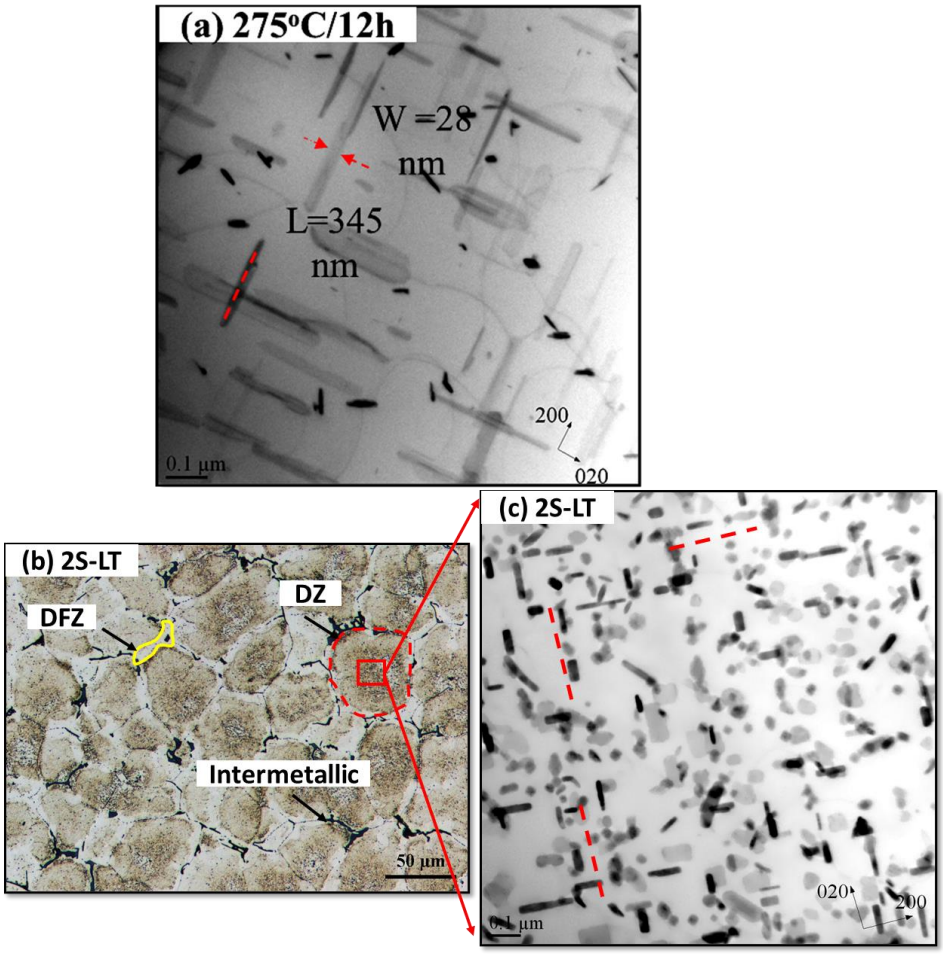

Figure 2.6: Distribution of dispersoids during two-step treatment (2S-LT, 275 °C/12 h + 375 °C/48 h): (a) bright-field TEM image showing the precipitation of β'-Mg2Si after the first step, (b) optical image of the DZ and DFZ distribution, and (c) bright-field TEM image showing the dispersoid precipitation along [001]Al after the second step

Although the 2S-LT treatment resulted in a higher number density of finer dispersoids, there were still some undissolved low-eutectic melting phases, as shown in Fig. 2.1d and Table 2.3, which could cause difficulties during the hot rolling process. Therefore, two other

conditions with the last step at relatively high temperature (500 °C) were also studied, namely 2S-HT (425 °C/24 h + 500 °C/4 h) and 3S-LT54 (275 °C/12 h + 375 °C/48 h + 500 °C/4 h).

Fig. 2.7 shows the distribution of the dispersoids after the 2S-HT and 3S-LT54 heat treatments. An overview of the DZ and DFZ distribution in the 2S-HT and 3S-LT54 samples is shown in Fig. 2.7a and 2.7c. With increasing temperature in the last step at 500 °C, an obvious DFZ increase was observed compared to the same conditions without the last step. Furthermore, the TEM images in Fig. 2.7b and 2.7d reveal that the dispersoids coarsened in the last step, owing to the high diffusivity of Mn and Fe at high temperatures [28, 29]. For instance, the dispersoids were much coarser with a lower number density when treated at 2S-HT (Fig. 2.7b) relative to the SS424 sample (Fig. 2.5c). Similarly, the 3S-LT54 sample exhibited a remarkable increase in dispersoid size with a lower number density (Fig. 2.7d) compared with the 2S-LT sample (Fig. 2.6c).

Table 2.6: Characteristics of DZ, DFZ and dispersoids after multistep heat treatments

Conditions	**Volume fraction %**		**Equivalent diameter, nm**	**Number density, μm^{-3}**
	DZ	**DFZ**		
2S-LT	70.9±2	26.1±2	22.4 ± 8	741.8 ± 65.2
2S-HT	67.1±1.5	30.4±2.4	55.2 ± 7	155.4 ± 11.5
3S-LT54	67.7±1.1	28.9±1.1	31.1 ± 4	333.3 ± 75

Table 2.6 summarizes the quantitative analysis of the dispersoids after the three multistep heat treatments. It can be seen that the DFZ volume fraction increases from 26 vol.% after SS424 to 30.4 vol.% after 2S-HT, while the DFZ volume fraction increases from 26.1 vol.% after 2S-LT to 28.9 vol.% after 3S-LT54. On the other hand, the dispersoid size increases from 22.4 nm after 2S-LT to 31 nm after 3S-LT54, along with a remarkable

reduction in their number density. However, the dispersoids were much finer and their number density was considerably higher after treatment at 3S-LT54 than after 2S-HT.

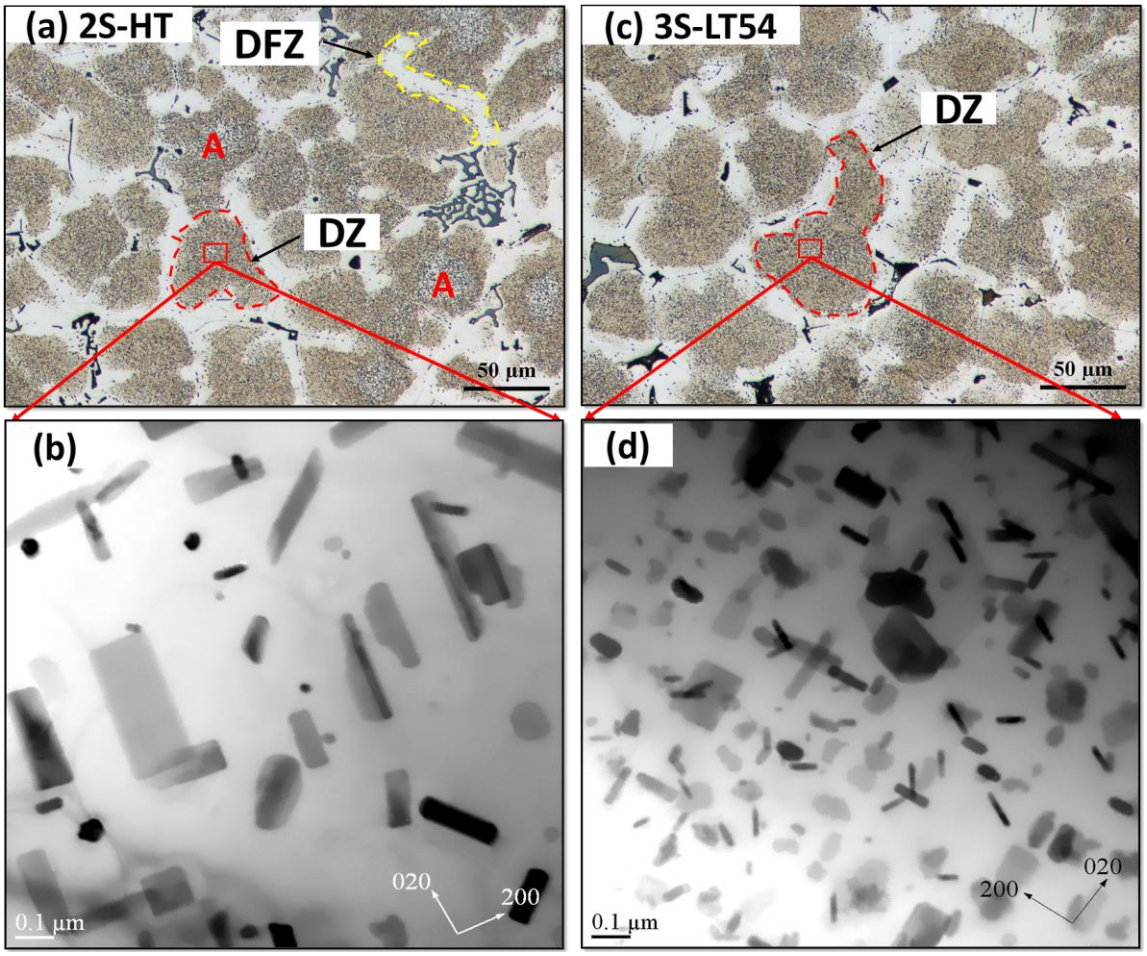

Figure 2.7: Distribution of dispersoids (a and b) after the two-step heat treatment (2S-HT) and (c and d) the three-step heat treatment (3S-LT54); a and c are OM images, and b and d are TEM images.

Fig. 2.8 summarizes the microhardness measurement results. It can be seen that the microhardness significantly increases after all heat treatments compared with the as-cast condition, reflecting the strengthening effect of the dispersoid precipitation. However, the benefit of the two-step treatments is dependent on the condition applied. For instance, the microhardness after the two-step treatment (2S-LT) is remarkably higher than that of the

single-step treatment (SS348), while there is no significant difference in microhardness between the 2S-HT and SS424 samples. As shown in Fig. 2.8, the microhardness shows a slight decrease after 3S-LT54 compared with 2S-LT (118 vs. 121 HV), which can be explained by a decreasing dispersoid number at the last step (Fig. 2.7d vs. Fig. 2.6c). However, the microhardness of the 3S-LT54 sample is still higher than those treated with 2S-HT and I-Homo conditions, indicating the strong strengthening effect of fine and densely distributed dispersoids (Tables 2.5 and 2.6).

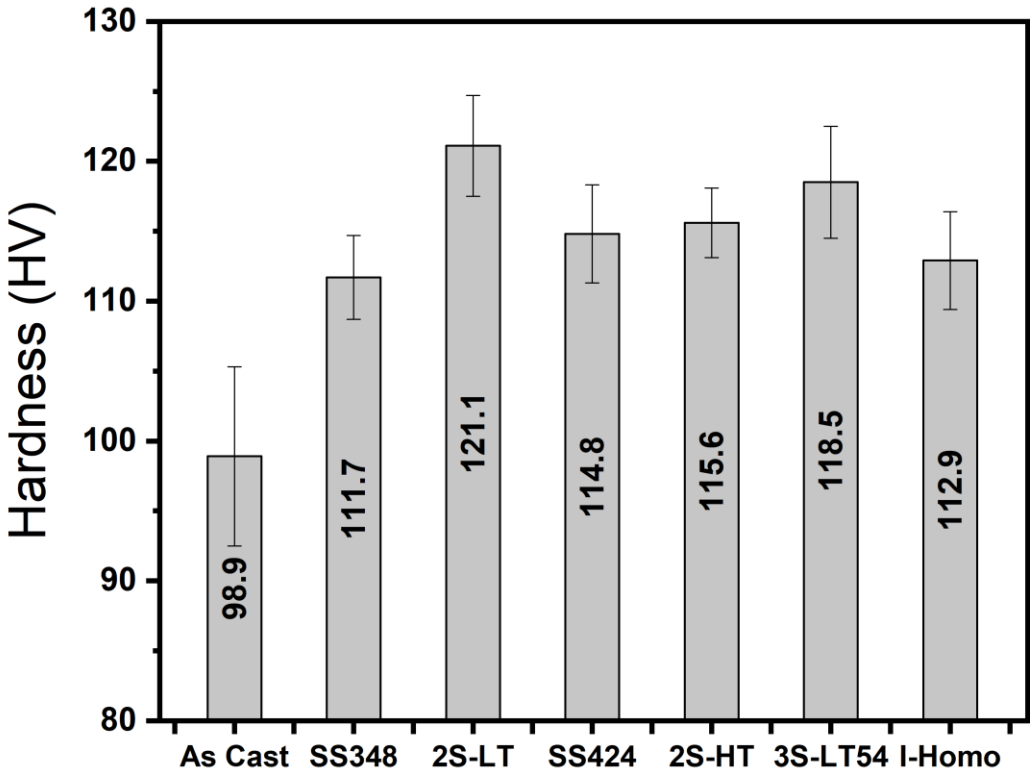

Figure 2.8: Microhardness measurements after single and multistep heat treatments

2.3.3 Rolling Performance

Al-Mg-Mn 5xxx alloys are usually used in sheet form fabricated by the hot rolling process. Hot rolling trials of heat-treated cast ingots were performed; these samples included

those that had undergone SS348, SS424, and multistep treatments. Fig. 2.9 shows representative views of the rolled samples. As shown in Fig. 2.9a, the hot-rolled samples of SS348, SS424, and 2S-LT exhibited severe problems with alligator and surface cracks after only 4–6 passes with an area reduction of 24%–36%. This can most likely be attributed to the remaining low-melting eutectic intermetallic phases resulting from the relatively low heat treatment temperatures (375–425 °C) [35, 36]. However, as shown in Fig. 2.9b, the samples exposed to 2S-HT, 3S-LT54, and I-Homo treatments exhibited good rolling performance with acceptable surface conditions down to the final sheet thickness of 3.2 mm (88% reduction).

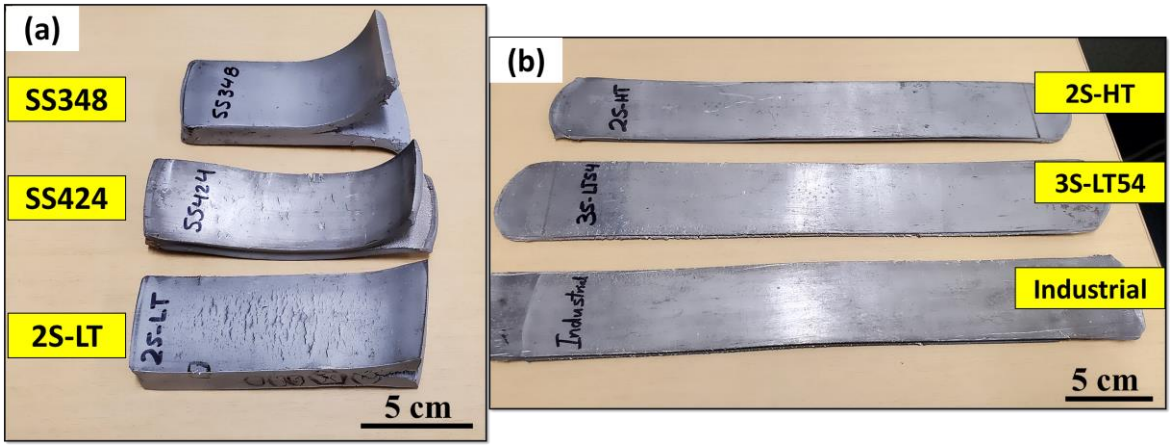

Figure 2.9: Representative views of rolled samples with various heat treatments: (a) samples with alligator and surface crack problems and (b) samples with good rolling performance

All three heat treatments involved a final step at a high temperature of 500 °C, which effectively dissolved the low-melting eutectic intermetallic phases and hence reduced the sensitivity to alligator problems and surface cracks. In addition, coarse rod-like dispersoids were observed in the peripheral areas of the DFZs after high-temperature heat treatments, such as 2S-HT, 3S-LT54, and I-Homo treatments, as shown in Fig. 2.2c and Fig. 2.10. A

previous study has reported that the precipitation of rod-like dispersoids in DFZs could provide a uniform slip distribution during hot deformation, and hence reduce the local stresses at the grain boundaries, resulting in a high resistance to intergranular fracture and alligator problems [35].

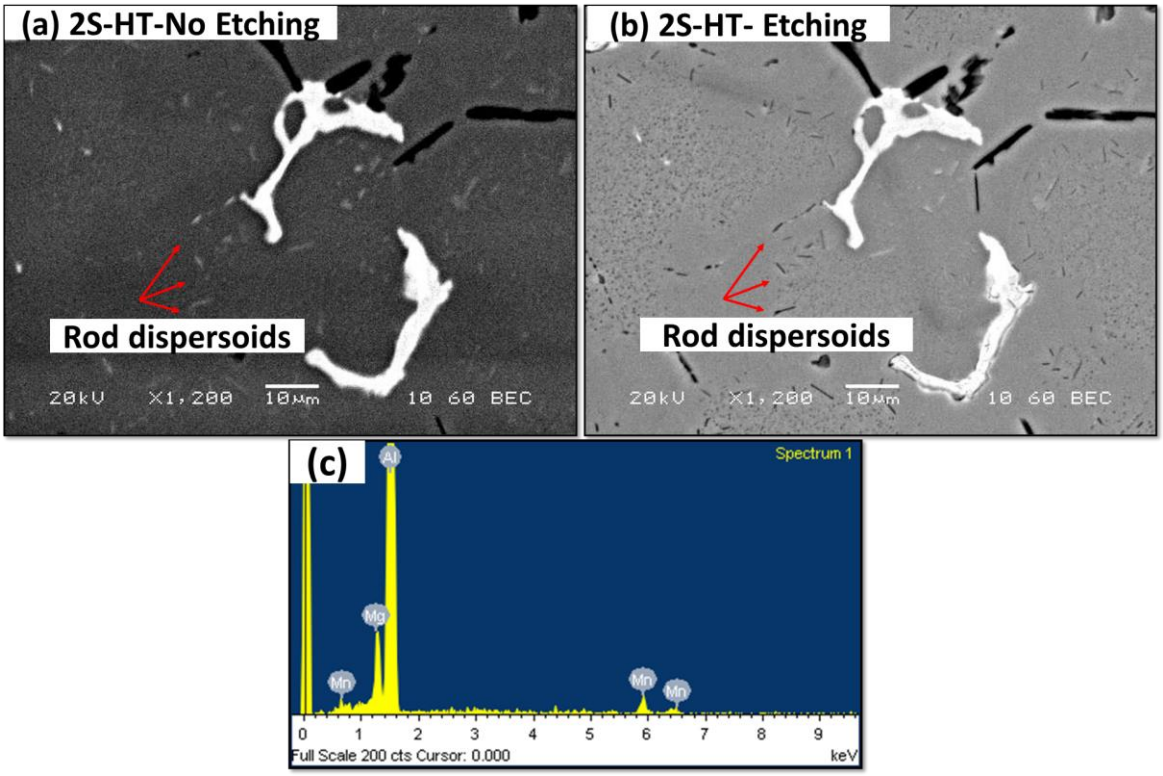

Figure 2.10: Precipitation of rod-like dispersoids in DFZs after high-temperature treatment of the 2S-HT sample: SEM images (a) before and (b) after etching, and (c) SEM-EDS result

2.3.4 Tensile properties after hot rolling

Prior to tensile testing, the hot-rolled samples were annealed at 300 °C/5 h to release the thermal stresses induced by rolling. Fig. 2.11 shows the room-temperature tensile properties of the rolled samples with good rolling performance. As observed, both the 2S-HT and 3S-LT54 samples have higher tensile strengths (YS and UTS) than the I-Homo samples. The

YS and UTS of the 3S-LT54 rolled samples reached 178 and 331 MPa, respectively, showing an improvement of 7.9% in YS and 6.3% in UTS relative to the I-Homo samples at the same elongation level.

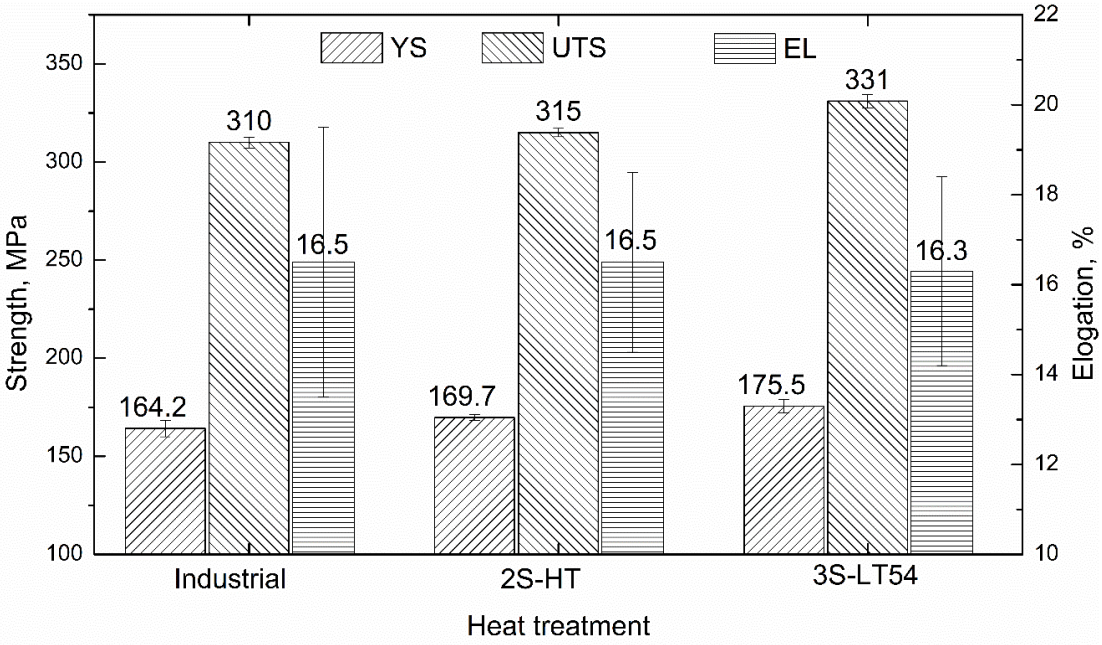

Figure 2.11: Tensile properties of three rolled sheet samples

Fig. 2.12 shows the microstructure after annealing of the hot-rolled samples subjected to 3S-LT54 and I-Homo treatments. Both samples exhibit elongated grains parallel to the rolling direction. However, the I-Homo sample (Fig. 2.12b) shows a higher DFZ area fraction than the sample after 3S-LT54 (Fig. 2.12a). At the higher magnification of the SEM images (Figs. 2.12c and d), it can be seen that the dispersoids in the 3S-LT54 sample have a higher number density with a finer size (Fig. 2.12c) compared to the I-Homo sample. The fact that the rolled 3S-LT54 samples possess higher tensile strengths relative to the I-Homo samples indicates a reasonable strengthening contribution from the fine dispersoids, providing an alternative way to improve the mechanical properties of non-heat-treatable 5xxx wrought alloys. The challenge of maximizing this additional dispersoid strengthening can be

addressed through appropriate alloy chemistry, heat treatment, and rolling processes targeted toward maintaining fine and densely distributed dispersoids in the microstructure.

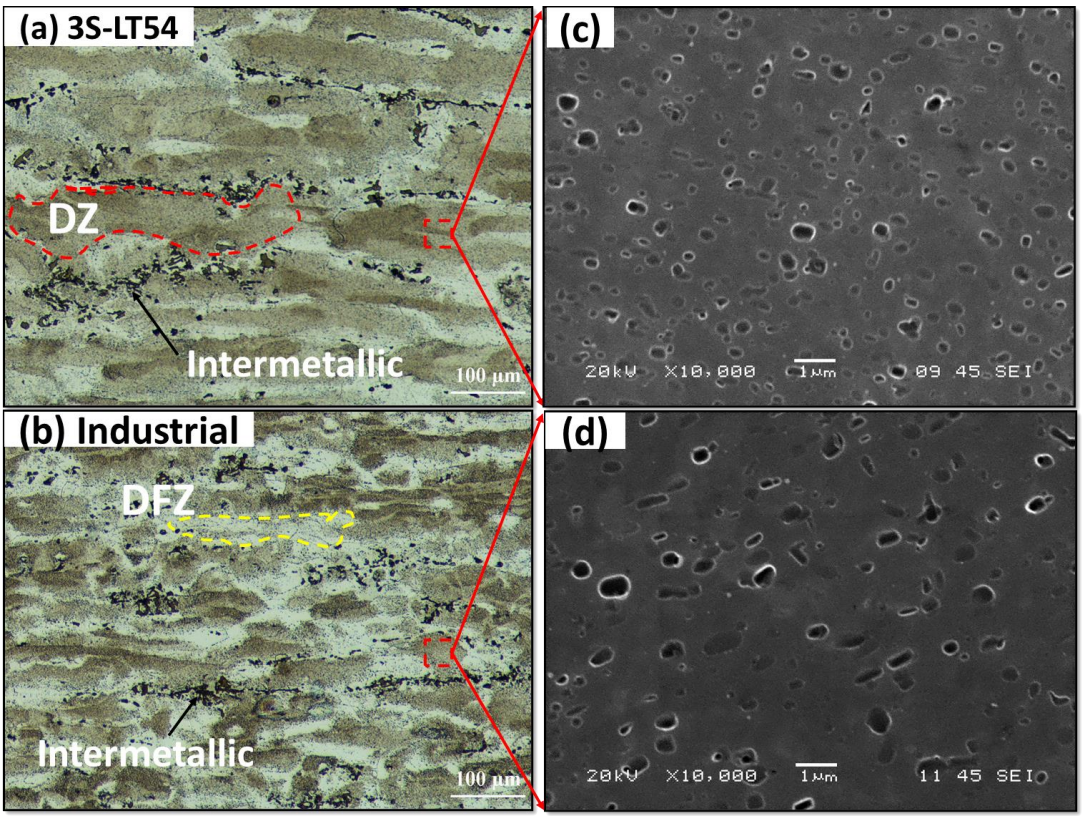

Figure 2.12: Microstructures after hot-rolling of the samples: a and c for 3S-LT54 while (b and d for I-Homo treatments;(a and b are OM images, and c and d are SEM images)

2.4 Conclusions

In the present study, various single- and multistep heat treatments were performed to optimize the characteristics of the dispersoids in terms of the size, number density, and distribution in an Al-5% Mg-0.8% Mn alloy. The rolling performance after different heat treatments was also evaluated. The following conclusions can be drawn:

1. The as-cast microstructure of Al-5% Mg-0.8% Mn alloy consisted of aluminum dendrite cells surrounded by dominant Fe/Mn-rich $Al_6(Mn,Fe)$ and $Al_m(Mn,Fe)$ intermetallic phases, in addition to primary Mg_2Si. Minor fractions of Cr-rich α-$Al_{15}(Fe,Mn,Cr)_3Si_2$, ε-$Al_{18}(Cr,Mn)_2Mg_3$, and $Al_6(Mn,Cr)$, as well as a low melting-point eutectic τ-Al_6CuMg_4 phase were also detected in the interdendritic regions.

2. During all heat treatments, a number of cube- and rod-like dispersoids were observed to precipitate in the dendritic cells and grains. Two types of Mn-bearing dispersoids, Al_4Mn and Al_6Mn, were identified based on their morphology and chemical composition. The size, number density, and distribution of the dispersoids were strongly dependent on the heat treatment step, temperature, and time.

3. The low-temperature two-step heat treatment (2S-LT, 275 °C/12 h + 375 °C/48 h) generated the highest number density of dispersoids with the finest size among all heat treatments studied, but severe defects were created during the hot rolling process.

4. The three-step heat treatment (3S-LT54, 275 °C/12 h + 375 °C/48 h + 500 °C/4 h) provided the best combination of dispersoid characteristics and rolling performance.

5. The mechanical properties of rolled sheets subjected to the three-step heat treatment (3S-LT54) were improved over those obtained through the industrial homogenization treatment, owing to the higher number density and finer size of dispersoids, providing an alternative way to improve the mechanical properties of non-heat-treatable 5xxx wrought alloys.

Acknowledgments

The authors would like to acknowledge the financial support of the Natural Sciences and Engineering Research Council of Canada (NSERC) under the Grant No. CRDPJ 514651-17 and Rio Tinto Aluminum through the Research Chair in the Metallurgy of Aluminum Transformation at University of Quebec at Chicoutimi.

2.5 References

[1] J.R. Davis, Aluminum and Aluminum Alloys, Light Metals and alloys (2001) 66-66.
[2] J.A.V.D. Hoeven, L. Zhuang, A New 5xxx Series Alloy Developed for Automotive Applications, SAE TECHNICAL PAPER SERIES (724) (2002) 1-8.
[3] E.L. Huskins, B. Cao, K.T. Ramesh, Strengthening mechanisms in an Al-Mg alloy, Materials Science and Engineering A 527(6) (2010) 1292-1298.
[4] Ø. Ryen, B. Holmedal, O. Nijs, E. Nes, E. Sjölander, H.-E. Ekström, Strengthening mechanisms in solid solution aluminum alloys, Metallurgical and Materials Transactions A 37(6) (2006) 1999-2006.
[5] Y.J. Li, W.Z. Zhang, K. Marthinsen, Precipitation crystallography of plate-shaped Al6(Mn, Fe) dispersoids in AA5182 alloy, Acta Materialia 60 (2012) 5963-5974.
[6] A. Marie, F. Muggerud, E. Anne, Y. Li, R. Holmestad, Dispersoid strengthening in AA3xxx alloys with varying Mn and Si content during annealing at low temperatures, Materials Science & Engineering A 567 (2013) 21-28.
[7] K. Liu, X.G. Chen, Development of Al-Mn-Mg 3004 alloy for applications at elevated temperature via dispersoid strengthening, Materials and Design 84 (2015) 340-350.
[8] Z. Li, Z. Zhang, X. Chen, Microstructure, elevated-temperature mechanical properties and creep resistance of dispersoid-strengthened Al-Mn-Mg 3xxx alloys with varying Mg and Si contents, Material Sciencr & Engineering A 708 (2017) 383-394.
[9] Y.J. Li, A.M.F. Muggerud, A. Olsen, T. Furu, Precipitation of partially coherent α-Al(Mn,Fe)Si dispersoids and their strengthening effect in AA 3003 alloy, Acta Materialia 60(3) (2012) 1004-1014.
[10] K. Liu, H. Ma, X.G. Chen, Improving the Elevated-Temperature Properties by Two-Step Heat Treatments in Al-Mn-Mg 3004 Alloys, Metallurgical and Materials Transactions B: Process Metallurgy and Materials Processing Science 49(4) (2018) 1588-1596.
[11] Z. Li, Z. Zhang, X.G. Chen, Effect of Metastable Mg2Si and Dislocations on α-Al(MnFe)Si Dispersoid Formation in Al-Mn-Mg 3xxx Alloys, Metallurgical and Materials Transactions A: Physical Metallurgy and Materials Science 49(11) (2018) 5799-5814.
[12] J. Rakhmonov, K. Liu, P. Rometsch, N. Parson, X.G. Chen, Effects of Al(MnFe)Si dispersoids with different sizes and number densities on microstructure and ambient/elevated-temperature mechanical properties of extruded Al–Mg–Si AA6082 alloys with varying Mn content, Journal of Alloys and Compounds 861 (2021) 157937-157937.

[13] K. Kannan, J.S. Vetrano, C.H. Hamilton, Effects of alloy modification and thermomechanical processing on recrystallization of Al-Mg-Mn alloys, Metallurgical and Materials Transactions A: Physical Metallurgy and Materials Science 27(10) (1996) 2947-2957.
[14] O. Engler, S. Miller-Jupp, Control of second-phase particles in the Al-Mg-Mn alloy AA 5083, Journal of Alloys and Compounds 689 (2016) 998-1010.
[15] P. Ratchev, B. Verlinden, P. Van Houtte, Effect of preheat temperature on the orientation relationship of (Mn,Fe)Al6 precipitates in an AA 5182 Aluminium-Magnesium alloy, Acta Metallurgica Et Materialia 43(2) (1995) 621-629.
[16] O. Engler, Z. Liu, K. Kuhnke, Impact of homogenization on particles in the Al-Mg-Mn alloy AA 5454-Experiment and simulation, Journal of Alloys and Compounds 560 (2013) 111-122.
[17] O. Engler, K. Kuhnke, J. Hasenclever, Development of intermetallic particles during solidification and homogenization of two AA 5xxx series Al-Mg alloys with different Mg contents, Journal of Alloys and Compounds 728 (2017) 669-681.
[18] T. Radetić, M. Popović, E. Romhanji, Microstructure evolution of a modified AA5083 aluminum alloy during a multistage homogenization treatment, Materials Characterization 65 (2012) 16-27.
[19] O. Engler, K. Kuhnke, K. Westphal, J. Hasenclever, Impact of chromium on the microchemistry evolution during solidi fi cation and homogenization of the Al-Mg alloy AA 5052, Journal of Alloys and Compounds 744 (2018) 561-573.
[20] C. Li, K. Liu, X. Chen, Improvement of elevated-temperature strength and recrystallization resistance via Mn-containing dispersoid strengthening in Al-Mg-Si 6082 alloys, Journal of Materials Science & Technology 39 (2020) 135-143.
[21] K.M. Gatenby, J. Creek, D. Kang, S.K. Das, (12) Patent Application Publication (10) Pub . No .: US 2016 / 0355915 A1, 1(19) (2016).
[22] S.M. Allen, Foil thickness measurements from convergent-beam diffraction patterns, Philos. Mag A 43(2) (1981) 325-335.
[23] A.Y. Algendy, K. Liu, X.G. Chen, Formation of intermetallic phases during solidification in Al-Mg-Mn 5xxx alloys with various Mg levels, MATEC Web of Conferences 326 (2020) 02002-02002.
[24] D.T.L. Alexander, A.L. Greer, Solid-state intermetallic phase tranformations in 3XXX aluminium alloys, Acta Materialia 50(10) (2002) 2571-2583.
[25] D.T.L. Alexander, A.L. Greer, Nucleation of the Al6(Fe, Mn)-to-α-Al-(Fe, Mn)-Si transformation in 3XXX aluminium alloys. I. Roll-bonded diffusion couples, Philosophical Magazine 84(28) (2004) 3051-3070.
[26] Y.J. Li, L. Arnberg, A eutectoid phase transformation for the primary intermetallic particle from Alm(Fe,Mn) to Al3(Fe,Mn) in AA5182 alloy, Acta Materialia 52(10) (2004) 2945-2952.
[27] Y. Liu, L. Luo, C. Han, L. Ou, J. Wang, C. Liu, Effect of Fe , Si and Cooling Rate on the Formation of Fe- and Mn-rich Intermetallics in Al – 5Mg – 0 . 8Mn Alloy, Journal of Materials Science & Technology 32(4) (2016) 305-312.
[28] Y. Du, Y.A. Chang, B. Huang, W. Gong, Z. Jin, H. Xu, Z. Yuan, Y. Liu, Y. He, F.Y. Xie, Diffusion coefficients of some solutes in fcc and liquid Al: Critical evaluation and correlation, Materials Science and Engineering A 363(1-2) (2003) 140-151.

[29] K.E. Knipling, D.C. Dunand, D.N. Seidman, Criteria for developing castable, creep-resistant aluminum-based alloys - A review, International Journal of Materials Research 97(3) (2006) 246-265.
[30] R. Goswami, G. Spanos, P.S. Pao, R.L. Holtz, Precipitation behavior of the β phase in Al-5083, Materials Science and Engineering A 527(4-5) (2010) 1089-1095.
[31] S.L. Lee, S.T. Wu, Identification of dispersoids in Al-Mg alloys containing Mn, Metallurgical Transactions A 18(8) (1987) 1353-1357.
[32] X.L. Xiao, H.W. Liu, W.L. Chen, Y.M. Lin, Morphology of Dispersoids in an Annealed Al-Mg Alloys, Materials Science Forum 1035 (2021) 72-82.
[33] Y.J. Li, L. Arnberg, Solidification structures and phase selection of iron-bearing eutectic particles in a DC-cast AA5182 alloy, Acta Materialia 52(9) (2004) 2673-2681.
[34] J. Osten, B. Milkereit, C. Schick, O. Kessler, Dissolution and precipitation behaviour during continuous heating of Al-Mg-Si alloys in a wide range of heating rates, Materials 8(5) (2015) 2830-2848.
[35] E. Romhanji, T. Radeti, M. Popovi, Homogenization of an Al-Mg alloy and alligatoring failure alloy ductility and fructure, Materials and technology 50(3) (2016) 403-407.
[36] E. Romhanji, T. Radetić, M. Popović, Homogenization of an Al-Mg alloy and alligatoring failure: influence of the microstructure, Materiali in tehnologije 50(4) (2016) 531-536.

Chapter 3: Effects of AlMn dispersoids and $Al_3(Sc,Zr)$ precipitates on microstructure and ambient/elevated-temperature mechanical properties of hot-rolled AA5083 alloys

Ahmed Y. Algendy [1], Kun Liu [1,], Paul Rometsch [2], Nick Parson [2], X.-Grant Chen [1,]
[1] Department of Applied Science, University of Quebec at Chicoutimi, Saguenay (QC), G7H 2B1, Canada
[2] Arvida Research and Development Center, Rio Tinto Aluminum, Saguenay (QC), G7S 4K8, Canada

This article has been published in:
Material Science and Engineering A 855 (2022) 143950

Abstract

With the addition of Sc and Zr to AA5083 alloy, two populations of strengthening particles (submicron-sized AlMn dispersoids and nanosized $Al_3(Sc,Zr)$ precipitates) precipitate during three-step heat treatment. Here, their influence on the microstructure and mechanical properties of hot-rolled sheets at ambient and elevated temperatures was investigated. The results show that the low-temperature (25–200 °C) tensile properties of the rolled sheets were significantly improved by increasing the Sc and Zr contents. The yield strength (YS) and ultimate tensile strength (UTS) of the alloy with 0.16 wt.% Sc and 0.17 wt.% Zr at ambient temperature reached 295 and 411 MPa, respectively, showing improvements of 30% in YS and 11.8% in UTS compared to the base alloy. However, the YSs of the Sc/Zr-containing alloys at high temperature (300–400 °C) were lower than that of the base alloy. The mechanical properties of both the base and Sc/Zr-containing alloys were thermally stable during long-term thermal exposure at 300 °C for 500 h, demonstrating the great potential of this alloy for various elevated-temperature applications. The characteristics of the AlMn dispersoids and $Al_3(Sc,Zr)$ precipitates after the heat treatment

and hot rolling were examined and quantified using transmission electron microscopy. Their combined contributions toward the YS at 25 and 300 °C were analyzed with the aid of constitutive strengthening equations and compared with experimentally measured values.

Keywords: Aluminum 5083 alloys, Sc and Zr addition, AlMn dispersoids, $Al_3(Sc,Zr)$ precipitates, Mechanical properties, Strengthening mechanism.

3.1 Introduction

Recently, interest in developing a new generation of lightweight aluminum alloys for automotive and aerospace applications has markedly increased. Owing to their excellent combination of high strength-to-weight ratio, good formability, high toughness, and excellent weldability and corrosion resistance, Al–Mg–Mn 5xxx alloys are considered excellent candidates for transportation (automotive, shipbuilding, etc.) and structural components, as well as many other applications [1, 2]. Traditionally, 5xxx aluminum alloys are classified as non-heat-treatable alloys, and their strength can only be achieved by strain hardening and solid-solution strengthening [3, 4]. Therefore, the achievable strength of this alloy series is more limited than that of heat-treatable high-strength aluminum alloys, thus restricting their performance in several applications.

In addition to strain hardening, dispersoid strengthening has recently been identified as a promising approach for improving the mechanical strength of non-heat-treatable aluminum alloys, such as 3xxx alloys [5-8]. Several studies have reported that appropriate heat treatments can promote the precipitation of fine and densely distributed dispersoids, thereby enhancing the ambient- and elevated-temperature mechanical properties [6-9]. A recent study on Al–Mg–Mn 5xxx alloys [10] demonstrated that a multistep heat treatment can be

used to precipitate high volume fractions of submicron-sized AlMn dispersoids and improve the rolling performance and mechanical properties of rolled sheets.

In recent years, Sc, as an effective microalloying element, has often been added to aluminum alloys to enhance their mechanical properties by forming nanosized $L1_2$-Al_3Sc precipitates during aging treatment in the temperature range of 300–425 °C [11-14]. These finely dispersed $L1_2$-Al_3Sc precipitates are fully coherent with the aluminum matrix and exhibit high thermal stability at elevated temperatures (300–350 °C) owing to the low diffusivity of Sc in Al [15, 16]. For industrial applications, cost-effective Zr is often added along with Sc. Zr can substitute with Sc to form core–shell $L1_2$-Al_3(Sc,Zr) precipitates that have better coarsening resistance than Al_3Sc precipitates, thereby improving the recrystallization resistance and elevated-temperature properties [17-20].

In several studies, Sc and Zr have been coadded to improve the mechanical properties of traditional heat-treatable alloys, such as 2xxx, 6xxx, and 7xxx alloys [21-23]. Significant improvements in the room-temperature microhardness and mechanical properties have been reported, mainly owing to the combined strengthening effect of aging strengthening phases (Al_2Cu, Mg_2Si, and $MgZn_2$) and Al_3(Sc,Zr) precipitates. For instance, the coaddition of Sc and Zr increases the tensile strength and high-cycle fatigue strength of AA6106 alloys [21] and noticeably increases the hardness of AA2219 alloys [22]. However, owing to the high coarsening rate of the strengthening phases (Al_2Cu, Mg_2Si, and $MgZn_2$) of heat-treatable alloys at elevated temperatures, most studies on Sc and Sc+Zr additions have focused on the ambient-temperature properties [24, 25], creep behavior of cast alloys [11, 19], or superplastic deformation of processed alloys [26, 27]. In addition, the temperatures for precipitating conventional aging strengthening phases (Al_2Cu, Mg_2Si, and $MgZn_2$) are very

different from those for $Al_3(Sc,Zr)$ precipitates, making the heat treatment of both types of phase incompatible. Therefore, the benefits of microalloying with Sc and Zr and the precipitation of fine and thermally stable $Al_3(Sc,Zr)$ precipitates cannot be fully applied.

In Al–Mg–Mn alloys, the precipitation temperatures of AlMn dispersoids and $Al_3(Sc,Zr)$ precipitates are similar, and both phases are thermally stable and coarsening-resistant, which provides a common basis for improving the ambient- and elevated-temperature properties during heat treatment. However, there is little information on the synergetic effects of these strengthening phases on the elevated-temperature mechanical properties of Al–Mg–Mn 5xxx alloys.

The main objective of this study was to explore the combined effects of two populations of strengthening particles (submicron-sized AlMn dispersoids and nanosized $Al_3(Sc,Zr)$ precipitates) on the mechanical properties of Al–Mg–Mn AA5083 alloys. To clarify the roles of microalloyed Sc and Zr, the microstructural evolution after heat treatment and hot rolling was characterized by several techniques, including optical microscopy, scanning electron microscopy (SEM), and transmission electron microscopy (TEM). The tensile properties of hot-rolled sheets were evaluated at ambient and elevated temperatures. Finally, the experimentally measured yield strengths (YSs) were compared with the analytically calculated ones using constitutive strengthening equations to better understand the strengthening mechanisms of Sc/Zr-containing AA5083 alloys.

3.2 Experimental Procedure

Three Al–Mg–Mn alloys were prepared from commercially pure Al (99.7%) and Mg (99.8%), as well as Al–25% Fe, Al–50% Si, Al–25% Mn, Al–20% Cr, Al–50% Cu, Al–2% Sc, and Al–15% Zr master alloys (all the alloy compositions used in this study were in wt.%). The alloys were denoted as base alloy B (AA5083, Sc/Zr-free), B08 (0.08% Sc and 0.08% Zr), and B15 (0.16% Sc and 0.17% Zr). The materials were melted in a graphite crucible in an electrical resistance furnace. The melting temperature was maintained at 780 °C for 30 min followed by degassing with pure Ar for 15 min. Al–5% Ti–1% B master alloy was added as a grain refiner. Then, the melt was poured into a permanent steel mold preheated at 250 °C to produce cast ingots with dimensions of 30 × 40 × 80 mm. The chemical compositions were analyzed using optical emission spectrometry, and the results are listed in Table 3.1.

Table 3.1: Chemical composition of experimental alloys (wt.%)

Alloys	**Elements, wt.%**								
	Mg	**Mn**	**Si**	**Fe**	**Cu**	**Cr**	**Ti**	**Sc**	**Zr**
B	4.78	0.79	0.26	0.31	0.12	0.14	0.09	---	---
B08	4.76	0.79	0.26	0.35	0.10	0.15	0.10	**0.08**	**0.08**
B15	4.75	0.81	0.31	0.31	0.11	0.15	0.09	**0.16**	**0.17**

To promote the precipitation of AlMn dispersoids and $Al_3(Sc,Zr)$ precipitates [10, 28] the cast ingots were heat-treated using a three-step heat treatment (275 °C/12 h + 375 °C/48 h + 425 °C/12 h) followed by water quenching to room temperature. The first two steps of low-temperature heat treatment (275 °C/12 h + 375 °C/48 h) were designed based on our previous work [10] to maximize the precipitation of AlMn disperosids and $Al_3(Sc,Zr)$ precipitates. The third step heat treatment at 425°C/12h was to ensure the full dissolution of the low

eutectic melting phases for a better rolling performance while minimizing the coarsening of AlMn dispersoids and Al_3(Sc,Zr) precipitates. Subsequently, the heat-treated ingots were machined to 25 mm thick and then hot rolled to a final sheet thickness of 3.2 mm (87% reduction in thickness) using a laboratory-scale rolling mill. Multiple hot-rolling passes were carried out at a temperature of 500 ± 10 °C. Before mechanical tests, all rolled sheets were annealed at 300 °C for 5 h to relieve the residual stress generated during rolling.

The tensile properties at room temperature were measured using Instron 8801 servo-hydraulic testing unit at strain rate 0.5 mm/min. The tensile samples of rolled plates were machined according to ASTM E8/E8M-16a in the rolling direction with a 3 x 6 mm gauge area. The tensile properties at 300 ^{o}C were measured on a Gleeble 3800 thermomechanical testing unit at a strain rate of 0.001 s^{-1}, in which the tensile samples were heated to 300 ^{o}C with a heating rate of 2 ^{o}C/sec and then holding 180 s prior to tensile loading. Average results were reported from three tests in a given condition.

Samples for microstructural observations were prepared using a standard metallographic procedure. The grain structure was observed using an optical microscope (Nikon, Eclipse ME600) under polarized light after electro-etching with Barker's agent (3 vol.% HBF_4 solution) at 15 V for 3 min. After heat treatment or rolling, the samples were etched in 0.5% HF for 30 s to reveal the general distribution of AlMn dispersoids. The grain and subgrain structures after rolling were characterized using electron backscatter diffraction (EBSD). The EBSD samples were sectioned from the gauge of the tensile samples, parallel to the rolling and tensile deformation directions. A transmission electron microscope (JEM-2100) operated at 200 kV was used to observe the distribution of AlMn dispersoids and Al_3(Sc,Zr) precipitates in detail. All TEM images were obtained along the $[001]_{Al}$ zone axis to observe

the AlMn dispersoids To clearly reveal the $Al_3(Sc,Zr)$ precipitates, centered superlattice dark-field images were recorded along the [100] reflections close to the <011> direction. The characteristics of the AlMn dispersoids and $Al_3(Sc,Zr)$ precipitates were quantified from the TEM images using ImageJ image analysis software. The quantitative analysis was performed on 10 images, and each image contains more than 300 particles. The number density N_d and volume fraction V_f of AlMn dispersoids were determined using the following equations [7, 11]:

$$N_d = \frac{N}{A(D+t)} \quad (1)$$

$$V_f = A_A \frac{K\bar{D}}{K\bar{D}+t}(1 - A_{DFZ}) \quad (2)$$

Where N is the number of particles; A and $\bar{D}$ are the total area and the equivalent diameter of the particles, respectively; t is the thickness of the TEM foil; A_A is the area fraction of dispersoids in the TEM image; K is the average shape factor of dispersoids equal to 0.45 [9]; A_{DFZ} is the area fraction of DFZ measured in the optical images.

3.3 Results

3.3.1 As-cast and heat-treated microstructures

Fig. 3.1 shows the grain structure and distribution of intermetallic phases in the as-cast alloys. All three alloys had equiaxed grain structures (Fig. 3.1a and b). The average grain size of alloy B was 64.8 μm, whereas those of alloys B08 and B15 were 60.8 and 54 μm, respectively. This reduction in grain size results from the grain-refining effect of the Sc+Zr addition [24, 29, 30]. As shown in Fig. 3.1c and d, the as-cast alloys contained α-Al dendritic cells with several intermetallic phases distributed at the dendrite boundaries. The dominant

intermetallic compounds (IMC) in all three alloys were Fe/Mn-rich α-$Al_{15}(Fe,Mn,Cr)_3Si_2$ and $Al_6(Fe,Mn,Cr)$ intermetallics and primary Mg_2Si intermetallics (dark color), as identified by SEM–energy dispersive X-ray spectroscopy (SEM-EDS) analysis. A small amount of low-melting-point τ-Al_6CuMg_4 eutectic phase was also detected in the interdendritic regions. Interestingly, the amount of intermetallic phases increased significantly with the addition of Sc and Zr. The results of image analysis confirmed that the area fraction of Fe/Mn-rich intermetallics (α-$Al_{15}(Fe,Mn,Cr)_3Si_2$ and $Al_6(Fe,Mn,Cr)$) increased from 1.98% in alloy B to 2.31% in alloy B08 and further to 3.14% in alloy B15, while the area fraction of primary Mg_2Si intermetallics increased from 0.7% in alloy B to 0.77% in alloy B08 and further to 0.9% in alloy B15. This could be attributed to the decreased solubility of Mn and Mg owing to the addition of Sc and Zr [11, 31].

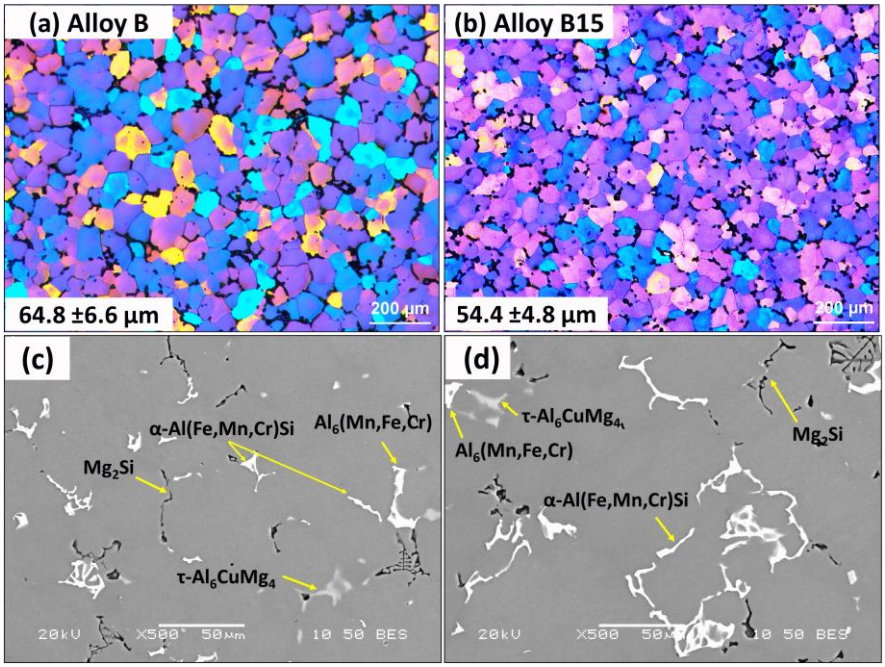

Figure 3.1: Optical images showing the grain structures of (a) alloy B and (b) alloy B15, and SEM backscattered images showing the distribution of intermetallic phases of (c) alloy B and (d) alloy B15 in the as-cast condition.

Fig. 3.2 shows the typical microstructures of the three alloys after the three-step heat treatment. As shown in the optical images (Fig. 3.2a-c), a large number of dispersoids formed in the dendritic cells during heat treatment, appearing as dispersoid zones (DZ, dark areas marked with red lines). In addition, dispersoid-free zones (DFZ, light area marked with blue lines) were observed in the interdendritic regions surrounding the intermetallic phases. It should be noted that complete dissolution of the low-melting-point τ-Al_6CuMg_4 eutectic phase and partial dissolution of the primary Mg_2Si intermetallics occurred during the heat treatment. Bright-field TEM images (Fig. 3.2d-f) revealed the precipitation of submicron-sized AlMn dispersoids with cube- and rod-like morphologies in the DZs. The AlMn dispersoids were identified as Al_4Mn (cube-like) and Al_6Mn (rod-like) by TEM-EDS and selected area diffraction patterns in our previous work [10]. The equivalent diameter of the AlMn dispersoids in base alloy B was ~25 nm, and the number density was ~560 μm^{-3}. However, with increasing Sc and Zr contents in alloys B08 and B15, the size of the dispersoids increased and the number density decreased compared to that in alloy B (Fig. 3.2g).

In addition to the AlMn dispersoids, a large number of nanosized Al_3(Sc,Zr) precipitates were formed in alloys B08 and B15, as shown in the dark-field TEM images (Fig. 3.2h and i). The Al_3(Sc,Zr) precipitates were uniformly distributed in the Al matrix and were much finer and denser than the AlMn dispersoids. A summary of the two populations of particles is shown in Fig. 3.2g. This figure shows that the addition of Sc and Zr caused the following microstructural changes: 1) a high number of nanosized Al_3(Sc,Zr) precipitates coexisted with AlMn dispersoids, 2) the size of the AlMn dispersoids increased and the number density (Nd) of dispersoids decreased, and 3) the area fraction of DFZs increased.

There are two possible reasons for the increased size and decreased number density of dispersoids in alloys B8 and B15. First, the addition of Sc and Zr lowers the solubility of Mn, Mg, and Si in the aluminum matrix [11, 15, 31-34]. Therefore, the addition of Sc and Zr would promote the formation of Fe/Mn-rich intermetallics, thereby increasing their volume fraction. Consequently, the amount of supersaturated Mn in the α-Al solid solution would be reduced, leaving less Mn available for the formation of AlMn dispersoids upon heat treatment. The other reason is that the addition of Sc and Zr decreases the nucleation efficiency of AlMn dispersoids during heat treatment.

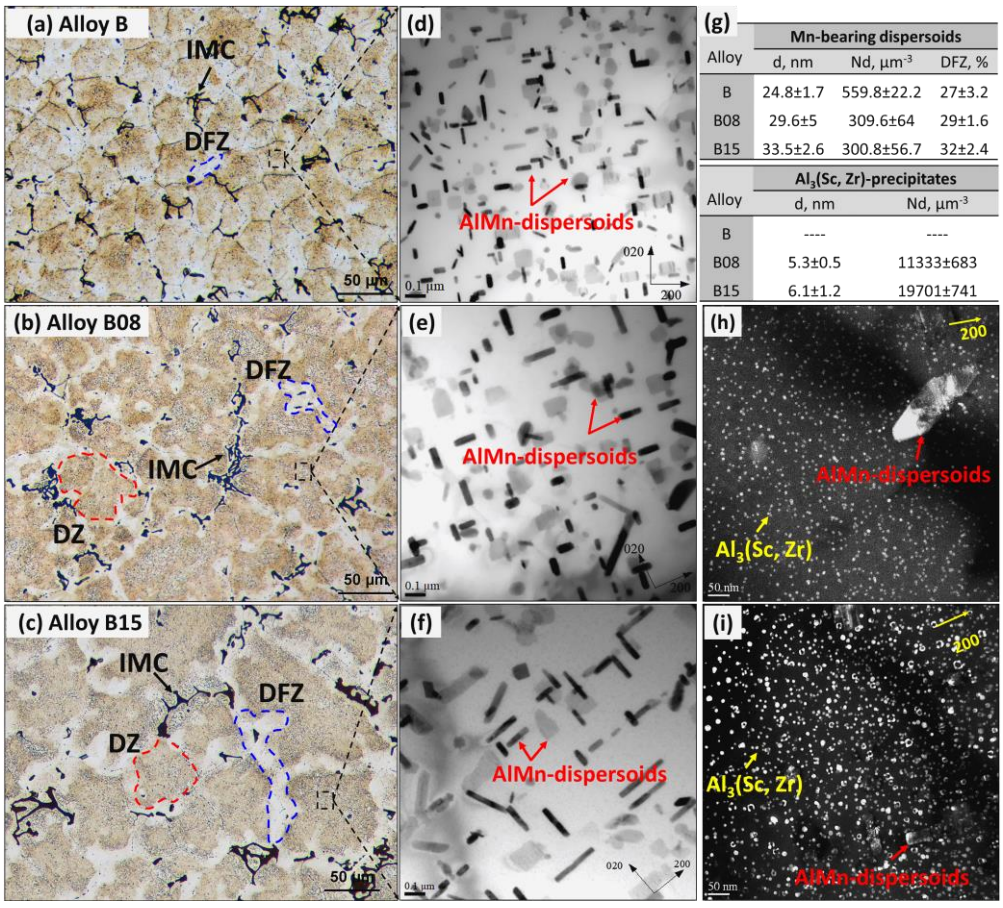

(g)

Alloy	Mn-bearing dispersoids		
	d, nm	Nd, μm^{-3}	DFZ, %
B	24.8±1.7	559.8±22.2	27±3.2
B08	29.6±5	309.6±64	29±1.6
B15	33.5±2.6	300.8±56.7	32±2.4

Alloy	Al_3(Sc, Zr)-precipitates	
	d, nm	Nd, μm^{-3}
B	----	----
B08	5.3±0.5	11333±683
B15	6.1±1.2	19701±741

Figure 3.2: Typical microstructures after heat-treatment: (a, b, c) optical images and (d, e, f) bright-field TEM images showing the distribution of AlMn dispersoids for alloys B, B08 and B15, respectively; (h, i) dark-field TEM images showing the distribution of Al_3(Sc,Zr) precipitates for alloys B08 and B15; (g) characteristics of two population of particles (AlMn dispersoids and Al_3(Sc,Zr) precipitates).

As reported previously [9, 10, 35, 36], metastable β′-Mg_2Si phases may act as nucleation sites for the precipitation of AlMn dispersoids. Owing to the reduced solubility of Mg and Si, more Mg and Si would be consumed to form primary Mg_2Si particles during solidification, lowering their supersaturation levels in the α-Al matrix. Therefore, during the heating process and first step of the heat treatment (i.e., 275 °C/12 h), a lower number of β′-Mg_2Si particles would form in the Sc/Zr-containing alloys than in the base alloy, resulting in a lower number density of AlMn dispersoids being precipitated in the subsequent heat treatment step.

3.3.2 Microstructures after hot rolling

After heat treatment, all three alloys were hot rolled at 500 °C. The typical microstructures after hot rolling are illustrated in Fig. 3.3. Owing to the high deformation ratio (87% reduction), the intermetallic particles were fragmented and aligned in the rolling direction, and the grains were also elongated in the rolling direction, as shown in Fig. 3.3a-c. Bright-field TEM images (Fig. 3.3d-f) revealed that the AlMn dispersoids coarsened during hot rolling; compared to the heat-treated alloys, the size of the dispersoids was increased, and their number density was remarkably decreased (Fig. 3.2). The quantitative results in Table 3.2 show that the number density of AlMn dispersoids decreased after hot rolling by 59%, 80%, and 79% for alloys B, B08, and B15, respectively. Base alloy B still exhibited the highest number density of dispersoids among the three alloys.

A similar coarsening trend was observed for the $Al_3(Sc,Zr)$ precipitates in alloys B08 and B15 after hot rolling, as shown in Fig. 3.3g and h. The fine and spherical $Al_3(Sc,Zr)$ particles became larger and less dense than those in the heat-treated samples. For instance, the number density sharply dropped from 11333 to 2718 μm^{-3} in alloy B08 and from 19701

to 5695 μm^{-3} in alloy B15 (Fig. 3.2 and Table 3.2), representing reductions of 76% and 71%, respectively. The lower density and larger size of the Mn-bearing dispersoids and $Al_3(Sc,Zr)$ precipitates are predominantly attributed to the high rolling temperature (500 °C), at which both AlMn dispersoids and $Al_3(Sc,Zr)$ precipitates are no longer thermally stable [7, 12, 14, 16, 17, 37]. In addition, the high number density of dislocations generated during rolling accelerates the diffusion of alloying elements in the matrix, resulting in the growth and coarsening of both types of particles [38-40].

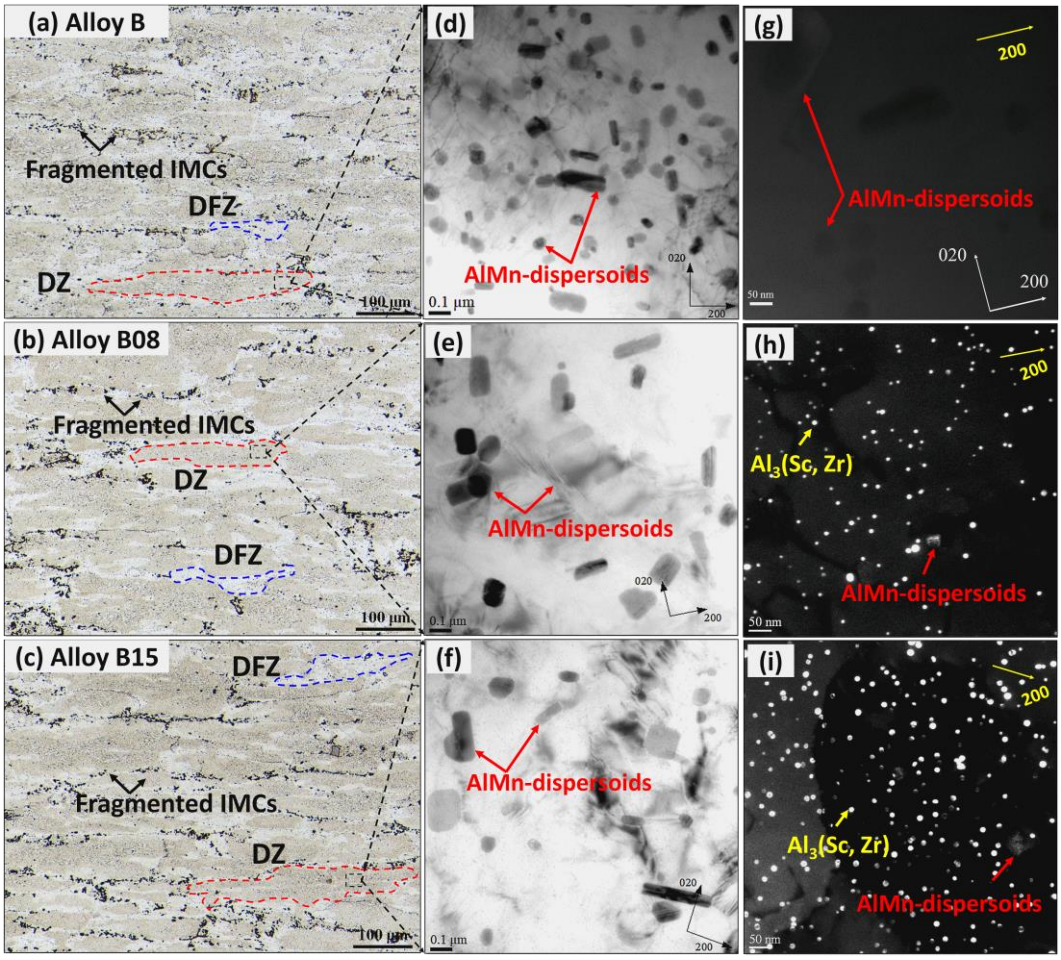

Figure 3.3: Typical microstructures of the hot-rolled samples: (a, b, c) OM images and (d, e, f) bright-field TEM images showing the distribution of AlMn dispersoids for alloys B, B08 and B15, respectively; (g, h) dark-field TEM images showing the distribution of $Al_3(Sc,Zr)$ precipitates for alloys B08 and B15.

Table 3.2: Quantitative TEM results of AlMn dispersoids and $Al_3(Sc,Zr)$ precipitates after rolling.

Alloy	AlMn dispersoids			$Al_3(Sc,Zr)$ precipitates		
	d (nm)	N_d (μm^{-3})	V_f (%)	d (nm)	N_d (μm^{-3})	V_f (%)
B	32.4±0.2	231±46	1.4	--	--	--
B08	57.2±0.6	60.1±9.6	1.02	11.9±0.5	2718±385	0.19
B15	56.0±0.6	64.8±13.3	1.06	12.6±0.4	5695±297	0.49

3.3.3 Mechanical properties of hot-rolled sheets at ambient and elevated temperatures

Fig. 3.4 shows the ambient-temperature tensile properties of all three hot-rolled alloys. The addition of Sc and Zr significantly improved the alloy strength, while the elongation decreased. Fig. 3.4a displays typical engineering stress–strain curves; after reaching the peak stress (ultimate tensile strength (UTS)), the curve underwent a short plateau followed by an instantaneous drop. As shown in Fig. 3.4b, the tensile strength increased with increasing Sc content, and alloy B15 exhibited the highest YS and UTS at 295 and 411 MPa, respectively. These values are 30% and 11.8% higher, respectively, than those for base alloy B. On the other hand, in low-Sc alloy B08, the YS and UTS were 262 and 392 MPa, respectively, representing an improvement of 14% and 3%, respectively, relative to those of base alloy B. The increase in tensile strength via the addition of Sc and Zr was mainly due to the introduction of fine and coherent $Al_3(Sc,Zr)$ precipitates as an additional strengthening phase (Fig. 3.3).

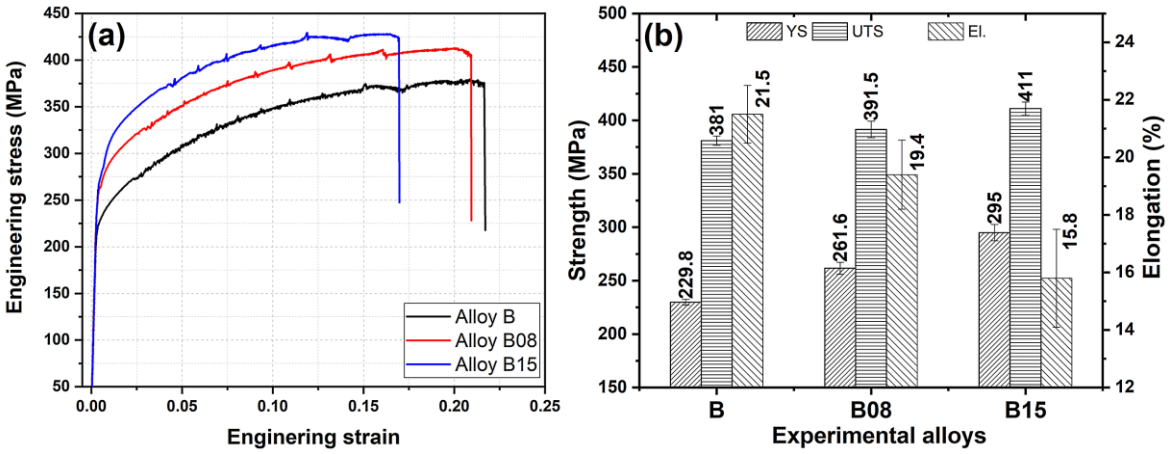

Figure 3.4: (a) Typical engineering stress-strain curves of experimental alloys and (b) tensile properties at ambient temperature for three hot-rolled alloys.

The elevated-temperature tensile properties of the hot-rolled alloys are shown in Fig. 3.5. Fig. 3.5a shows the engineering stress–strain curves measured at 300 °C. Shortly after tensile loading, the curves of all alloys quickly rose to the maximum stress (UTS) and then gradually decreased until reaching a strain of 0.6–0.7. It is apparent that the elevated-temperature ductility of the alloys is no longer a concern because the elongation of all three alloys exceeded 60%. As shown in Fig. 3.5b, the UTS of both Sc/Zr-containing alloys (99 MPa) was only slightly lower than that of the base alloy (104 MPa). However, the YSs of both B08 and B15 alloys (66 MPa) were significantly lower than that of alloy B (88 MPa). This is equivalent to a 24% reduction in YS compared to that of the Sc-free base alloy. Notably, this trend is completely different from that at ambient temperature. In addition, although alloy B15 contained more $Al_3(Sc,Zr)$ precipitates (Table 3.2), the YS and UTS of alloys B08 and B15 were almost the same.

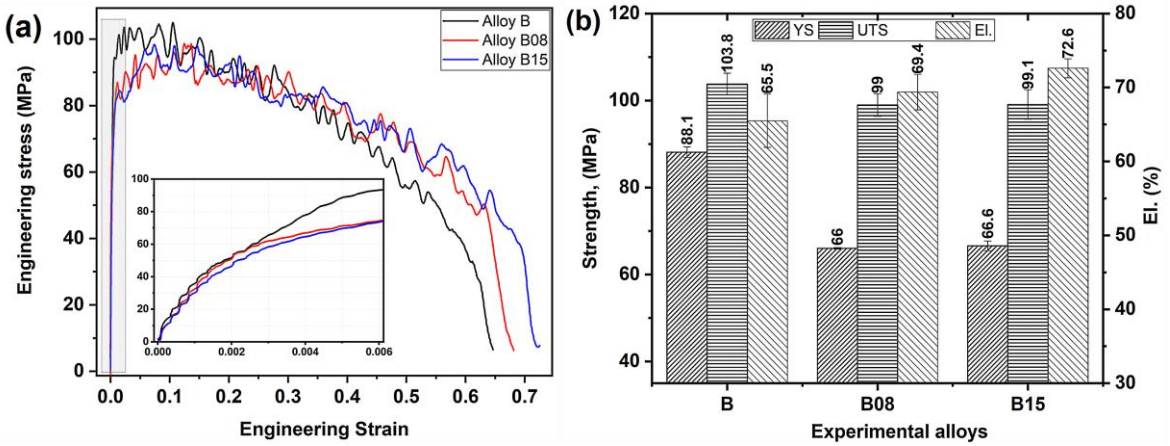

Figure 3.5: (a) Typical engineering stress-strain curve of experimental alloys and (b) tensile properties at 300 ^{o}C.

Al-Mn-Mg 5xxx alloys could be serviced at a wide rang of temperatures for transportation and other structural components. For example, AA5083 alloys are increasingly used in load-bearing structural applications, such as land-based vehicles, marine crafts and building structure. However, one of the major concerns in the design of land-based and marine aluminum structure is fire safty, in which the temperature of aluminum structure could reach above 400 ^{o}C during an unintentional fire [41]. To better understand the effect of temperature on the tensile properties, all three hot-rolled alloys were subjected to tensile tests at temperatures of 25–400 °C, and the tensile properties are presented in Fig. 3.6. As expected, the tensile strengths decreased gradually with increasing test temperature for all three alloys. At 25–200 °C, the Sc/Zr-containing alloys (B08 and B15) exhibited higher tensile strengths (both YS and UTS) than base alloy B, and the YS and UTS increased with increasing Sc content. At 250 °C, alloys B and B08 had similar YS (150 vs. 147.2 MPa), but alloy B15 showed noticeably lower YS of 123.2 MPa (Fig. 3.6a). As the testing temperature increased to 300–400 °C, although the YS of the Sc/Zr-containing alloys (B08 and B15) remained equal, the YS became considerably lower than that of base alloy B. For instance, at 400 °C, both alloys B08 and B15 had a YS of 21 MPa, which was lower than that of base

alloy B (32 MPa). The UTS showed a slightly different trend from that of the YS (Fig. 3.6b). At relatively low temperatures (25–200 °C), the UTSs of the Sc/Zr-containing alloys were higher than that of alloy B. However, at 250 °C, the UTSs of all three alloys were almost the same. At higher temperatures (300–400 °C), the UTSs of all three alloys were still very close.

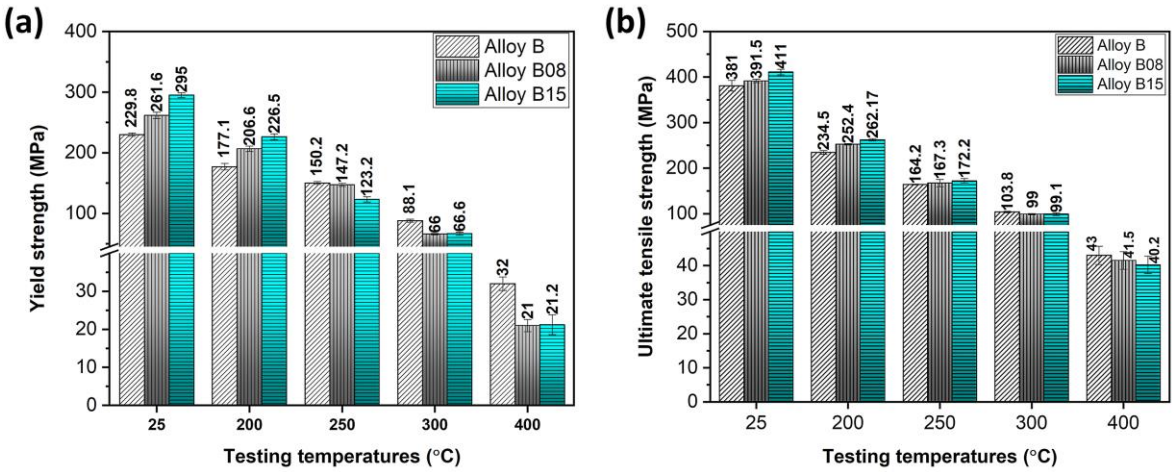

Figure 3.6: (a) YS and (b) UTS of experimental alloys as a function of testing temperatures.

The thermal stability of the mechanical properties is an important consideration for aluminum alloys that can potentially be used at elevated temperatures. Therefore, the thermal stability of two of the hot-rolled alloys (B and B15) was evaluated by exposing them at 300 °C for up to 500 h. The tensile strengths at 25 and 300 °C as a function of the exposure time are displayed in Fig. 3.6. Both the YS and UTS remained unchanged after long-term thermal exposure of up to 500 h for both alloys. For instance, the YSs at 25 °C remained at 230 MPa for alloy B and 295 MPa for alloy B15, while the elevated-temperature YSs were stable at 85 MPa (alloy B) and 68 MPa (alloy B15) throughout the entire long-term thermal exposure. These results confirm the excellent thermal stability and low coarsening kinetics of AlMn

dispersoids and $Al_3(Sc,Zr)$ precipitates at 300 °C for Al-Mg-Mn alloys strengthened by both types of particles.

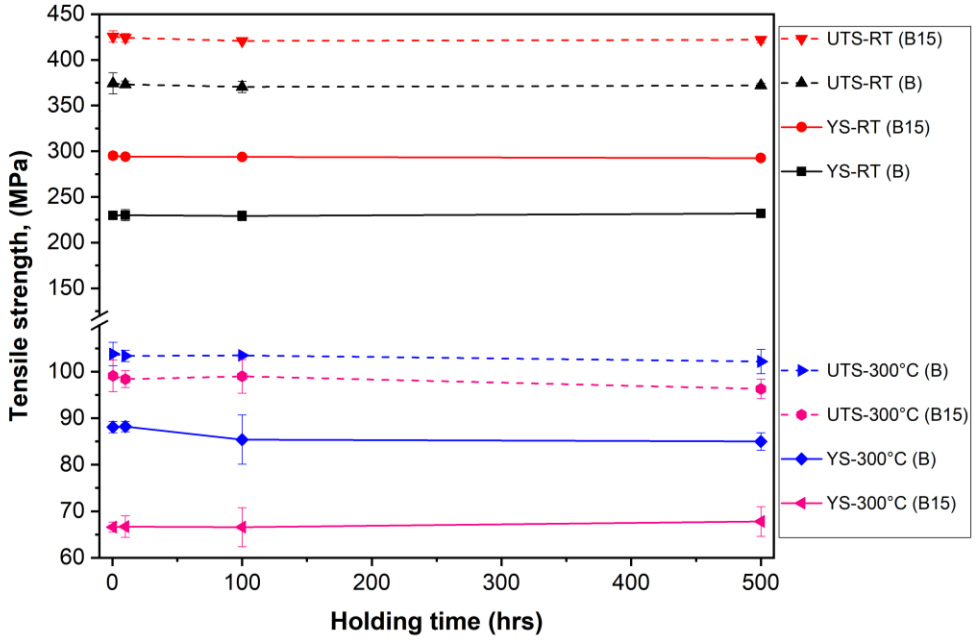

Figure 3.7: Evolution of YS and UTS of alloys B and B15 tested at 25 ^{o}C and 300 ^{o}C as a function of the time of thermal exposure at 300 ^{o}C.

3.4 Discussion

3.4.1 Strengthening model at ambient and elevated temperatures

The overall mechanical strength of aluminum alloys is determined by the stress required to overcome various obstacles during deformation. Several strengthening mechanisms are operative, including solid-solution strengthening, grain-boundary strengthening, and particle strengthening. To better understand the strengthening effect of the two distinct groups of particles (AlMn dispersoids and $Al_3(Sc,Zr)$ precipitates) at ambient and elevated temperatures, the YSs of the experimental Al–Mg–Mn alloys were quantitatively studied using constitutive equations. Assuming that the contributions of the strengthening

mechanisms are independent and can be linearly added, the overall YS can be expressed as follows:

$$\Delta\sigma_{YS} = \sigma_o + \Delta\sigma_{SS} + \Delta\sigma_{GB} + \Delta\sigma_{dispersoids} + \Delta\sigma_{precipitates} \quad (3)$$

where $\Delta\sigma_{YS}$ is the overall yield strength, σ_o is the strength of the pure Al matrix, and $\Delta\sigma_{SS}$, $\Delta\sigma_{GB}$, $\Delta\sigma_{dispersoids}$, and $\Delta\sigma_{precipitates}$ are the strengthening contributions of solid-solution strengthening, grain-boundary strengthening, the AlMn dispersoids, and the Al_3(Sc,Zr) precipitates.

3.4.1.1 Strengthening mechanisms at ambient temperature

The yield strength of the Al matrix was considered to be 34 MPa, as taken from an annealed pure 1100-O Al alloy [11]. The solid-solution strengthening of AA5083 alloys is mainly attributed to Mg and Mn; the other elements have a negligible contribution owing to their small contents. Mg is primarily consumed by primary Mg_2Si and the low-melting-point τ-Al_6CuMg_4 eutectic phase. After heat treatment and hot rolling, the τ-Al_6CuMg_4 eutectic phase was entirely dissolved, and Mg_2Si was mostly dissolved. By measuring the remaining volume fraction of Mg_2Si, the availability of Mg solutes in the solid solution was estimated. The consumption of Mn is strongly related to the formation of Fe/Mn-rich intermetallics and AlMn dispersoids. Therefore, the Mn concentration in the aluminum matrix can be assessed based on their volume fractions after hot rolling. The strengthening contributions of Mg and Mn were calculated using Eq. 4 [3, 4].

$$\Delta\sigma_{ss} = KC^n \quad (4)$$

where C is the concentration of solute atoms (wt.%), K_{Mg} = 13.8 MPa/wt.%, n_{Mg} = 1.14, K_{Mn} = 18.35 MPa/wt.%, and n_{Mn} = 0.9 [3]. The calculation showed that the strengthening effects caused by Mg and Mn solutes were 77 and 3.5 MPa, respectively (Table 3.3).

The contribution of grain boundary strengthening to the YS was predicted using the Hall–Petch equation [3]:

$$\sigma_{GB} = K_y/(d_{GB})^{0.5} \quad (5)$$

where K_y is the Hall–Petch constant, which is typically considered to be 0.22 MPa/m$^{0.5}$ for Al–4 wt.% Mg alloys [3] and d_{GB} is the average grain size of the hot-rolled samples, which was measured in optical microscopy on electro-etched samples with polarized light using the intercept method according to ASTM E112-12 (Non-equiaxed grain). The measured average grain sizes of alloys B, B8, and B15 were 64.8, 64.2, and 59.4 μm, respectively.

For the precipitation strengthening mechanism, the contribution of the two types of particles (AlMn dispersoids and Al_3(Sc,Zr) precipitates) to the ambient-temperature YS can be explained and predicted using the classical Orowan bypass mechanism because of their relatively large size [19]. Therefore, the contributions of both types of strengthening particle were calculated using Eqs. 6 and 7 [11, 19, 42, 43].

$$\Delta\sigma_{dispersions} = \frac{0.84MGb}{2\pi(1-\upsilon)^{0.5}\lambda}\ln\left(\frac{r}{b}\right) \quad (6)$$

$$\lambda = r\,(\frac{2\pi}{3V_f})^{0.5} \quad (7)$$

where M (= 3) is the Taylor factor, G (= 27.4 GPa) is the shear modulus of the Al matrix, b (= 0.286 nm) is the Burgers vector, υ (= 0.33) is Poisson's ratio, λ is the effective interparticle spacing, r is the equivalent average radius of the dispersoids/precipitates, and V_f is the volume fraction of particles [11, 19, 43].

Using the data in Table 3.2 and Eqs. 6 and 7, the increments in YS due to the presence of AlMn dispersoids and Al_3(Sc,Zr) precipitates were computed (Table 3.3). In the present work, the addition of Sc and Zr increased the dispersoid-free zone of AlMn dispersoids and hence reduced the volume fraction of AlMn dispersoids (Fig. 3.2 and Table 3.2). In the base alloy B, AlMn dispersoids provided an increment of 80.1 MPa to the YS of the base alloy B. However, with the addition of Sc and Zr in two Sc/Zr-containing alloys, the YS increment due to AlMn dispersoids decreased by a factor of two because the addition of Sc and Zr significantly decreased the number density and volume fraction of dispersoids (Fig. 3.3, Table 3.2). On the other hand, although the volume fraction of the Al_3(Sc,Zr) precipitates was not so high, because of their fine nanosize and large number density, their strengthening effect was very strong at ambient temperature according to Eq. 6. The decrease in YS increment from the AlMn dispersoids in the two Sc/Zr-containing alloys was compensated by Al_3(Sc,Zr) precipitates. Owing to the coexistence of the two types of particles, the contribution of particle strengthening is higher in alloys B08 and B15 than that in the base alloy.

As shown in Table 3.3, in the case of the Sc-free base alloy, the highest contribution to the YS is from AlMn dispersoids (80 MPa), followed by the Mg solid solution (77 MPa). In the two Sc/Zr-containing alloys, B08 and B15, precipitation strengthening due to the coexisting AlMn dispersoids and Al_3(Sc,Zr) precipitates provided the largest contribution in

strength, with the strengthening contribution of the $Al_3(Sc,Zr)$ precipitates exceeding that of the AlMn dispersoids.

Fig. 3.8a shows a comparison of the predicted and experimentally measured YSs for all three alloys. Although the predicted YSs were slightly lower than the measured ones, the general trend agreed well between the predicted and experimental results. Consequently, the constitutive equation is suitable for predicting the YS of deformed samples containing different types of precipitates.

Table 3.3: Predicted YS contributions and experimentally measured YS at 25 ^{o}C (MPa)

Alloy	**B**	**B8**	**B15**
Al matrix (1100-O)	34	34	34
Mg solid solution	76.8	75.7	74.4
Mn solid solution	3.5	3.5	2.3
Grain boundary	27.3	27.4	28.5
AlMn dispersoids	80.1	43.2	44.7
$Al_3(Sc,Zr)$ precipitates	---	59.3	89.8
Predicted YS	221.7	243.1	273.9
Experimental results	229.8	261.6	295

3.4.1.2 Strengthening mechanisms at elevated temperature (300 ^{o}C)

Owing to a lack of high-temperature data and appropriate constitutive equations, the elevated-temperature strengthening mechanisms are less well-understood than those at ambient temperature. A few studies have used different approaches to predict the elevated-temperature strength [11, 19, 44]. It is difficult to estimate the contributions of solid-solution

and grain-boundary strengthening at elevated temperatures using Eqs. 4 and 5. To simplify the case and focus on the main factor (i.e., precipitation strengthening), the available YS data for AA5083-O at 315 °C (52 MPa) [45] was used as a close approximation for the matrix, solid solution, and grain boundary contributions at 300 °C.

The elastic interaction between dislocations and coherent precipitates causes repulsive stress that hinders dislocation motion [44, 46]. However, at high temperatures, the induced thermal energy allows dislocations to overcome this repulsive stress by enabling dislocation climb. Owing to their size range, the dislocation climb mechanism was considered to better estimate the strength contribution of the nanosized Al_3(Sc,Zr) precipitates [11, 46]. The strength increment caused by dislocation climb strengthening ($\Delta\sigma_{\text{Climb}}$) is the sum of the modulus and lattice mismatch strength increments ($\Delta\sigma_{\text{MMC}}$ *nad* $\Delta\sigma_{\text{LMC}}$*)* according to Eqs. 8 and 9 [44, 46].

$$\Delta\sigma_{Climb\ (\text{Al3(Sc,Zr)})} = \Delta\sigma_{MMC} + \Delta\sigma_{LMC} \tag{8}$$

$$\Delta\sigma_{Climb} = 0.0055M'\Delta G^{1.5}\left(\frac{2V_f}{G_m}\right)^{0.5}\left(\frac{r}{b}\right)^{\frac{3m}{2}-1} + \chi M'(\varepsilon)^{1.5}G_m\left(\frac{2V_f r}{b}\right)^{0.5} \tag{9}$$

where M' (= 3.06) is the mean matrix orientation factor; G_{m} (= 21.1 GPa) is the shear modulus of the Al matrix at 300 °C; ΔG (= $G_{\text{p}} - G_{\text{m}}$) is the difference in modulus between the matrix and precipitates, where G_{p} (= 66.2 GPa) is the shear modulus of the precipitates; b (= 0.288 nm) is the Burgers vector; υ (= 0.33) is Poisson's ratio; χ (= 2.6) and m (= 0.85) are constants; ε is the contrained strain) mainly related to the lattice parameter misfit between the

precipitates and the matrix [19, 44]; r is the equivalent average radius of the particles; and V_f is the volume fraction of the particles [44, 46]

Because the size of AlMn dispersoids is relatively large, their predominant strengthening mechanism is Orowan bypass strengthening [46]. Thus, the YS contribution of the AlMn dispersoids at elevated temperatures can still be estimated using Eqs. 6 and 7, considering only the change in the shear modulus of the matrix, G_m, from 27.4 GPa (25 °C) to 21.1 GPa (300 °C).

Table 3.4 displays the calculated YS increments of the AlMn dispersoids and Al_3(Sc,Zr) precipitates, and Fig. 3.8b shows a comparison of the predicted and experimental YS values at 300 °C. Compared to their contribution at room temperature, the strengthening increments of the AlMn dispersoids and Al_3(Sc,Zr) precipitates decreased by a factor of two at 300 °C for all three alloys. This was attributed to the change in the shear modulus (G_m) and the sufficient thermal energy at elevated temperatures. In the Sc/Zr-containing alloys, B08 and B15, it was predicted that the total contribution of the coexisting AlMn dispersoids and Al_3(Sc,Zr) precipitates was higher than the contribution of AlMn dispersoids to base alloy B. However, the experimentally measured YSs exhibited the opposite trend; that is, the measured YSs of B08 and B15 were considerably lower than that of base alloy B. The experiment results suggested that the strengthening mechanism of Al_3(Sc,Zr) precipitates at elevated temperature was much weaker than that at ambient temperature. At high temperature, the dislocations can much easily climb through the nanosized Al_3(Sc,Zr) precipitates. The decrease in YS due to the reduced volume fraction of AlMn dispersoids in the two Sc/Zr-containing alloys could no longer compensated by Al_3(Sc,Zr) precipitates. The other reasons for the lower YS in B08 and B15 alloys are explored in the following section.

Table 3.4: Predicted YS contributions and experimentally measured YS at 300 °C (MPa)

Alloy	B	B08	B15
AA 5083-O	52	52	52
AlMn dispersoids	40.3	22.5	23.1
$Al_3(Sc,Zr)$ precipitates	---	19.6	32.3
Predicted YS	92.3	94.1	107.4
Experimental results	88	66	67

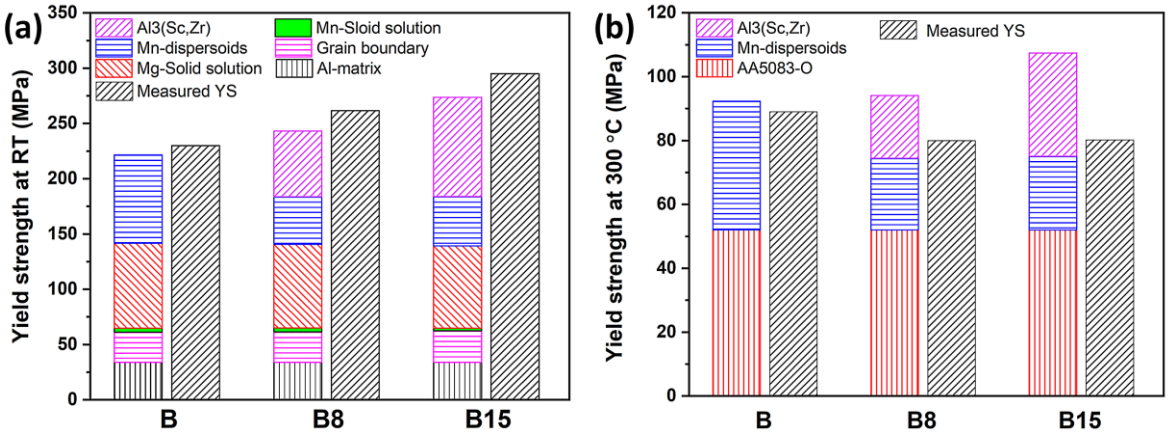

Figure 3.8: Comparison between predicted and experimental yield strengths for three alloys, (a) at ambient temperature and (b) at 300 °C.

3.4.2 Other factor influencing the elevated-temperature yield strength

As shown in Fig. 3.8a, the predicted ambient-temperature YSs agreed well with the experimental results. However, there was a large discrepancy between the predicted and experimental YSs at 300 °C for both Sc/Zr-containing alloys (B08 and B15) (Fig. 3.8b). In fact, the Sc/Zr-containing alloys had considerably lower YSs at 300 °C than the Sc-free base alloy (Fig. 3.5b). The most likely reason for this discrepancy at 300 °C is the difference in grain structure between the base alloy and Sc/Zr-containing alloys. Fig. 3.9a and b show the

grain structures of alloys B and B15 after hot rolling, prior to tensile testing. The deformed grains were partially recrystallized in both alloys, presenting a mixture of recrystallized grains along the grain boundaries and elongated deformed grains in the rolling direction. In alloy B, the recrystallized grains were coarse, with an average size of 25 μm, and were randomly grown in the deformed grains. However, in alloy B15, there were often chains of tiny recrystallized grains with an average size of 8.4 μm along the grain boundaries.

At relatively low temperatures (25–200 °C), the fine recrystallized grains in the Sc/Zr-containing alloys can provide additional strengthening by retarding dislocation motion and grain rotation. In general, the difference in recrystallized grain size and distribution may not significantly affect the tensile strength. Therefore, the predicted ambient-temperature YSs matched well with the measured values for all three alloys.

However, at high temperatures (300 °C and up with sufficient thermal activation energy), the large numbers of fine recrystallized grains in the Sc/Zr-containing alloys, which covered large areas of the grain boundaries, became a major softening source by 1) acting as a vast channel for dislocation movement and vacancy diffusion [47, 48] and 2) facilitating localized deformation along the grain boundaries during tensile deformation. Grain boundary sliding has been reported as an operative deformation mechanism for fine-grained aluminum alloys at elevated temperatures and low strain rates [49, 50]. Griffiths *et al*. [51] reported that grain boundary sliding due to fine equiaxed grains in heat-treated Al–2.9 wt.% Mg–2.1 wt.% Zr alloy results in a significant drop in the YS at temperatures above 150 °C compared to that of the as-fabricated condition which comprises coarse columnar grains, although the ambient-temperature YS of the heat-treated alloy was always higher than that of the as-fabricated alloy. Therefore, it is reasonable to believe that the existence of many tiny

recrystallized grains along the grain boundaries could reduce the YS at 300 °C to a large extent compared with the coarse recrystallized grain structure of alloy B owing to grain boundary sliding.

Fig. 3.9c and d show the grain structures of alloys B and B15, respectively, after tensile testing at 300 °C. Dynamic recrystallization continued heavily in alloy B during the tensile test at 300 °C, resulting in an increased recrystallization volume with coarse quasi-equiaxed grains. In this case, grain boundary sliding would be relatively weak. Therefore, the predicted and experimental YSs at 300 °C for alloy B were in good agreement (Fig. 3.8b). However, in alloy B15, a large number of tiny recrystallized grains still existed along the grain boundaries and even worsened during the tensile test owing to the restricting effect of Al_3(Sc,Zr) precipitates on the coarsening of recrystallized grains. Consequently, grain boundary sliding would be activated and become much more pronounced than that in base alloy B. This explains the large reduction in YS of the Sc/Zr-containing alloys at 300 °C and the unexpected discrepancy between the predicted and experimental values (Fig. 3.8b). However, it seems that the grain boundary sliding had a much less impact on the elevated-temperature UTSs, as the UTSs at 300–400 °C of all three alloys were very close (Figs. 3.5 and 3.6b).

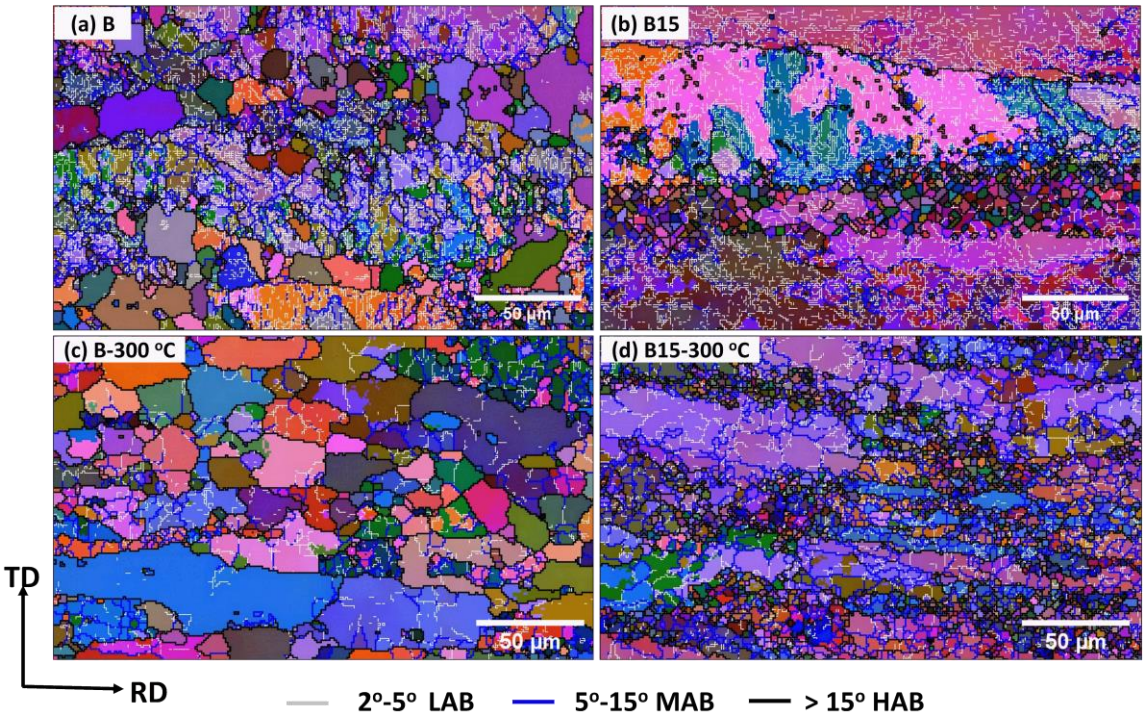

Figure 3.9: All Euler orientation maps, (a) alloy B and (b) alloy B15 samples after hot rolling prior tensile testing; (c) alloy B and (d) alloy B15 samples after tensile testing at 300 °C.

3.4.3 Thermal stability of hot-rolled sheets and potential applications at high temperature

Table 3.5 presents a comparison of the elevated-temperature YSs and thermal stability of several commercial wrought aluminum alloys. The mechanical properties of most precipitation-strengthened Al alloys, such as 2xxx, 6xxx, and 7xxx alloys, deteriorate dramatically after thermal exposure at high temperatures, mainly because of rapid coarsening of the strengthening precipitates. The Al–Mg–Mn AA5083 alloys are potential candidates for high-temperature applications because its main strengthening mechanism (i.e., Mg solid-solution strengthening) is not prone to fade at high temperatures; the YS of conventional 5083 alloy at 315 °C is 52 MPa, which is much better than those of most precipitation-strengthened alloys [45]. More importantly, through the three-step heat treatment in the present work, a large number of thermally stable AlMn dispersoids were introduced into the

aluminum matrix of the base alloy (Fig. 3.2a), which reinforced not only the ambient-temperature strength, but also the high-temperature strength (Figs. 3.4 and 3.5). The elevated-temperature YS (300 °C) reached 88 MPa in the hot-rolled sheets, resulting in an improvement of 70% relative to that of conventional AA5083 alloy. In particular, the YSs at 25 and 300 °C remained stable after long-term thermal exposure for up to 500 h because of the superior thermal stability of the AlMn dispersoids (Fig. 3.7), making this hot-rolled alloy an excellent candidate as an engineering material for various elevated-temperature applications.

The present work focused on low-Sc alloys (Sc range of 0.08–0.15 wt.%) due to cost considerations. The AlMn dispersoids and Al_3(Sc,Zr) precipitates are both thermally stable at elevated temperatures, and could synergistically improve the alloy strength. In addition, the precipitation temperature ranges of AlMn dispersoids and Al_3(Sc,Zr) precipitates are similar and compatible (375–425 °C), which provides a common base for developing aluminum alloys with good high-temperature strength. However, this synergetic strengthening effect is limited to relatively low temperatures. At 20 - 200 °C, the addition of Sc and Zr significantly improves the tensile properties (Fig. 3.4). At higher temperatures (300–400 °C), the YSs of both Sc/Zr-containing alloys were lower than that of the base alloy (Fig. 3.6), restricting the application of Sc/Zr-containing alloys at high temperatures to some extent.

Table 3.5: Comparison of the YS at 300 ºC (MPa) of serval commercial wrought aluminum alloys

Alloys	YS at 300-315 ºC for various holding time					Reference
	0.5 h	10 h	100 h	500 h	1000 h	
2024-T6*	95	70	55	--	41	[45]
5083-O*	52	52	52		52	[45]
6061-T6*	75	55	31	--	29	[45]
7075-T6*	55	52	48	--	45	[45]
Alloy B (5083 base)	88	88	86	85	--	Present work
Alloy B08 (5083-0.08Sc)	66	66	67	69	--	Present work
Alloy B15 (5083-0.15Sc)	67	66	67	68	--	Present work

Note: * Test temperature and thermal exposure temperature was 315 ºC [45].

Owing to the poor rolling performance and the occurrence of alligator and crack defects during rolling [10], hot rolling was carried out at 500 °C in the present work, which caused extensive coarsening of the AlMn dispersoids and Al_3(Sc,Zr) precipitates (Fig. 3.3). If the rolling performance can be improved and the rolling temperature lowered to 400–425 °C to reduce the coarsening of both types of particles, a better synergetic strengthening effect of the two types of particles and, hence, higher strength at high temperatures can be expected.

3.5 Conclusions

The effects of Sc and Zr additions to Al–Mg–Mn AA5083 alloys, particularly in the low Sc and Zr range (0.08–0.15 wt.%), on the microstructure and ambient/elevated-temperature mechanical properties were investigated. The results are summarized as follows:

1. The grain size of the as-cast microstructure was moderately decreased by the addition of Sc and Zr, whereas the area fraction of Fe/Mn-rich intermetallics and primary Mg_2Si remarkably increased.
2. Two populations of strengthening particles (AlMn dispersoids and $Al_3(Sc,Zr)$ precipitates) precipitated in the Sc/Zr-containing alloys during the three-step heat treatment. However, the addition of Sc and Zr caused a reduction in AlMn dispersoids and an increase in dispersoid- free zones.
3. During hot rolling at 500 °C, both the AlMn dispersoids and $Al_3(Sc,Zr)$ precipitates coarsened. The number density of AlMn dispersoids decreased by 60–80% after hot rolling, while the number density of $Al_3(Sc,Zr)$ precipitates reduced by 71–76% compared to that in the heat-treated alloy (before rolling).
4. The tensile properties of the rolled sheets at 25–200 °C were significantly improved with increasing Sc and Zr content. The ambient-temperature YS and UTS of alloy B15 (with 0.16% Sc and 0.17% Zr) were 295 and 411 MPa, respectively, showing an improvement of 30% in YS and 11.8% in UTS compared to the base alloy. However, the YSs of the Sc/Zr-containing alloys at high temperatures (300–400 °C) were lower than those of the base alloy, most likely due to the grain boundary sliding mechanism.
5. The mechanical properties of the base and Sc/Zr-containing alloys were thermally stable during long-term thermal exposure at 300 °C for 500 h because of the superior thermal stability of the AlMn dispersoids and $Al_3(Sc,Zr)$ precipitates, providing great potential for various high-temperature applications.
6. Constitutive analysis was applied to predict the YS contributions of the different strengthening mechanisms at 25 and 300 °C. The predicted YSs at 25 °C were in

good agreement with the experimentally measured values. However, the predicted YSs at 300 °C of the Sc/Zr-containing alloys were quite different from the experimental ones. This discrepancy was predominantly due to the softening effect of grain boundary sliding, based on the EBSD results.

Acknowledgments

The authors would like to acknowledge the financial support from the Natural Sciences and Engineering Research Council of Canada (NSERC) and Rio Tinto Aluminum under the Grant No. CRDPJ 514651-17, through the Research Chair in Metallurgy of Aluminum Transformation at the University of Quebec at Chicoutimi.

3.6 References

[1] J.R. Davis, Aluminum and Aluminum Alloys, Light Metals and alloys (2001) 66-66.
[2] J.A.V.D. Hoeven, L. Zhuang, A New 5xxx Series Alloy Developed for Automotive Applications, SAE TECHNICAL PAPER SERIES (724) (2002) 1-8.
[3] E.L. Huskins, B. Cao, K.T. Ramesh, Strengthening mechanisms in an Al-Mg alloy, Materials Science and Engineering A 527(6) (2010) 1292-1298.
[4] Ø. Ryen, B. Holmedal, O. Nijs, E. Nes, E. Sjölander, H.-E. Ekström, Strengthening mechanisms in solid solution aluminum alloys, Metallurgical and Materials Transactions A 37(6) (2006) 1999-2006.
[5] Y. Li, A. Muggerud, A. Olsen, T. Furu, Precipitation of partially coherent α-Al (Mn, Fe) Si dispersoids and their strengthening effect in AA 3003 alloy, Acta Materialia 60(3) (2012) 1004-1014.
[6] Z. Li, Z. Zhang, X.-G. Chen, Microstructure, elevated-temperature mechanical properties and creep resistance of dispersoid-strengthened Al-Mn-Mg 3xxx alloys with varying Mg and Si contents, Materials Science and Engineering: A 708 (2017) 383-394.
[7] K. Liu, X.G. Chen, Development of Al-Mn-Mg 3004 alloy for applications at elevated temperature via dispersoid strengthening, Materials and Design 84 (2015) 340-350.
[8] A.M.F. Muggerud, E.A. Mørtsell, Y. Li, R. Holmestad, Dispersoid strengthening in AA3xxx alloys with varying Mn and Si content during annealing at low temperatures, Materials Science and Engineering: A 567 (2013) 21-28.
[9] K. Liu, H. Ma, X.G. Chen, Improving the elevated-temperature properties by two-step heat treatments in al-mn-mg 3004 alloys, Metallurgical and Materials Transactions B 49(4) (2018) 1588-1596.
[10] A.Y. Algendy, K. Liu, X.G. Chen, Evolution of dispersoids during multistep heat treatments and their effect on rolling performance in an Al-5 % Mg-0 . 8 % Mn alloy, Materials Characterization 181(September) (2021) 111487-111487.

[11] Z. Li, Z. Zhang, X.G. Chen, Improvement in the mechanical properties and creep resistance of Al-Mn-Mg 3004 alloy with Sc and Zr addition, Materials Science and Engineering A 729(December 2017) (2018) 196-207.
[12] E.A. Marquis, D.N. Seidman, Nanoscale structural evolution of Al 3 Sc precipitates in Al(Sc) alloys, Acta Materialia 49(11) (2001) 1909-1919.
[13] D.N. Seidman, E.A. Marquis, D.C. Dunand, Precipitation strengthening at ambient and elevated temperatures of heat-treatable Al (Sc) alloys, Acta Materialia 50(16) (2002) 4021-4035.
[14] P. Xu, F. Jiang, M. Tong, Z. Tang, J. Jiang, N. Yan, Y. Peng, Precipitation characteristics and morphological transitions of Al3Sc precipitates, Journal of Alloys and Compounds 790 (2019) 509-516.
[15] E.a. Marquis, D.N. Seidman, Coarsening Kinetics of Nanoscale Al-3Sc Precipitates in an Al-Mg-Sc Alloy, Acta Mater. 53 (2005) 4259-4268.
[16] P. Xu, F. Jiang, Z. Tang, N. Yan, J. Jiang, X. Xu, Y. Peng, Coarsening of Al3Sc precipitates in Al-Mg-Sc alloys, Journal of Alloys and Compounds 781 (2019) 209-215.
[17] C. Booth-Morrison, D.C. Dunand, D.N. Seidman, Coarsening resistance at 400 °c of precipitation-strengthened Al-Zr-Sc-Er alloys, Acta Materialia 59(18) (2011) 7029-7042.
[18] C.B. Fuller, J.L. Murray, D.N. Seidman, Temporal evolution of the nanostructure of Al(Sc ,Zr) alloys:Part I -Chemical compositions of Al3(Sc1-xZrx) precipitates, Acta Materialia 53 (2005) 5401-5413.
[19] C.B. Fuller, D.N. Seidman, D.C. Dunand, Mechanical properties of Al (Sc, Zr) alloys at ambient and elevated temperatures, Acta materialia 51(16) (2003) 4803-4814.
[20] J. Lai, Z. Zhang, X.G. Chen, The thermal stability of mechanical properties of Al-B 4C composites alloyed with Sc and Zr at elevated temperatures, Materials Science and Engineering A 532 (2012) 462-470.
[21] P. Cavaliere, M. Cabibbo, Effect of Sc and Zr additions on the microstructure and fatigue properties of AA6106 produced by equal-channel-angular-pressing, Materials Characterization 59(3) (2008) 197-203.
[22] T. Dorin, M. Ramajayam, J. Lamb, T. Langan, Effect of Sc and Zr additions on the microstructure/strength of Al-Cu binary alloys, Materials Science and Engineering A 707(July) (2017) 58-64.
[23] G. Li, N. Zhao, T. Liu, J. Li, C. He, C. Shi, E. Liu, J. Sha, Effect of Sc/Zr ratio on the microstructure and mechanical properties of new type of Al-Zn-Mg-Sc-Zr alloys, Materials Science and Engineering A 617 (2014) 219-227.
[24] G.B. Teng, C.Y. Liu, Z.Y. Ma, W.B. Zhou, L.L. Wei, Y. Chen, J. Li, Y.F. Mo, Effects of minor Sc addition on the microstructure and mechanical properties of 7055 Al alloy during aging, Materials Science and Engineering A 713 (2018) 61-66.
[25] C. Xu, W. Xiao, R. Zheng, S. Hanada, H. Yamagata, C. Ma, The synergic effects of Sc and Zr on the microstructure and mechanical properties of Al–Si–Mg alloy, Materials & Design 88 (2015) 485-492.
[26] M. Li, Q. Pan, Y. Shi, X. Sun, H. Xiang, High strain rate superplasticity in an Al–Mg–Sc–Zr alloy processed via simple rolling, Materials Science and Engineering A 687(January) (2017) 298-305.
[27] F. Liu, Z. Ma, Achieving exceptionally high superplasticity at high strain rates in a micrograined Al–Mg–Sc alloy produced by friction stir processing, Scripta Materialia 59(8) (2008) 882-885.

[28] Y. Luo, Q. Pan, Y. Sun, S. Liu, Y. Sun, L. Long, X. Li, X. Wang, M. Li, Hardening behavior of Al-0.25 Sc and Al-0.25 Sc-0.12 Zr alloys during isothermal annealing, Journal of Alloys and Compounds 818 (2020) 152922.
[29] D. Pan, S. Zhou, Z. Zhang, M. Li, Y. Wu, Effects of Sc(Zr) on the microstructure and mechanical properties of as-cast Al–Mg alloys, Materials Science and Technology (United Kingdom) 33(6) (2017) 751-757.
[30] S.a. Zhou, Z. Zhang, M. Li, D. Pan, H. Su, X. Du, P. Li, Y. Wu, Effect of Sc on microstructure and mechanical properties of as-cast Al-Mg alloys, Materials and Design 90 (2016) 1077-1084.
[31] L.L. Rokhlin, N.R. Bochvar, I.E. Tarytina, N.P. Leonova, Phase composition and recrystallization of Al-based Al-Sc-Mn-Zr alloys, Russian Metallurgy (Metally) 2010(3) (2010) 241-247.
[32] E.M. Elgallad, K. Liu, Z. Zhang, X.G. Chen, Effect of transition elements on dispersoid formation and elevated-temperature mechanical properties in 6082 aluminum alloy, Philosophical Magazine 101(1) (2021) 96-116.
[33] K. Liu, E. Elgallad, C. Li, X.G. Chen, Effects of Zr and Sc additions on precipitation of α-Al(FeMn)Si dispersoids under various heat treatments in Al-Mg-Si AA6082 alloys, International Journal of Materials Research 112(9) (2021) 706-716.
[34] E.A. Marquis, D.N. Seidman, M. Asta, C. Woodward, Composition evolution of nanoscale Al3Sc precipitates in an Al-Mg-Sc alloy: Experiments and computations, Acta Materialia 54(1) (2006) 119-130.
[35] Z. Li, Z. Zhang, X.G. Chen, Effect of Metastable Mg2Si and Dislocations on α-Al(MnFe)Si Dispersoid Formation in Al-Mn-Mg 3xxx Alloys, Metallurgical and Materials Transactions A: Physical Metallurgy and Materials Science 49(11) (2018) 5799-5814.
[36] M.J. Starink, N. Gao, N. Kamp, S.C. Wang, P.D. Pitcher, I. Sinclair, Relations between microstructure, precipitation, age-formability and damage tolerance of Al-Cu-Mg-Li (Mn, Zr, Sc) alloys for age forming, Materials Science and Engineering A 418(1-2) (2006) 241-249.
[37] W. Lefebvre, F. Danoix, H. Hallem, B. Forbord, A. Bostel, K. Marthinsen, Precipitation kinetic of Al3(Sc, Zr) dispersoids in aluminium, Journal of Alloys and Compounds 470 (2009) 107-110.
[38] M. Cabibbo, E. Evangelista, M. Vedani, Influence of severe plastic deformations on secondary phase precipitation in a 6082 Al-Mg-Si alloy, Metallurgical and Materials Transactions A 36(5) (2005) 1353-1364.
[39] I. Lomaev, E. Elsukov, On the analysis of the mechanisms of the strain-induced dissolution of phases in metals, PHYSICS OF METALS AND METALLOGRAPHY C/C OF FIZIKA METALLOV I METALLOVEDENIE 102(2) (2006) 186.
[40] J. Rakhmonov, K. Liu, P. Rometsch, N. Parson, X.G. Chen, Effects of Al(MnFe)Si dispersoids with different sizes and number densities on microstructure and ambient/elevated-temperature mechanical properties of extruded Al–Mg–Si AA6082 alloys with varying Mn content, Journal of Alloys and Compounds 861 (2021) 157937-157937.
[41] P. Summers, Y. Chen, C. Rippe, B. Allen, A. Mouritz, S. Case, B. Lattimer, Overview of aluminum alloy mechanical properties during and after fires, Fire Sci, Rev., no. December 2016 (2015).
[42] K.L. Kendig, D.B. Miracle, Strengthening mechanisms of an Al-Mg-Sc-Zr alloy, Acta Materialia 50(16) (2002) 4165-4175.

[43] L. Tang, X. Peng, J. Huang, A. Ma, Y. Deng, G. Xu, Microstructure and mechanical properties of severely deformed Al-Mg-Sc-Zr alloy and their evolution during annealing, Materials Science and Engineering: A 754 (2019) 295-308.
[44] J. Qin, Z. Zhang, X.G. Chen, Mechanical Properties and Strengthening Mechanisms of Al-15 Pct B4C Composites with Sc and Zr at Elevated Temperatures, Metallurgical and Materials Transactions A: Physical Metallurgy and Materials Science 47(9) (2016) 4694-4708.
[45] J.G. Kaufman, Properties of aluminum alloys: tensile, creep, and fatigue data at high and low temperatures, ASM international1999.
[46] A.J. Ardell, Precipitation hardening, Metallurgical Transactions A 16(12) (1985) 2131-2165.
[47] A.H. Chokshi, Grain boundary processes in strengthening, weakening, and superplasticity, Advanced Engineering Materials 22(1) (2020) 1900748.
[48] X. Zhang, H. Wang, B. Yan, C. Zou, Z. Wei, The effect of grain refinement and precipitation strengthening induced by Sc or Er alloying on the mechanical properties of cast Al-Li-Cu-Mg alloys at elevated temperatures, Materials Science and Engineering: A 822 (2021) 141641.
[49] F. Musin, D.R. Lesuer, T.G. Nieh, Superplastic behavior of an Al - Mg alloy at elevated temperatures, Material Sciencr & Engineering A 342 (2003) 169-177.
[50] A. Venkataraman, M. Linne, S. Daly, M.D. Sangid, Criteria for the prevalence of grain boundary sliding as a deformation mechanism, Materialia 8 (2019) 100499.
[51] S. Griffiths, J.R. Croteau, M.D. Rossell, R. Erni, A. De Luca, N.Q. Vo, D.C. Dunand, C. Leinenbach, Coarsening- and creep resistance of precipitation-strengthened Al–Mg–Zr alloys processed by selective laser melting, Acta Materialia 188 (2020) 192-202.

Chapter 4: On the Evolution of Discontinuous/Continuous $Al_3(Sc, Zr)$ precipitates during the thermal process in Al-Mg-Mn 5083 alloy with higher Sc addition

Ahmed Y. Algendy [1], Kun Liu [1,], Paul Rometsch [2], Nick Parson [2], X.-Grant Chen [1,]
[1] Department of Applied Science, University of Quebec at Chicoutimi, Saguenay (QC), G7H 2B1, Canada
[2] Arvida Research and Development Center, Rio Tinto Aluminum, Saguenay (QC), G7S 4K8, Canada

This article has been published in:
Material Characterization 192 (2022) 112241

Abstract

The evolution of discontinuous and continuous $Al_3(Sc,Zr)$ precipitation in an Al-Mg-Mn AA5083 alloy during heat treatment and hot rolling was investigated. The results showed that, at a high Sc content (0.43 wt.%), a large number of line/fan-shaped structures were formed as discontinuous $Al_3(Sc,Zr)$ precipitation during solidification, while no such discontinuous precipitation was observed when the amount of Sc added was low (0.16 wt.%). During the three-step heat treatment (275 °C /12 h + 375 °C/48 h + 425 °C/12 h), two types of precipitates — Mn-bearing dispersoids and spherical $Al_3(Sc,Zr)$ precipitates — were formed as the main strengthening phases. In the high-Sc alloy, the discontinuous $Al_3(Sc,Zr)$ precipitates dissolved partially. However, the quantity of the spherical $Al_3(Sc,Zr)$ precipitates in the high-Sc alloy was much lower than that in the low-Sc alloy, lowering its age hardening response. During hot rolling, although the discontinuous precipitates were completely dissolved, the number density of the spherical $Al_3(Sc,Zr)$ precipitates in the high-Sc alloy was still lower than that in the low-Sc alloy. The tensile properties of the Sc-containing alloys improved significantly compared with those of the base alloy. However, the yield and

ultimate tensile strengths of the high-Sc alloy were lower than those of the low-Sc alloy. This indicates that the discontinuous precipitation had a deleterious effect on the mechanical properties of the alloy.

Keywords: Al-Mg-Mn 5083 alloy, Discontinuous precipitation, $Al_3(Sc,Zr)$ precipitates, Sc and Zr, Microstructure, Mechanical properties.

4.1 Introduction

Microalloying of rare-earth elements, especially Sc, is an efficient approach to improving the mechanical properties of aluminum and its alloys [1-3]. Microalloying with Sc can significantly improve the mechanical properties, preserve the work hardening and enhance the recrystallization resistance of Al-Mg-Mn 5xxx alloys [4-6]. In Sc-containing alloys, a high number of fine and coherent $L1_2$-Al_3Sc particles can be precipitated in the aluminum matrix as the strengthening phase through the decomposition of the supersaturated solid solution during aging treatment at relatively high temperatures [4, 7-10]. Owing to its cost-effectiveness, Zr is often added together with Sc. Zr can substitute Sc in Al_3Sc and form core-shell $Al_3(Sc_{1-x},Zr_x)$ precipitates with the same $L1_2$-crystal structure while improved coarsening resistance [11, 12].

In Al-Sc/Al-Sc-Zr systems, $Al_3Sc/Al_3(Sc, Zr)$ precipitates are formed continuously and discontinuously [13-16]. Continuous precipitation usually occurs during aging treatment (300–425 °C). Nano-sized $Al_3Sc/Al_3(Sc,Zr)$ precipitates effectively retard the dislocation and grain boundary movements and significantly improve the alloy properties [4, 8, 9, 11]. However, discontinuous precipitation can also occur during solidification or aging treatment [16-19]. The tendency of Al-Sc alloys to form Al_3Sc discontinuous precipitates is strongly related to their Sc level (often in high-Sc hypereutectic alloys) [14, 16, 20, 21], solidification

rate [14, 17, 18, 22], and annealing temperature [14, 19]. Norman *et al.* [20] reported that the discontinuous precipitation reaction of rod-like precipitates occurs during solidification cooling to room temperature in a hypereutectic 0.79 wt.% Sc alloy. According to Black and Hopkins [21], discontinuous Al_3Sc precipitates with various morphologies, including rod- and branch-like morphologies, can be formed during the solidification of Al-1.0 wt.% Sc. Furthermore, the effect of the cooling rate during solidification on the Al_3Sc discontinuous precipitation of Al-Sc alloys has been investigated [17, 22]. The results reported the formation of rod- and lamellae-shaped Al_3(Sc,Zr) precipitates at slow cooling rates and a decrease in the number density of these precipitates with the increasing cooling rate. Lathabai *et al.* [18] reported that discontinuous precipitation in the as-cast microstructure of Al-4.5%Mg-0.7Mn alloy occurs within a low range of 0.17–0.26 wt.% Sc. Similar discontinuous precipitation phenomena have been observed in other alloy systems containing transition metals, such as Al-Zr [23] and Al-Li [24].

Most studies related to the effect of discontinuous precipitation on the mechanical properties of Al-Sc/Al-Sc-Zr systems considered Al_3Sc discontinuous precipitates as an undesirable microstructure, which negatively affects the mechanical properties of the alloy. Zhang *et al*. [19] reported the deterioration effect of discontinuous precipitates on the microhardness of heat-treated Al-0.7 wt.% Sc. Lohar *et al.* [22] observed that the as-cast Al_3(Sc,Zr) discontinuous precipitates in an Al-0.3Sc-0.15Zr alloy lowered its microhardness during aging. However, Lathabai et al. [18] found that the microhardness and tensile properties of an Al-4.5%Mg-0.7Mn alloy with 0.17% Sc addition increased compared to those of the Sc-free counterpart despite the occurrence of discontinuous precipitation.

To date, studies on the effect of discontinuous precipitation on the mechanical properties of Al-Mg-Mn alloys have been scarce, and most of them focused on the microstructural evolution of Al_3(Sc,Zr) discontinuous precipitates. This study investigated the precipitation behaviors of discontinuous and continuous precipitates in a typical Al-Mg-Mn 5083 alloy with various Sc levels during the thermomechanical process (heat treatment and hot rolling). The effect of discontinuous precipitation on the aging response and tensile properties of the hot-rolled sheets was also studied.

4.2 Experimental procedure

Three Al-Mg-Mn alloys were prepared according to the typical AA5083 chemical composition. The chemical compositions of experimental alloys analyzed with optical omission spectrometer are listed in Table 4.1. In addition to the base alloy, the alloy L-Sc contained 0.16% Sc and 0.17% Zr, and the alloy H-Sc had 0.43% Sc and 0.15% Zr (all the alloy compositions used in this study were in wt.%). The alloys were batched in a graphite crucible using an electric resistance furnace at 780 ^{o}C. After melting and degassing, the melt was poured into a permanent steel mold preheated at 250 ^{o}C, which had a cooling rate of ~2 °C/s during solidification. The dimensions of the cast ingots were 30 × 40 × 80 mm.

A three-step heat treatment (275^{o}C/12h + 375^{o}C/48h + 425^{o}C/12h) was applied to all cast ingots to promote the effective precipitation of Mn-bearing dispersoids and Al_3(Sc,Zr) precipitates in the aluminum matrix [25]. The heat treatment was conducted in a programmable electric air circulating furnace with a 60 ^{o}C/h heat rate. The thickness of the heat-treated ingots was machined to 26.5 mm, and then preheated at 500 °C for 1.5 h prior hot rolling. The ingots were hot-rolled in multiple passes at a temperature of 500±10 °C. The thickness reduction of each pass is approximately 3.2 mm. The rolled plate was back to the

furnace and heated at 500 °C for 20 min after each 3 passes to keep rolling at similar temperature. The final thickness of sheet is ~3.2 mm, which is ~ 88% reduction. Prior mechanical testing, all rolled sheets were annealed at 300 °C for 5 h to relieve the rolling-induced thermal stress.

Table 4.1: Chemical composition of experimental alloys (wt.%)

Alloys	**Mg**	**Mn**	**Si**	**Fe**	**Cu**	**Cr**	**Ti**	**Sc**	**Zr**
Base	4.78	0.79	0.26	0.31	0.12	0.14	0.09	---	---
L-Sc	4.75	0.80	0.30	0.31	0.11	0.15	0.09	**0.16**	**0.17**
H-Sc	4.76	0.75	0.30	0.33	0.10	0.15	0.10	**0.43**	**0.15**

The precipitation behavior of precipitates during heat treatment was evaluated by electrical conductivity (EC) and microhardness (HV) measurements. EC was deterimined using a sigmascope SMP 10 electrical conductivity device with a %IACS unit at room temperature. Vickers microhardness was obtained using NG-1000 CCD microhardness machine with 25 g load for 20 s dwelling time. Generally, 20 measurements were performed to evaluate the average hardness value for each sample. The tensile samples were machined according to ASTM E8/E8M-16a in the rolling direction with a gauge size of 3 x 6 mm. Uniaxial tensile tests were conducted using Instron 8801 servo-hydraulic testing unit at strain rate 0.001 s^{-1}. Average results were obtained from three repeated tests. The samples were ground and polished using a standard metallographic procedure for microstructure observations. The microstructure of studied alloys was charaterized using optical microscopy (Nikon, Eclipse ME600), scanning electron microscope (SEM, JSM-6480LV) and transmission electron microscope (TEM, JEM-2100). The as-cast, heat-treated and hot-rolled ssamples were observed after etching by 0.5% HF for 30 s. TEM was used to observe the

distribution of Mn-bearing dispersoids and Al_3(Sc,Zr) precipitates. All TEM images were taken along the $[001]_{Al}$ zone axis. Centered superlattice dark-field micrograph was recorded along [100] reflections close to <011> direction to reveal Al_3(Sc, Zr) precipitates. The size and number density of precipitates were measured using ImageJ image analysis software with TEM images. The quantitative analysis was performed on 10 images, and each image contains more than 300 particles. The number density of precipitates was determined using the following equation:

$$ND = \frac{N}{A*(D+t)} \qquad (1)$$

Where; N is the number of particles in the TEM image, A is the total area, D is the equivalent diameter, and t is the thickness of the TEM foil, which was measured using the convergent electron beam diffraction (CBED) method [26].

4.3 Results and discussion

4.3.1 As-cast microstructure

Fig. 4.1 shows the as-cast microstructure of the experimental alloys under the optical bright and dark-field modes after etching with Keller's reagent. The as-cast microstructure mainly consisted of α-Al dendrite cells as the matrix, with several intermetallic phases distributed along the dendrite boundaries. The major intermetallic compounds (IMCs) in the three alloys were Fe/Mn-rich α-Al_{15}(Fe,Mn,Cr)$_3Si_2$ and Al_6(Fe,Mn,Cr) intermetallics and primary Mg_2Si intermetallics, as indicated by the SEM-EDS results. In the Sc-containing alloys (low-Sc (L-Sc) and high-Sc (H-Sc)), a few primary Al_3(Sc,Zr) particles with cubic

morphology were detected within the aluminum dendrite cells (see the inserts in Figs. 1b and 1c).

A noticeable difference was observed in the microstructure of the as-cast alloy after the addition of high Sc (0.43 %). In the aluminum dendrite cells, many areas showed the formation of a line-or fan-shaped structure (Fig. 4.1c and d). This type of precipitation was not easily observed using optical microscopy when the sample was just polished. After etching the H-Sc alloy in the dark-field mode, both line- and fan-shaped Sc-containing particles could be observed (Fig. 4.1d), which initiated at the dendrite boundaries and extended into the cell interiors. This discontinuous precipitation of Sc-containing particles was related to the decomposition of the saturated solid solution in the aluminum matrix to form Al_3(Sc,Zr) at a moving grain boundary with a common lamellar structure [21, 27]. In the L-Sc alloy, such discontinuous precipitation rarely occurred.

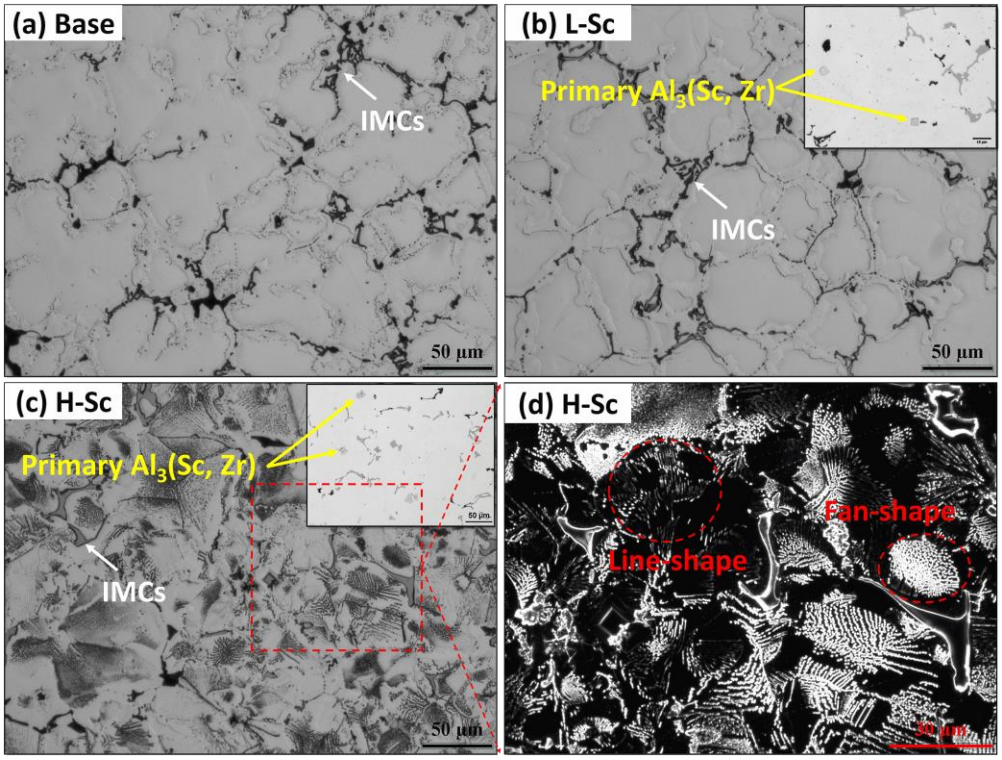

Figure 4.1: Optical microscopy images of the as-cast microstructure in the bright-field mode after etching with Keller's agent (a) base, (b) L-Sc, and (c) H-Sc alloys. (d) high-magnification dark-field image of the H-Sc alloy showing line/fan-shaped discontinuous precipitation at the dendrite cells. Inserted image in Fig. 1b and c shows the primary $Al_3(Sc,Zr)$.

The discontinuous precipitation in the H-Sc alloy was investigated in detail using TEM, and the results are shown in Fig. 4.2. The observations were conducted along the $[001]_{Al}$ and $[011]_{Al}$ zone axes. The dark-field TEM images Fig. 4.2a and b showed lamellar aggregations near the cell/grain boundaries, which contained a high density of branched and rod-like precipitates. The corresponding selected area diffraction patterns (SADP) along the $[001]_{Al}$ zone axis showed light spots corresponding to the precipitates between the bright α-Al spots (Figs. 4.2c and 4.2i). This observation along with the TEM-EDS results (Fig. 4.2f) confirmed that these precipitates were $L1_2$-$Al_3Sc/Al_3(Sc,Zr)$ [16, 17]. In addition, the orientation relationship between α-Al and the precipitates was observed to be [100]α-Al//[100] precipitates.

Fig. 4.2d and e indicate that the discontinuous precipitation resulted from the multiplication of rod-like precipitates originating at the dendrite cell/grain boundaries, which extended into the dendritic cells. Many rod-like precipitates were aligned in sequence and gave a line-shaped appearance, as indicated by the optical microscopy images (Fig. 4.1d). This is consistent with the results reported in the literature [16, 23, 28]. In addition, In addition, a coarse, spherical $L1_2$-precipitate with a size of 20–30 nm was observed on one end of each rod-like precipitate (yellow circles in Fig. 4.2e), suggesting that the discontinuous precipitates could nucleate heterogeneously on the pre-existing particles. Mochugovskiy *et al.* [29] found that a line of coarse $L1_2$-dispersoids was formed heterogeneously on the grain boundaries before the onset of discontinuous precipitation. The

rod-like precipitates were of different sizes with a length ranging from 500 to 860 nm (Fig. 4.2 d and e). Furthermore, the TEM observations (Fig. 4.2g and h) along the $[011]_{Al}$ zone axes confirmed that the rod-like precipitates were aligned in a line sequence.

The formation of discontinuous $Al_3Sc/Al_3(Sc,Zr)$ precipitates during solidification with line- and fan-shaped aggregates has been reported in previous studies [27, 29-32]. Since the casting and solidification conditions of the two Sc-containing alloys were the same, the primary reason for the formation of discontinuous precipitates in the H-Sc alloy was its high Sc level. Hornbogen [30] reported that discontinuous precipitates tend to nucleate heterogeneously along the grain boundaries rather than within the grain interior. During solidification, Sc tends to segregate toward the dendrite boundaries, which are considered fast channels for the redistribution and transportation of solute atoms, enhancing the growth of discontinuous precipitates. Marquis *et al.* [31] reported that the dislocation lines and networks formed owing to internal stress relaxation can also act as heterogeneous nucleation sites for discontinuous Al_3Sc precipitation.

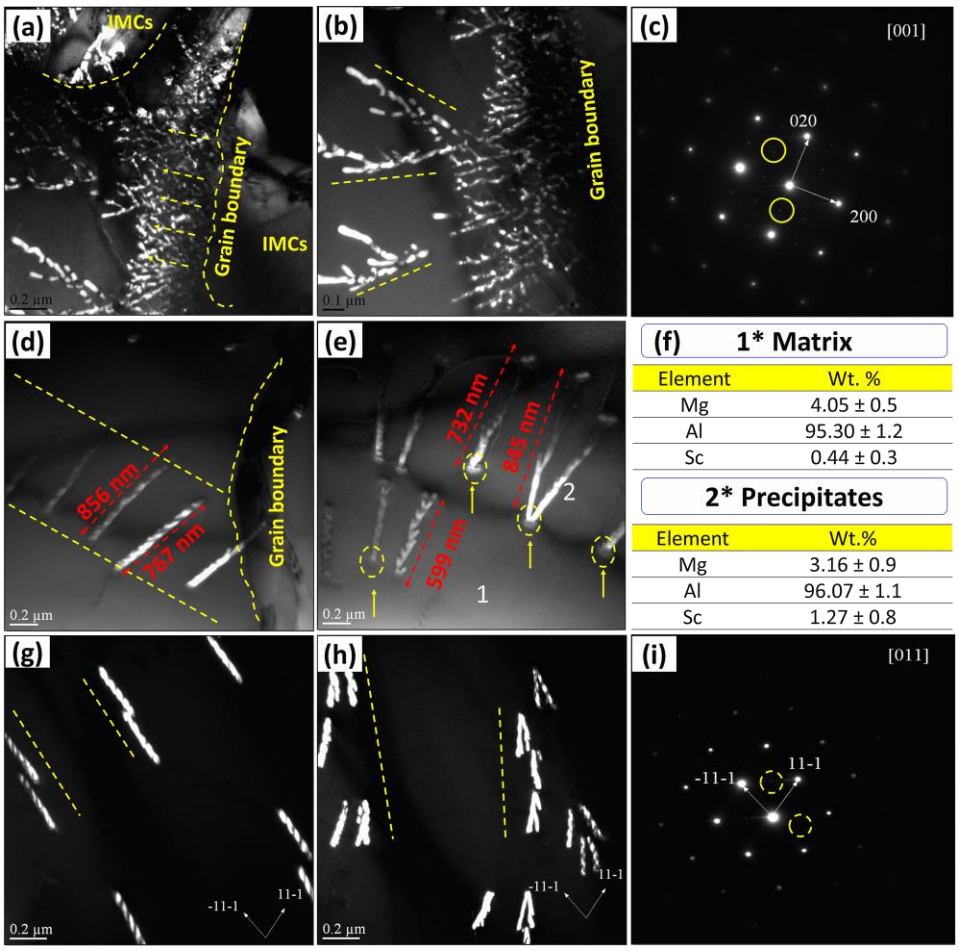

Figure 4.2: Dark-field TEM images showing the discontinuous precipitation of the H-Sc alloy under the as-cast condition along the (a and b) $[001]_{Al}$, (d and e) $[001]_{Al}$, and (g and h) $[011]_{Al}$ zone axes; (c and i) the corresponding SADPs confirming the $L1_2$-$Al_3Sc/Al_3(Sc,Zr)$ crystal structure of the precipitates; (f) TEM-EDS analysis results showing the chemistry of the matrix and rod-like precipitates..

4.3.2 Microstructure after heat treatment

Owing to the high Mn content in all the three experimental alloys, Mn-bearing dispersoids precipitated in the aluminum matrix after the three-step heat treatment [25]. The optical microscopy images of the three alloys (Fig. 4.3a–4.3c) revealed the presence of a precipitation zone (gray zone marked by the red line) and a precipitate-free zone (PFZ) (bright zone marked by the blue line) in the interdendritic region. The SEM images showed that a large number of Mn-bearing dispersoids existed in the base and L-Sc alloys (Fig. 4.3d),

whereas the line/fan-shaped structure remained in the H-Sc alloy along with several Mn-bearing dispersoids (Fig. 4.3e). However, as compared to the as-cast microstructure of the H-Sc alloy (Fig. 4.1c), the number of line/fan-shaped structures reduced remarkably after the heat treatment process, which indicates that the discontinuous precipitates dissolved partially during the heat treatment process [13, 16].

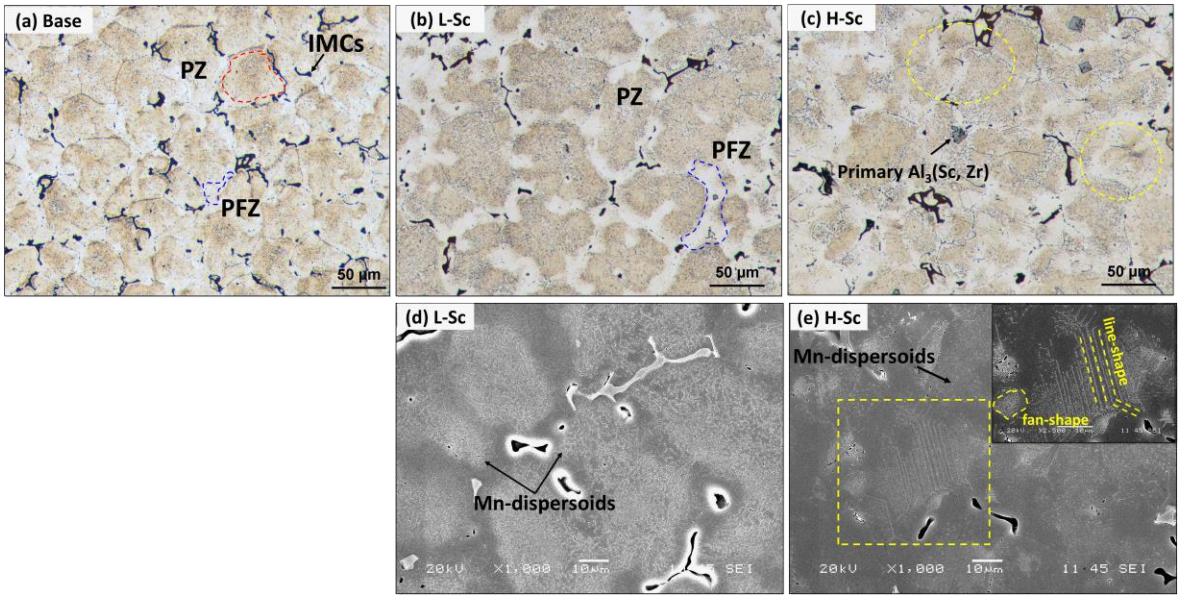

Figure 4.3: Microstructures of the alloys after the heat treatment showing the distribution of the precipitation zone and precipitate free zone, (a) base alloy, (b) L-Sc and (c) H-Sc alloys. SEM images showing the precipitation of Mn-bearing dispersoids in (d) L-Sc and (e) H-Sc co-existing with the line/fan-shaped structure.

The TEM images provided more details on the precipitation of both the Mn-bearing dispersoids and nano-sized $Al_3(Sc,Zr)$ precipitates during the heat treatment. In the L-Sc alloy, in addition to the Mn-bearing dispersoids (Fig. 4.4a), a large number of spherical and nano-sized $Al_3(Sc,Zr)$ precipitates were formed in the aluminum matrix (as continuous precipitation (CP)) (Fig. 4.4b). These precipitates overlapped with the Mn-bearing dispersoids (Fig. 4.4b). In the H-Sc alloy, a large number of discontinuous rod-like $Al_3(Sc,Zr)$ precipitates (DCP) were widely existed after the precipitation of the Mn-bearing

dispersoids and spherical $Al_3(Sc,Zr)$ precipitates. It should be mentioned that the Mn-bearing dispersoids formed in the matrix were Al_4Mn and Al_6Mn disperoids, identified by the selected area diffraction pattern and TEM-EDS analysis (not showing here) [25]. Figs. 4.4c–4.4f show two examples of discontinuous rod-like precipitates formed at different locations. The rod-like precipitates were non-uniformly distributed in the aluminum matrix and were much larger than the spherical ones (Fig. 4.4g). After heat treatment, the size of the rod-like precipitates decreased, and the length ranged from 200 to 350 nm. This indicates that these precipitates dissolved partially in the Al matrix during the heat treatment [16, 33, 34].

Moreover, in the vicinity of the rod-like precipitates, there were almost no spherical and fine $Al_3(Sc,Zr)$ precipitates (indicated by the blue line area), as shown in Fig. 4.4f. In addition, although the Sc content of the H-Sc alloy was high, it consisted of fewer spherical $Al_3(Sc,Zr)$ precipitates (Fig. 4.4f) than the L-Sc alloy (Fig. 4.4b). For instance, the number density of the spherical $Al_3(Sc,Zr)$ precipitates in the H-Sc alloy was 5188 μm^{-3}, while that in the L-Sc alloy was 19700 μm^{-3}. It is evident that the discontinuous precipitates consumed large amounts of Sc and Zr solutes and caused a large decrease in the Sc content in the solid solution, reducing the number density of the spherical $Al_3(Sc,Zr)$ precipitates formed during the subsequent heat treatment process. In addition, it created a depletion area around the rod-like precipitates, making the further precipitation of the spherical $Al_3(Sc,Zr)$ precipitates impossible.

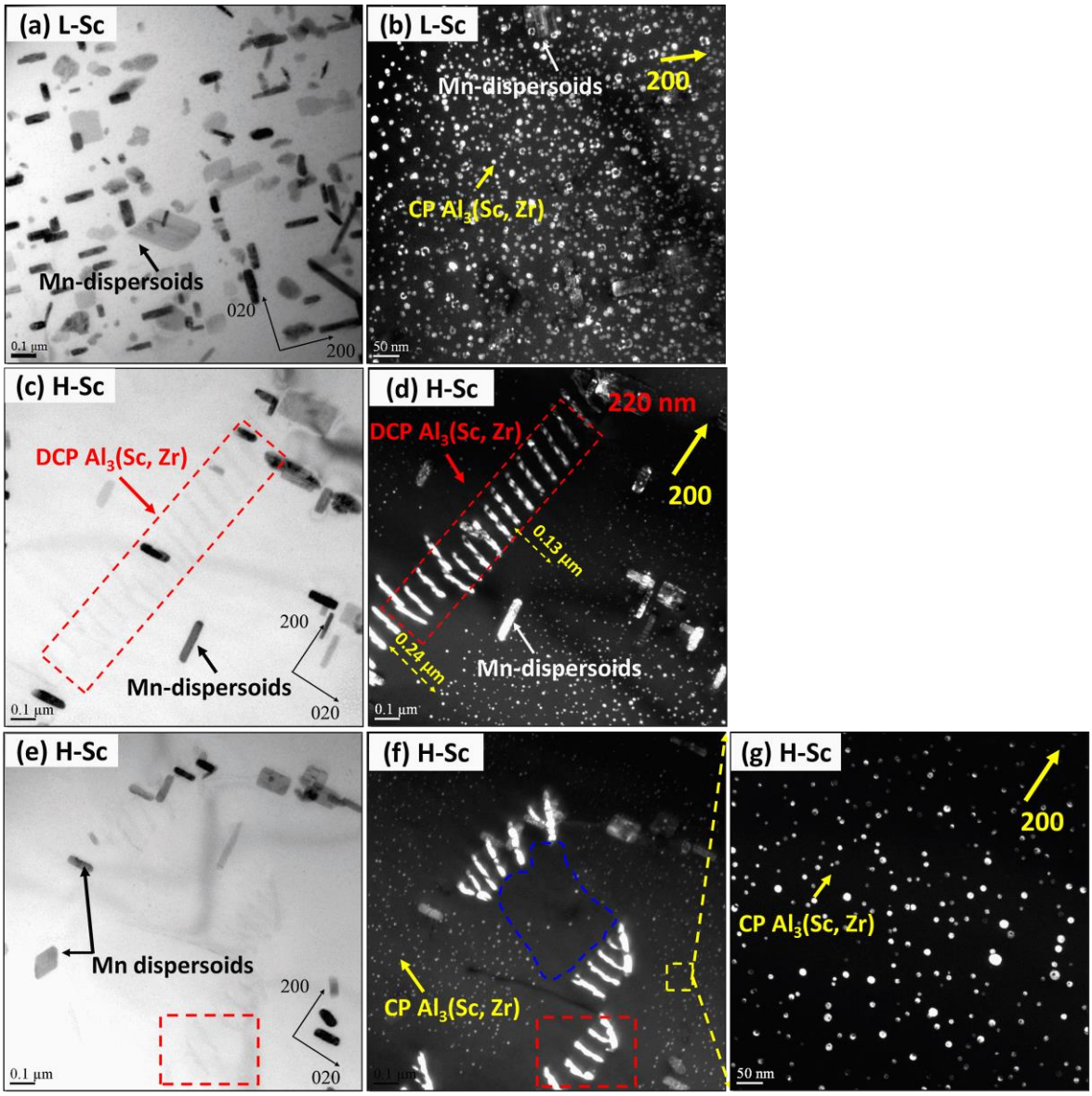

Figure 4.4: Bright-field (a, c, e) and dark-field (b, d, f, g) TEM images along the $[001]_{Al}$ zone axis showing the precipitation of Mn-bearing dispersoids, continuous and discontinuous $Al_3(Sc,Zr)$ precipitates in Sc-containing alloys under the heat-treated condition, (a, b) L-Sc and (c–g) H-Sc alloys.

Fig. 4.5 shows the electrical conductivity and microhardness of the alloys after the heat treatment. Owing to the increased amount of total precipitates (Mn-bearing dispersoids and $Al_3(Sc,Zr)$ precipitates), the electrical conductivity values of the Sc-containing alloys (L-Sc and H-Sc) were slightly lower than those of the base alloy. However, the microhardness

values of the Sc-containing alloys were considerably higher than that of the base alloy, which indicates that the nano-sized $Al_3(Sc,Zr)$ precipitates provided a substantial strengthening effect to the alloy. For instance, the microhardness increased from 112 HV for the base alloy to 136.4 HV for the L-Sc alloy. This is because a large number of fine $Al_3(Sc,Zr)$ precipitates coexisted with Mn-bearing dispersoids in the L-Sc alloy. However, the microhardness of the H-Sc alloy was lower (122 HV) than that of the L-Sc alloy (136.4 HV). This indicates that the discontinuous precipitates had a deleterious effect on the precipitation of fine $Al_3(Sc,Zr)$ precipitates, and hence on the hardening response of the alloy.

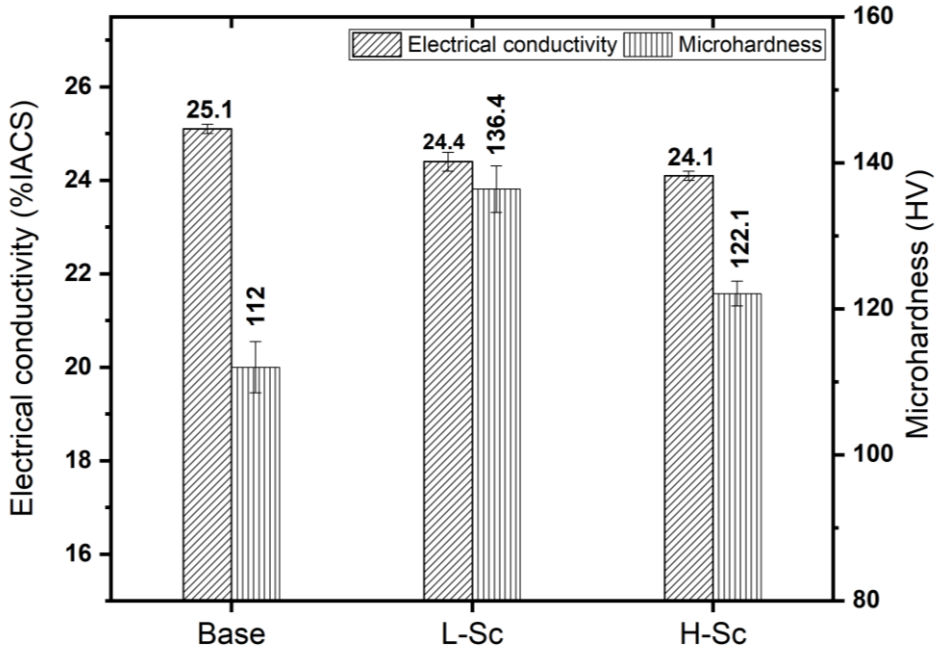

Figure 4.5: Electrical conductivity and microhardness of experimental alloys after heat treatment

4.3.3 Microstructure evolution during hot rolling

Prior to rolling, the heat-treated ingots were preheated at 500 °C for 1.5 h to improve their rollability. Fig. 4.6 shows the microstructure of the preheated sample of the H-Sc alloy. As shown in the figure, some areas with a line-shaped structure (Fig. 4.6a, marked with yellow

circles and Fig. 4.6b, marked with yellow dashed lines), similar to that observed in the heat-treated sample (Fig. 4.3), were present in the microstructure. However, these areas were much smaller than those in the heat-treated sample. In addition, the fan-shaped structure almost disappeared (Fig. 4.6b).

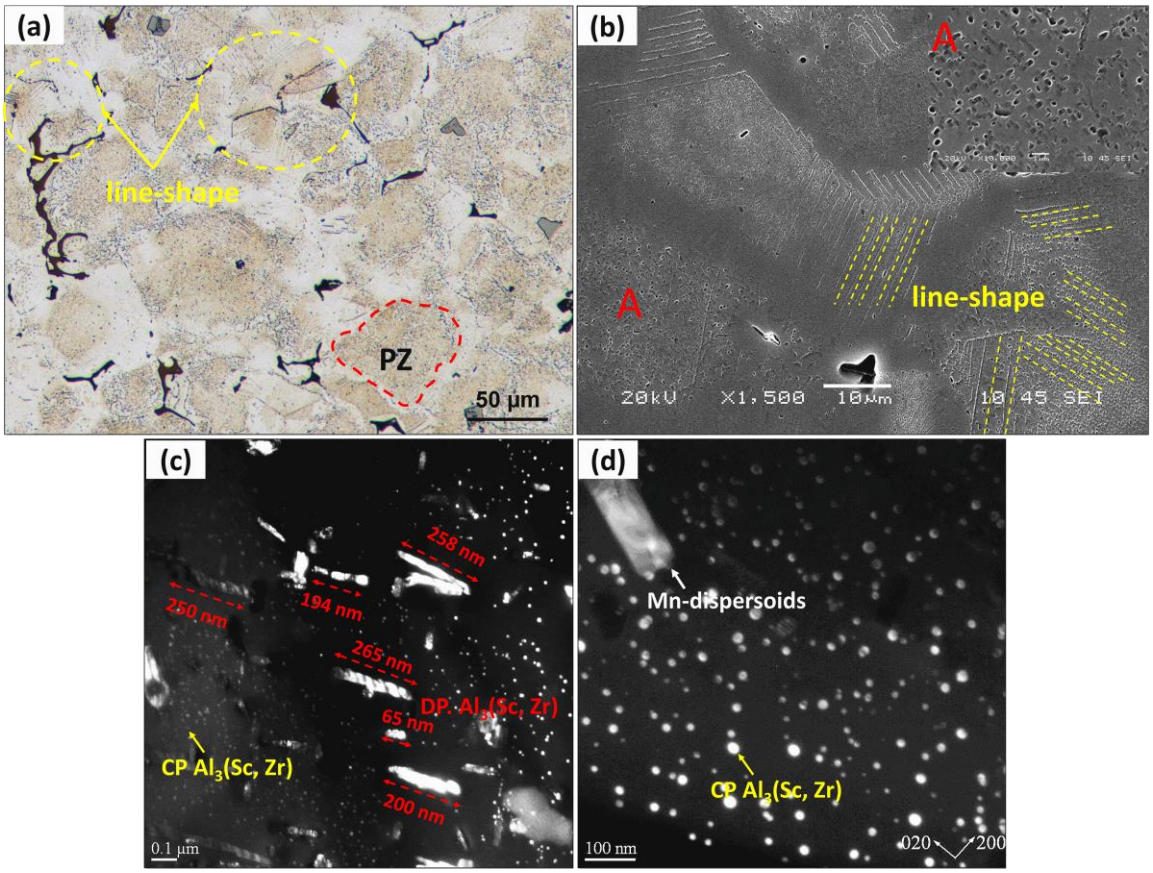

Figure 4.6: Microstructure of the preheated H-Sc sample (500℃/1.5h), (a) optical microscopy image and (b) SEM image showing the distribution of the line-shaped structure, and (c, d) dark-field TEM images showing the rod-like discontinuous precipitates and spherical $Al_3(Sc,Zr)$ precipitates.

The dark-field TEM image (Fig. 4.6c) showed the co-existence of rod-like discontinuous precipitates with spherical $Al_3(Sc,Zr)$ precipitates and Mn-bearing dispersoids. As compared to the case of the heat-treated sample (Fig. 4.4c), in the preheated sample, the size of the rod-like precipitates decreased, and the length ranged from 100 to 250 nm, indicating the further dissolution of the rod-like precipitates during the preheating process at 500 °C. This

phenomenon can be explained by the increase in the diffusivity of Sc with increasing temperature [35] and grain boundary stability [36]. Marquis *et al.* [31] reported that rod-like precipitates re-dissolve into the Al matrix during annealing. Sun *et al.* [16] reported the reduction in and disappearance of rod-like precipitates with increasing aging time up to 24 h at 340 °C. In contrast, the spherical Al_3(Sc,Zr) precipitates (Fig. 4.6d) grew moderately, and their size increased during the preheating process at 500 °C [37, 38].

Fig. 4.7 shows the typical microstructures of the hot-rolled Sc-containing alloys (L-Sc and H-Sc). Both the samples showed elongated grains parallel to the rolling direction (Figs. 4.7a and 4.7d), marked by red lines). Moreover, as shown in Fig. 4.7d, the previous line-shaped structure after preheating could not be observed after hot rolling. This can be attributed to the accelerated dissolution of the rod-like precipitates with the interaction of the dislocations generated during high-temperature deformation (500 °C) [38-40]. The dark-field TEM images (Figs. 4.7b and 4.7c, 4.7e and 4.7f) revealed that the spherical Al_3(Sc,Zr) precipitates underwent coarsening in both the alloys during hot rolling, and the number density of these precipitates decreased and the size increased as compared to those of the precipitates observed after the heat treatment (Fig. 4.4). For instance, in the case of the L-Sc alloy, the number density of the spherical Al_3(Sc,Zr) precipitates decreased from 19700 μm^{-3} (after the heat treatment) to 5695 μm^{-3} after hot rolling while in the case of the H-Sc alloy, it decreased from 5188 μm^{-3} to 650 μm^{-3}. The spherical Al_3(Sc, Zr) precipitates in the L-Sc sample had a much higher number density and significantly smaller size than those in the H-Sc sample. For example, the average diameter of the spherical Al_3(Sc, Zr) precipitates in the L-Sc sample was 12.7 nm while that of the precipitates in the H-Sc sample was 37.8 nm. This indicates that the complete dissolution of the rod-like discontinuous

precipitates during hot rolling could not prevent their negative effect on the characteristics of the spherical $Al_3(Sc,Zr)$ precipitates.

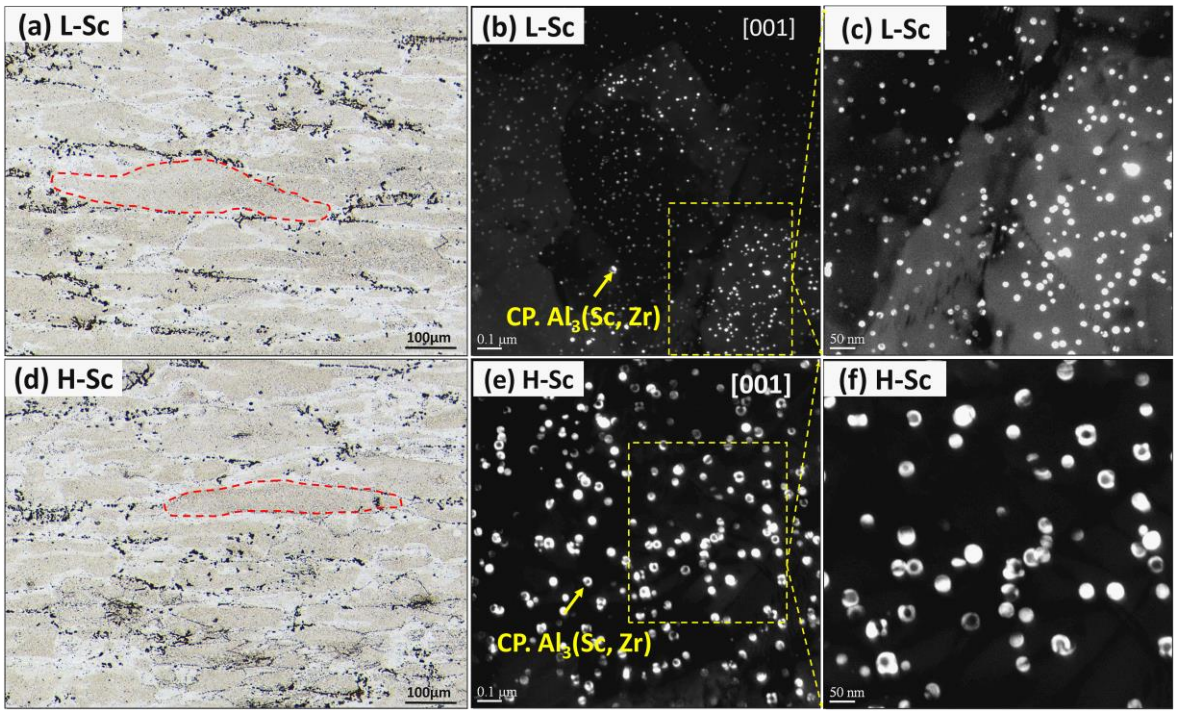

Figure 4.7: Typical optical microscopy images of the samples after hot rolling (a) L-Sc and (d) H-Sc samples. Dark-field TEM images showing the spherical $Al_3(Sc, Zr)$ precipitates after hot rolling (b, c) L-Sc and (e, f) H-Sc samples.

Fig. 4.8 presents a schematic overview of the evolution of the discontinuous and continuous precipitates during the thermomechanical process. Starting from the as-cast condition, the microstructure is similar between the base and L-Sc alloys, while a high density of fan- and line-shaped DCP formed at moving grain boundaries and extended to the grain interior in H-Sc alloy. During the subsequent heat treatment, Mn-dispersoids are precipitated out in all three alloys but with decreasing number density in Sc-containing alloys. Meanwhile, continuous (CP) $Al_3(Sc,Zr)$ precipitates formed in both L-Sc and H-Sc alloy, but its volume was significantly higher in L-Sc alloy than H-Sc alloy. On the other hand, DCP was partially dissolved in H-Sc alloy. With further rolling and annealing, both

Mn-dispersoids and CP $Al_3(Sc,Zr)$ precipitates underwent coarsening in experimental alloys, resulting in a decreased number density and increased size. Moreover, DCP was fully dissolved in H-Sc alloy, and the high Sc solutes from the dissolution of DCP in H-Sc accelerated the coarsening of the $Al_3(Sc,Zr)$ particles, leading to a larger size of CP $Al_3(Sc,Zr)$ in H-Sc alloy than L-Sc alloy through diffusion/growth mechanism.

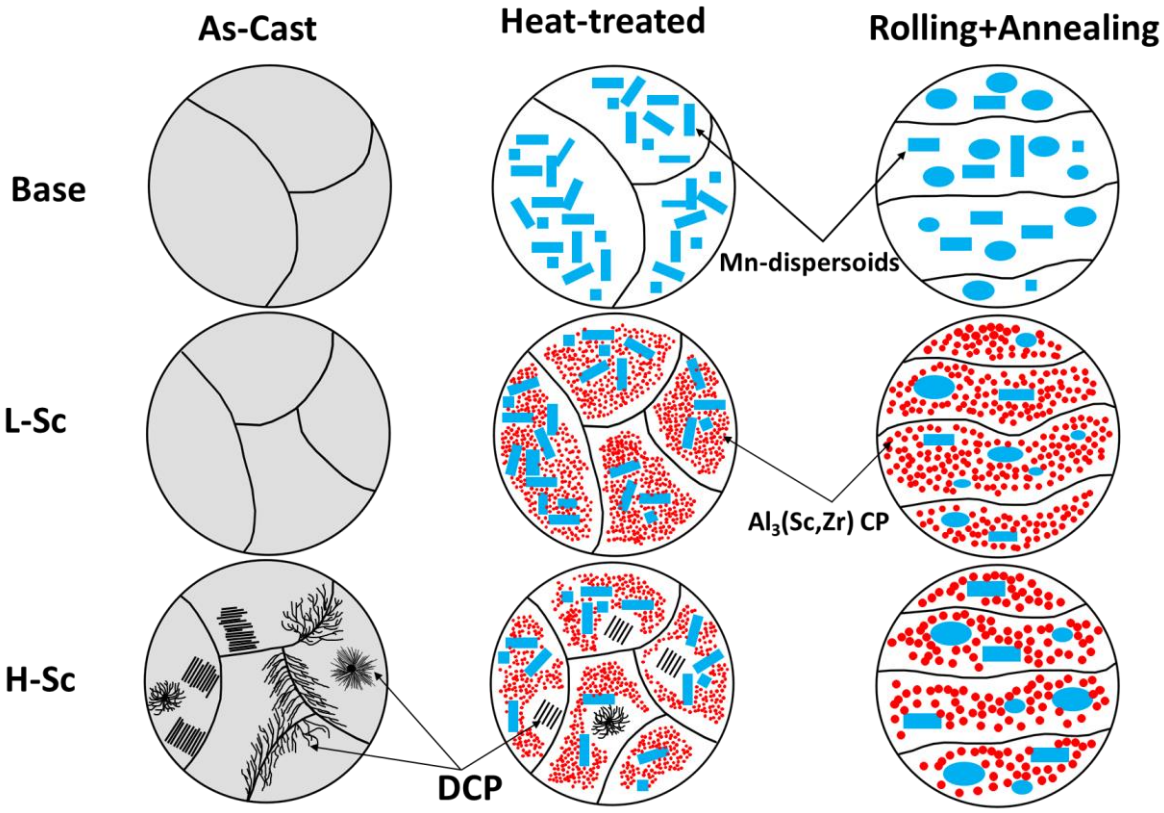

Figure 4.8 A schematic illustration on the evolution of Mn-dispersoids, discontinuous and continuous $Al_3(Sc,Zr)$ precipitates during thermomechanical process.

4.3.4 Tensile properties of hot rolled sheets

As summarized in Fig. 4.8, the evolution of Mn-dispersoids, CP and DCP precipitates varies with the addition of Sc. Therefore, it is expected to have different mechanical propertied related to the evolution of microstructure. Fig .4.9 displays the tensile properties

of the hot-rolled samples tested at room temperature, considering that all the hot-rolled samples were annealed at 300 °C for 5 h to release the thermal stress induced by rolling. As shown in Fig. 4.9a, the stress level is increasing from base alloy to H-Sc and further to L-Sc, confirming the position contribution of Sc on improving the mechanical properties. Fig. 4.9b shows the detailed tensile properties of the three alloys. It can be found that the tensile strength of the Sc-containing alloys was significantly higher than that of the base alloy owing to the additional strengthening effect of the spherical Al_3(Sc,Zr) precipitates. The L-Sc alloy with a low Sc content exhibited the highest YS and UTS while the tensile properties deteriorated with an increase in the Sc content. For instance, the YS and UTS of the L-Sc alloy reached 298.4 and 494.3 MPa, respectively, showing an improvement of 30% in the YS and 8.2% in the UTS relative to the base alloy. On the other hand, the H-Sc alloy showed the YS and UTS values of 261 and 464.9 MPa, respectively, resulting in an improvement of 14% in the YS and 4.2% in the UTS as compared to the base alloy.

Generally, the improvement on the mechanical properties with the addition of Sc can be derived from the nano-sized CP Al_3(ScZr) precipitates after rolling, which could pin the movement of dislocations and grain boundaries. As shown in Figs. 4.7 and 4.8, a high number density of CP Al_3(ScZr) presented after rolling in Sc-containing alloys, providing the additional contribution on the mechanical properties relative to the base alloy.

On the other hand, the different mechanical properties between L-Sc and H-Sc alloys are closely related to the evolution of microstructure with Sc additions: The smaller size and higher density of CP Al_3(Sc,Zr) precipitates (see Fig. 4.7b and Fig. 4.8) in L-Sc alloy contributed to its better tensile properties than those in H-Sc alloy. While the relatively low tensile properties of H-Sc alloy can be attributed to the following reasons: (1) During

solidification, as shown in Fig. 1 and 8, a large number of rod-like DCP were formed, which consumed large amount of Sc and Zr in the solid solution, reducing the number of fine CP Al_3(Sc,Zr) during heat treatment. (2) During the heat treatment process, fine CP Al_3(Sc,Zr) precipitates could not be formed in the vicinity of the discontinuous precipitates (see Figs. 4.4 and 4.8) owing to the depletion of Sc and Zr in the surrounding area, resulting in a locally weakened strengthening effect. (3) Although the DCP dissolved completely during hot rolling (Fig. 4.8), the dissolved Sc in the solid solution could only promote the coarsening of the CP Al_3(Sc,Zr) precipitates through diffusion/growth mechanism (Fig. 4.7), further weakening their strengthening effect [22].

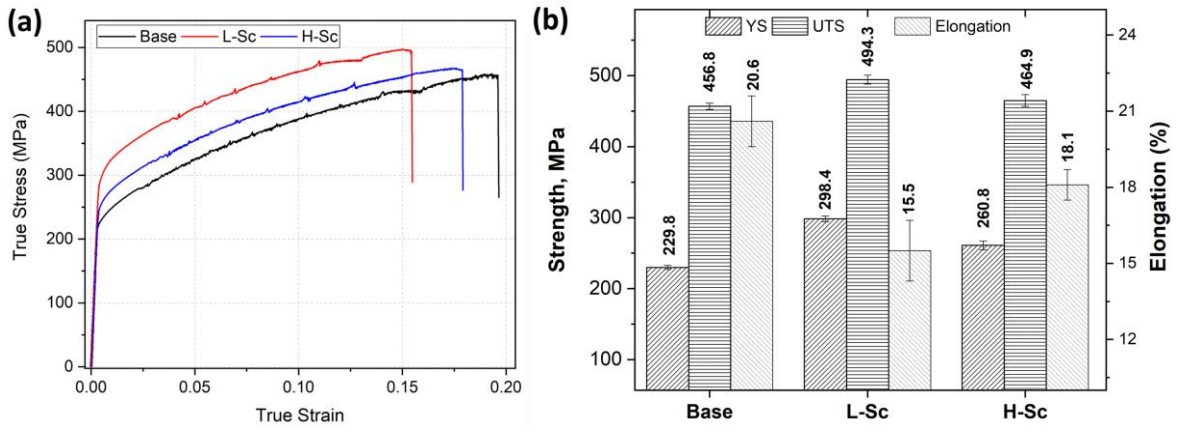

Figure 4.9: Typical true stress-strain curves of the hot-rolled samples (a), average tensile properties of all the three samples (b).

4.4 Conclusions

In this study, we investigated the evolution of discontinuous/continuous Al_3(Sc,Zr) precipitation in an Al-Mg-MnAA5083 alloy during heat treatment and hot rolling as well as its impact on the tensile properties of the alloy. The following conclusions were drawn.

1. When a high amount of Sc (0.43 wt.%) was added, a large number of line- and fan-shaped structures were formed as discontinuous $Al_3(Sc,Zr)$ precipitation during solidification with a cooling rate of ~2 ℃/s. The length of these precipitates ranged from 500 to 860 nm. In the low-Sc alloy (0.15 wt.%), no such discontinuous precipitation was observed.
2. During the heat treatment process in the temperature range of 275-425 °C, two types of precipitates (Mn-bearing dispersoids and spherical $Al_3(Sc,Zr)$ precipitates) were formed as the main strengthening phases. In the H-Sc alloy, the discontinuous $Al_3(Sc,Zr)$ precipitates were partially dissolved, and their length decreased to 200–350 nm. The number density of the spherical $Al_3(Sc,Zr)$ precipitates in the H-Sc alloy was much lower than that in the L-Sc alloy because the discontinuous precipitates consumed large amounts of Sc and Zr in the solid solution.
3. The microhardness of the heat-treated H-Sc alloy was lower than that of the heat-treated L-Sc alloy, which indicates that the discontinuous precipitates had a deleterious effect on the aging hardening response of the alloys.
4. During hot rolling, the discontinuous precipitates dissolved completely, and only the spherical $Al_3(Sc,Zr)$ precipitates and Mn-bearing dispersoids existed in both the Sc-containing alloys. Both the precipitates and dispersoids underwent coarsening during hot rolling. However, the number density of spherical $Al_3(Sc,Zr)$ precipitates in the H-Sc alloy was lower and their size was larger than those in the L-Sc alloy.
5. The tensile properties were significantly improved in Sc-containing alloys, owing to the additional strengthening effect of spherical $Al_3(Sc,Zr)$ precipitates. However, by increasing Sc content, the YS and UTS decreased, confirming the negative effect of

discontinuous precipitates. The low Sc alloy exhibited the highest YS and UTS, showing an improvement of 30% in YS and 11.8% in UTS relative to the base alloy.

Acknowledgments

The authors would like to acknowledge the financial support from the Natural Sciences and Engineering Research Council of Canada (NSERC) and Rio Tinto Aluminum under the Grant No. CRDPJ 514651-17 through the Research Chair in Metallurgy of Aluminum Transformation at the University of Quebec at Chicoutimi.

4.5 References

[1] Z. Li, Z. Zhang, X.G. Chen, Improvement in the mechanical properties and creep resistance of Al-Mn-Mg 3004 alloy with Sc and Zr addition, Materials Science and Engineering A 729(December 2017) (2018) 196-207.
[2] X. Liu, Z. Guo, J. Xue, C. Zhu, P. Zhang, X. Li, Microstructures and mechanical properties of the Al-Cu-Sc alloys prepared by ultrasound-assisted molten salt electrolysis, Journal of Alloys and Compounds 818 (2020) 152870-152870.
[3] Y. Wang, H. Liu, X. Ma, R. Wu, J. Sun, L. Hou, J. Zhang, X. Li, M. Zhang, Effects of Sc and Zr on microstructure and properties of 1420 aluminum alloy, Materials Characterization 154(May) (2019) 241-247.
[4] S. Ikeshita, A. Strodahs, Z. Saghi, K. Yamada, P. Burdet, S. Hata, K.-i. Ikeda, P.A. Midgley, K. Kaneko, Hardness and microstructural variation of Al – Mg – Mn – Sc – Zr alloy, Micron 82 (2016) 1-8.
[5] J. Jiang, F. Jiang, M. Zhang, Z. Tang, M. Tong, Recrystallization behavior of Al-Mg-Mn-Sc-Zr alloy based on two different deformation ways, Materials Letters 265 (2020) 127455-127455.
[6] Y. Peng, S. Li, Y. Deng, H. Zhou, G. Xu, Z. Yin, Synergetic effects of Sc and Zr microalloying and heat treatment on mechanical properties and exfoliation corrosion behavior of Al-Mg-Mn alloys, Materials Science and Engineering A 666 (2016) 61-71.
[7] C.B. Fuller, D.N. Seidman, D.C. Dunand, Mechanical properties of Al (Sc, Zr) alloys at ambient and elevated temperatures, Acta Materialia 51 (2003) 4803-4814.
[8] S.M. Anijdan, D. Kang, N. Singh, M. Gallerneault, Precipitation behavior of strip cast Al–Mg–0.4 Sc–0.15 Zr alloy under single and multiple-stage aging processes, Materials Science and Engineering: A 640 (2015) 275-279.
[9] D.N. Seidman, E.A. Marquis, D.C. Dunand, Precipitation strengthening at ambient and elevated temperatures of heat-treatable Al (Sc) alloys, Acta Materialia 50(16) (2002) 4021-4035.

[10] S.a. Zhou, Z. Zhang, M. Li, D. Pan, H. Su, X. Du, P. Li, Y. Wu, Effect of Sc on microstructure and mechanical properties of as-cast Al-Mg alloys, Materials and Design 90 (2016) 1077-1084.
[11] C.B. Fuller, J.L. Murray, D.N. Seidman, Temporal evolution of the nanostructure of Al(Sc ,Zr) alloys:Part I -Chemical compositions of Al3(Sc1-xZrx) precipitates, Acta Materialia 53 (2005) 5401-5413.
[12] J. Lai, Z. Zhang, X.G. Chen, The thermal stability of mechanical properties of Al-B 4C composites alloyed with Sc and Zr at elevated temperatures, Materials Science and Engineering A 532 (2012) 462-470.
[13] A.K. Lohar, B. Mondal, D. Rafaja, V. Klemm, S.C. Panigrahi, Microstructural investigations on as-cast and annealed Al-Sc and Al-Sc-Zr alloys, Materials Characterization 60(11) (2009) 1387-1394.
[14] J. Røyset, N. Ryum, Scandium in aluminium alloys, International Materials Reviews 50(1) (2005) 19-44.
[15] J. Røyset, N. Ryum, Kinetics and mechanisms of precipitation in an Al-0.2wt.% Sc alloy, Materials Science and Engineering A 396(1-2) (2005) 409-422.
[16] Y. Sun, Q. Pan, Y. Luo, S. Liu, W. Wang, J. Ye, Y. Shi, Z. Huang, S. Xiang, Y. Liu, The effects of scandium heterogeneous distribution on the precipitation behavior of Al3(Sc, Zr) in aluminum alloys, Materials Characterization 174(February) (2021).
[17] Q. Dong, A. Howells, D.J. Lloyd, M. Gallerneault, V. Fallah, Effect of solidification cooling rate on kinetics of continuous/discontinuous Al3(Sc,Zr) precipitation and the subsequent age-hardening response in cold-rolled AlMgSc(Zr) sheets, Materials Science and Engineering A 772 (2020) 138693-138693.
[18] S. Lathabai, P.G. Lloyd, The effect of scandium on the microstructure, mechanical properties and weldability of a cast Al-Mg alloy, Acta Materialia 50(17) (2002) 4275-4292.
[19] W. Zhang, Y. Wu, H. Lu, G. Lao, K. Wang, Y. Ye, P. Li, Discontinuous Precipitation of Nano-Al3Sc Particles in Al-Sc Alloy and its Effect on Mechanical Property, International Journal of Nanoscience 19(1) (2020).
[20] A. Norman, P. Prangnell, R. McEwen, The solidification behaviour of dilute aluminium–scandium alloys, Acta materialia 46(16) (1998) 5715-5732.
[21] N.B. Hopkins, A. M, Constitution and age hardening of Al-Sc alloys, Journal of Materials Science 20 (1985) 2861-2867.
[22] A.K. Lohar, B.N. Mondal, S.C. Panigrahi, Influence of cooling rate on the microstructure and ageing behavior of as-cast Al–Sc–Zr alloy, Journal of Materials Processing Tech. 210(15) (2010) 2135-2141.
[23] A. Mochugovskiy, V. Levchenko, N.Y. Tabachkova, W. Mufalo, V. Portnoy, Precipitation behavior of L12 Al3Zr phase in Al-Mg-Zr alloy, Materials Characterization 139 (2018).
[24] D.O. P. B. Prangnell, S. W. M, Discontinuous precipitation in high Li content Al-Zr alloys, Acta Metallurgica Et Materialia 42(2) (1994) 419-433.
[25] A.Y. Algendy, K. Liu, X.G. Chen, Evolution of dispersoids during multistep heat treatments and their effect on rolling performance in an Al-5 % Mg-0 . 8 % Mn alloy, Materials Characterization 181(September) (2021) 111487-111487.
[26] S.M. Allen, Foil thickness measurements from convergent-beam diffraction patterns, Philos. Mag A 43(2) (1981) 325-335.

[27] D.B. Williams, E.P. Butler, Grain boundary discontinuous precipitation reactions, International Metals Reviews 4590 (2013) 153-183.
[28] Y.W. Riddle, T.H. Sanders, A Study of Coarsening , Recrystallization , and Morphology of Microstructure in Al-Sc- (Zr) - (Mg) Alloys, METALLURGICAL AND MATERIALS TRANSACTIONS A 35 A (2004) 341-350.
[29] A.G. Mochugovskiy, A.V. Mikhaylovskaya, N.Y. Tabachkova, V.K. Portnoy, The mechanism of L12 phase precipitation, microstructure and tensile properties of Al-Mg-Er-Zr alloy, Materials Science and Engineering A 744 (2019) 195-205.
[30] E. Hornbogen, Systematics of the Cellular Precipitation Reactions, Metallurgical transactions. A 3(November) (1972) 2717-2727.
[31] E.A. Marquis, D.N. Seidman, Nanoscale structural evolution of Al 3 Sc precipitates in Al(Sc) alloys, Acta Materialia 49(11) (2001) 1909-1919.
[32] D. Tsivoulas, J. Robson, Heterogeneous Zr solute segregation and Al3Zr dispersoid distributions in Al–Cu–Li alloys, Acta Materialia 93 (2015) 73-86.
[33] W. Lefebvre, F. Danoix, H. Hallem, B. Forbord, A. Bostel, K. Marthinsen, Precipitation kinetic of Al3(Sc, Zr) dispersoids in aluminium, Journal of Alloys and Compounds 470 (2009) 107-110.
[34] A.G. Mochugovskiy, A.V. Mikhaylovskaya, Comparison of precipitation kinetics and mechanical properties in Zr and Sc-bearing aluminum-based alloys, Materials Letters 275 (2020) 128096-128096.
[35] Y. Du, Y.A. Chang, B. Huang, W. Gong, Z. Jin, H. Xu, Z. Yuan, Y. Liu, Y. He, F.Y. Xie, Diffusion coefficients of some solutes in fcc and liquid Al: Critical evaluation and correlation, Materials Science and Engineering A 363(1-2) (2003) 140-151.
[36] A.V. Mikhaylovskaya, A.G. Mochugovskiy, V.S. Levchenko, N.Y. Tabachkova, W. Mufalo, V.K. Portnoy, Precipitation behavior of L12 Al3Zr phase in Al-Mg-Zr alloy, Materials Characterization 139(February) (2018) 30-37.
[37] E.a. Marquis, D.N. Seidman, Coarsening Kinetics of Nanoscale Al-3Sc Precipitates in an Al-Mg-Sc Alloy, Acta Mater. 53 (2005) 4259-4268.
[38] K. Yan, Z. Chen, W. Lu, Y. Zhao, W. Le, S. Naseem, Nucleation and growth of Al3Sc precipitates during isothermal aging of Al-0 . 55 wt % Sc alloy, Materials Characterization 179(May) (2021) 111331-111331.
[39] M. Cabibbo, E. Evangelista, M. Vedani, Influence of severe plastic deformations on secondary phase precipitation in a 6082 Al-Mg-Si alloy, Metallurgical and Materials Transactions A 36(5) (2005) 1353-1364.
[40] I. Lomaev, E. Elsukov, On the analysis of the mechanisms of the strain-induced dissolution of phases in metals, PHYSICS OF METALS AND METALLOGRAPHY C/C OF FIZIKA METALLOV I METALLOVEDENIE 102(2) (2006) 186.

Chapter 5: Role of Mn-bearing dispersoids on the tensile properties, and recrystallization resistance of rolled Al-3Mg-0.8Mn alloy

Ahmed Y. Algendy[1], Kun Liu[1], X.-Grant Chen[1]
[1] Department of Applied Science, University of Quebec at Chicoutimi, Saguenay (QC), G7H 2B1, Canada

This article is under internal review

Abstract

In the present study, the role of Mn-dispersoids on the tensile properties and recrystallization resistance in an Al3Mg0.8Mn rolled alloy was investigated. During heat treatment, the modified low-temperature three-step heat treatment (275 ^{o}C / 12h + 375 ^{o}C / 48 h + 425 ^{o}C / 12h) generated a higher number density of Mn-bearing dispersoids with finer size compared to the high-temperature industrial heat treatment, a significant increase of mechanical properties after both hot and cold rolling. The yield strength (YS) reached 196 MPa and 233 MPa after hot/cold rolling and annealing, respectively, showing an improvement of 30% over the samples with the industrial heat treatment. In addition, the modified three-step heat treatment showed a stronger recrystallization resistance after hot and cold rolling, owing to the higher number density of Mn-dispersoids and the lower fraction of dispersoid free zone (DFZ) compared to the base heat treatment. The YS contributions of various strengthening mechanisms after hot and cold rolling were quantitatively analyzed using the constitutive equations. The predicted YSs were in good agreement with the experimentally measured values.

Keywords: Al-Mg-Mn alloy, Mn-bearing dispersoids, Hot and cold rolling, Mechanical properties, Recrystallization resistance.

5.1 Introduction

Al-Mg-Mn alloys with medium strength, good toughness and corrosion resistance, and good forming performance makes them suitable for a broad range of applications, especially in transportation and chemical industries, such as internal panels, pressure vessels, tanks, boilers [1-4]. Solid solution strengthening from Mg and plastic deformation are two primary aspects contributing to the strength of Al-Mg-Mn 5xxx alloys [5-7].

The typical manufacturing process of non-heat-treatable Al-Mg-Mn alloys includes casting, homogenization, and then hot and cold deformation [8]. Generally, homogenization treatment is applied after casting to reduce the element segregation produced during solidification and prepare the cast ingots for the following hot deformation [9]. During homogenization, Mn-bearing dispersoids precipitate out in the dendritic cells/grains, improving the deformed structure by pining the dislocation movements and grain boundary migration [10-12]. Therefore, these submicron dispersoids may control the performance of the final product. In Al-Mg-Mn 5xxx alloys, the homogenization treatment is conducted at relatively high temperatures (500–550 °C), resulting in coarse dispersoids with a low number density [9, 13-15]. For example, Engler *et al.* [9, 13] studied the precipitation of dispersoids at various homogenization cycles and their influence on recrystallization resistance; the minimum treatment temperature was performed at 500 ^{o}C, resulting in a low number density of coarse dispersoids. Y. Wang *et al.* [16] reported the precipitation of Al_6Mn dispersoids during homogenization under various condition in Al–6Mg–0.8 Mn alloys, including single

and two-step heat treatments. The results showed that a high-volume fraction of Al_6Mn dispersoids improved the flow stress during the hot compression tests, and effectively inhibited the growth of recrystalized grains. In our previous study [17], it is found that the multistep heat treatments produced high volume fractions of submicron Mn-bearing dispersoids, and hence improved sheets' rolling performance and mechanical properties.

The final product of Al-Mg-Mn alloys is generally delivered in sheet form with different thicknesses for various structural applications. Therefore, the cast materials undergo hot and cold rolling after homogenization to produce the final sheets. During hot rolling, dynamic recovery (DRV) and dynamic recrystallization (DRX) control the work hardening and alloy formability. Therefore, retardation of both DRV and DRX could improve the alloy's properties. According to Huang *et al.* [18], Mn-bearing dispersoids played an essential role in the deformation behavior of Al-Mg alloys by impeding the subgrain boundaries migration and retard the recrystallization. After hot rolling, the materials undergo cold rolling to reach the required thickness of final products (1 mm and less) [8, 9]. During the cold rolling process, many defects (vacancies and dislocations) were introduced with high stored energy, resulting in structural instability. Subsequent annealing treatment stabilized the alloy's deformation through the recovery and recrystallization process. Both recovery and recrystallization occurred during the annealing treatment, lowering the hardening effect [9, 19-21]. The degree of recrystallization strongly depends on the annealing temperature and time. Engler *et al.* [9] found that the degree of recrystallization is strongly affected by the volume fraction and the size of dispersoids formed during homogenization (Zener drag effect). Therefore, controlling the size and distribution of Mn-bearing dispersoids during a proper heat treatment can significantly improve the alloy performance.

To date, the role of Mn-bearing dispersoids on the mechanical properties and recrystallization resistance of rolled Al-Mg-Mn sheets is rarely reported. The present study was undertaken to understand the role of Mn-bearing dispersoids in a typical Al-3Mg-0.8Mn rolled alloy and their influence on the mechanical properties and recrystallization resistance during hot and cold rolling. The different size and distribution of dispersoids were produced using a modified three-step heat treatment and a conventionally industrial heat treatment. The microstructure evolution during homogenization, hot and cold rolling was characterized using optical microscopy (OM), scanning electron microscopy (SEM), electron backscatter diffraction (EBSD), and transmission electron microscopy (TEM). The strength contributions were analysed using constitutive equations to understand various strengthening mechanisms.

5.2 Experimental Procedure

The Al-3Mg-0.8Mn alloy was prepared in the present work, and its chemical composition was very closed to the specification of a typical AA5454 alloy. The material was melted in a graphite crucible in an electrical resistance furnace. The melt was grain-refined by adding an Al–5Ti–1B master alloy. The melt was cast into a permanent steel mold with a cooling rate of ~2 ℃/s during solidification to produce the cast ingots with dimensions of 30 x 40 x 80 mm. The chemical compositions were analyzed using an optical emission spectrometer, and the results are listed in Table 5.1.

Table 5.1: The chemical composition of the experimental alloy (wt.%)

		Mg	Mn	Si	Fe	Cu	Cr	Ti	Al
AA5454 [22]	Min.	2.4	0.5				0.05		Bal.
	Max.	3	1	0.25	0.40	0.10	0.20	0.20	
Present alloy		3.01	0.81	0.27	0.31	0.10	0.14	0.09	Bal.

A programmable electric air circulating furnace was used for the heat treatment with a 60 ^{o}C/h heating rate. The experimental alloy was subjected to a modified low-temperature three-step heat treatment (3S) (275 ^{o}C / 12h + 375 ^{o}C / 48 h + 425 ^{o}C / 12h) followed by water quenching, to facilitate the precipitation Mn-bearing dispersoids [17]. In addition, a typical high-temperature industrial heat treatment (Ind) (430 ^{o}C/2 h + 480 ^{o}C/2 h + 525 ^{o}C/2 h) was performed as the base case for comparison of the dispersoid's performance [17, 23]. After the heat treatments, the homogenized ingots were machined to 26.5 mm thickness, and then hot-rolled to a final sheet with a thickness of 3.2 mm with 88% total reduction. The hot rolling was performed in multiple passes at a temperature of 500 ± 20 °C. Afterward, all hot-rolled sheets were isothermally annealed at 300 ^{o}C/5 h to relieve the induced thermal stress prior the mechanical testing. Next, the hot-rolled sheet was cold-rolled to a final thickness of 1 mm with a 69% reduction. The cold-rolled samples were annealed at 150 - 400 ^{o}C with a 50 ^{o}C interval for 1 h, followed by air cooling.

The tensile properties of the hot and cold-rolled sheets were measured using an Instron 8801 servo-hydraulic testing unit with an initial strain rate of 0.3 mm/min (in the elastic region), then the strain rate increased to 1 mm/min. The tensile samples were machined

according to ASTM E8/E8M-16a in the rolling direction with the gauge sizes of 3 x 6 mm for hot-rolled samples and 1 x 6 mm for cold-rolled samples. Average results were obtained from three repeated tests.

Samples under various conditions, such as after heat treatment and hot/cold rolling, were taken for microstructure observations. The microstructures were observed under optical microscopy (Nikon, Eclipse ME600), Scanning Electron Microscope (SEM, JEOL-JSM-6480LV), and transmission electron microscope (TEM, JEM-2100). The homogenized samples were etched in 0.5% HF for 30 seconds for clear observation of the dispersoid distribution and dispersoids free zone (DFZ). Image Analysis Software (Clemex PE 4.0) was used to analyze the area fraction of DFZs. The grain structure was characterized under polarized light after electro-etching using Barker's reagent (4 mL HBF4 + 200 mL H_2O) at 17 V for 3 min. The deformed samples were sectioned in the rolling direction and observed under Electron Backscattered Diffraction (EBSD) with scan step sizes of 1 µm. EBSD data were subsequently processed by using HKL Channel 5 software. The characteristics and distribution of Mn-bearing dispersoids were investigated using TEM operated at 200 kV. TEM thin foils were prepared in a twin-jet electro-polisher using a solution of 30% nitric acid in methanol at 20 volts and -20 ^{o}C. The size and number density of Mn-bearing dispersoids were measured using ImageJ analysis software on TEM images. The number density and the volume fraction calculation of Mn-bearing dispersoids were determined using the following equations:

$$N_d = \frac{N}{A(D+t)} \qquad (1)$$

$$V_f = A_d \frac{KD}{KD+t}(1 - A_{DFZ}) \qquad (2)$$

Where N is the number of particles in the TEM image, V_f is the volume fraction of dispersoids, A is the total area, D is the equivalent diameter, A_d is the area fraction of dispersoids in TEM imaged, K is the average shape factor of dispersoids equal to 0.45 [24]; A_{DFZ} is the area fraction of DFZ measured in the optical images, and t is the thickness of the TEM foil measured according to [25].

5.3 Results and discussions

5.3.1 Microstructure evolution during heat treatments

Fig. 5.1 displays the microstructure of the experimental alloy after both 3S- and Ind-heat treatments, showing the distribution of intermetallic phases and dispersoids. As shown in Figs. 5.1a and 5.1b, α-$Al_{15}(Fe,Mn)_3Si_2$ and Mg_2Si were the major intermetallic particles after heat treatment [26], while their sizes were finer after Ind-heat treatment due to the higher temperature than those after 3S-heat treatment. On the other hand, Mn-containing dispersoids precipitated during the heat treatment. As shown in Figs. 5.1 c and 5.1d after 0.5% HF etching, a large number of dispersoids were observed in the dendrite cell/grain interiors (dispersoid zone, DZ), while the areas adjacent to the intermetallic particles have few or no dispersoids, namely dispersoids free zones (DFZ) due to the depletion of dispersoid forming alloying elements [17, 24]. Due to the higher homogenization temperature (525 ^oC) in the Ind-heat treatment, the DFZs became more noticeable and wider compared to the 3S-heat treatment (28 vol.% vs 21.3vol.%).

The distribution and features of the submicron dispersoids in the DZ were further studied using TEM, which are shown in Fig. 5.2. Under both heat treatments, two kinds of dispersoids with different morphologies were observed. The round/irregular-shaped one was

identified as small α-Al(Fe,Mn)Si, and the plate/rod-like one was considered as Al_6(Mn,Fe) according to the TEM-EDS results (Table 5.2) and literature [9]. To simplify, both of them are designated as "Mn-dispersoids" in the following test since they are thermally stable and have a similar influence on the mechanical properties and recrystallization during the rolling and annealing processes.

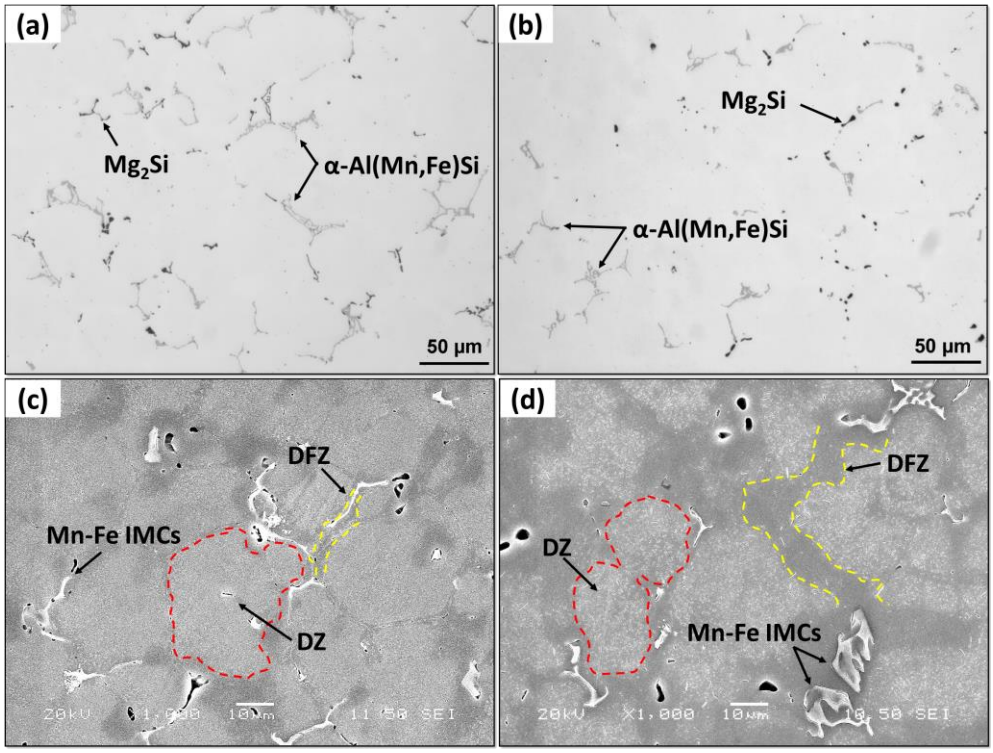

Figure 5.1: The microstructure evolution after heat treatments: (a and c) 3S and (b and d) Ind heat treatments.

As shown in Figs. 5.2a and 5.2b, the size and number density of Mn-dispersoids are strongly related to the heat treatment parameters, particularly the temperature [9, 13, 17]. Due to the higher temperature in the Ind-heat treatment (520 ^{o}C) that was higher than the formation temperature (370 ^{o}C) of Mn-bearing dispersoids [17, 24], the Mn-dispersoids became coarse with a remarkable reduction in their number density, as shown in Fig. 5.2b. By contrast, the 3S-heat treatment exhibited a higher number density and finer size of Mn-

dispersoids. For instance, compared with Ind-heat treatment, the size of Mn-dispersoids decreased by 60%, while the number density significantly increased by 83%, as shown in Fig. 5.2c.

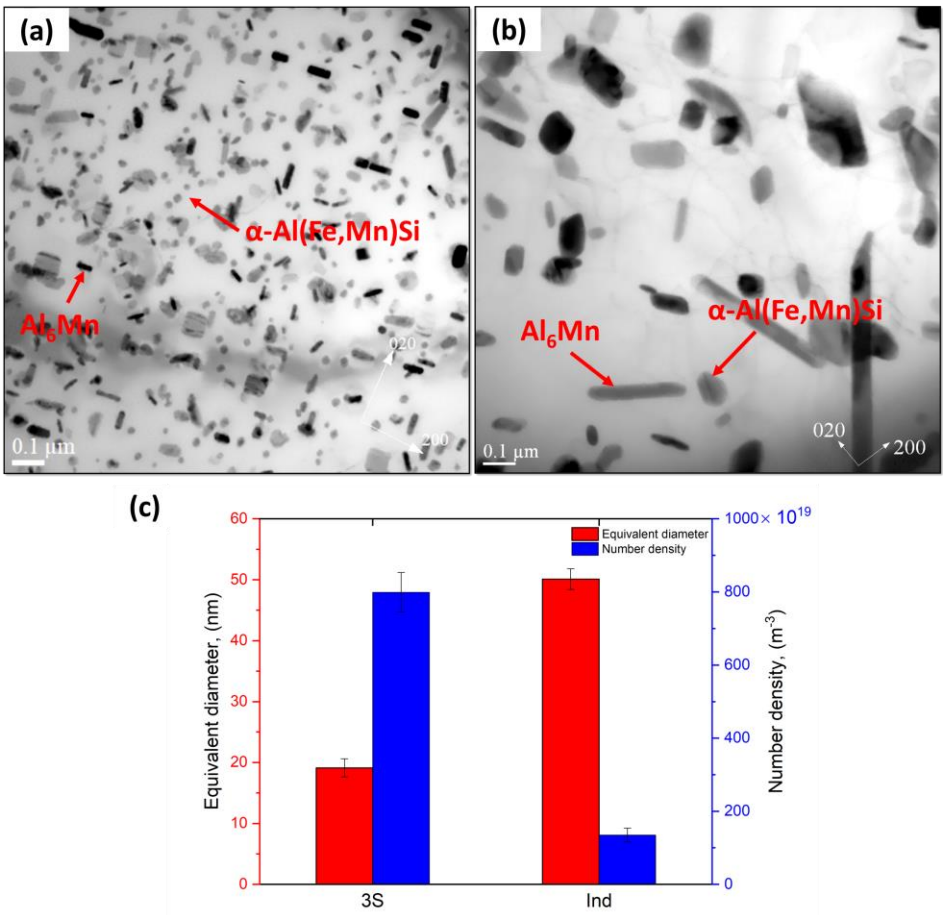

Figure 5.2: Bright field TEM images showing the distribution of Mn-bearing dispersoids under (a) 3S-heat treatment, (b) Ind-heat treatments, and (c) the quantitative analysis of Mn-dispersoids.

Table 5.2: Statistical TEM-EDS analysis (at. %) of different dispersoids in experimental alloys.

	Mg	Mn	Fe	Si	Cr	Al
α-Al(Fe,Mn)Si	2.90±0.5	2.88±0.4	0.29±0.6	0.99±0.7	0.42±0.9	92.52±0.7
Al_6Mn	2.81±0.6	2.95±0.3	0.31±0.4	--	0.47±0.4	93.46±0.9

5.3.2 Microstructure evolution and mechanical properties after hot rolling

After heat treatments, the alloys underwent the hot rolling, and the distribution of Mn-dispersoids after hot rolling is shown in Fig. 5.3. It can be seen that the dispersoids become larger with a lower number density than those observed after heat treatments (Fig. 5.2). The coarsening of Mn-dispersoids could be attributed to the higher rolling temperature (500 ^{o}C) and the interaction of dispersoids with dislocation during deformation, which both could accelerate the coarsening of dispersoids [17, 27-29]. The size, number density, and volume fraction of dispersoids were quantitatively analyzed and results are listed in Table 5.3. Similar to heat-treated conditions, alloy with the 3S-heat treatment showed an appreciable higher number density and finer size of dispersoid than those observed after the Ind-heat treatment. For instance, the number density of dispersoids of alloy treated with 3S could reach 343×10^{19} m^{-3} compared to 72×10^{19} m^{-3} from Ind-treated sample, which was 6 times higher. Meanwhile, the size is also much finer in the 3S-treated sample relative to that in the Ind-treated sample (29 vs 65 nm).

Table 5.3: Characteristics of Mn-dispersoids after hot rolling and the average Mg solid solution

Conditions	Dispersoids characteristics		
	Equivalent diameter $\overline{D}$, nm	Number density, $\times 10^{19}$, m^{-3}	Volume fraction, V_f
3S	29.1±1.1	343±50.7	1.6
Ind	65.4±2.4	72±8.2	1.4

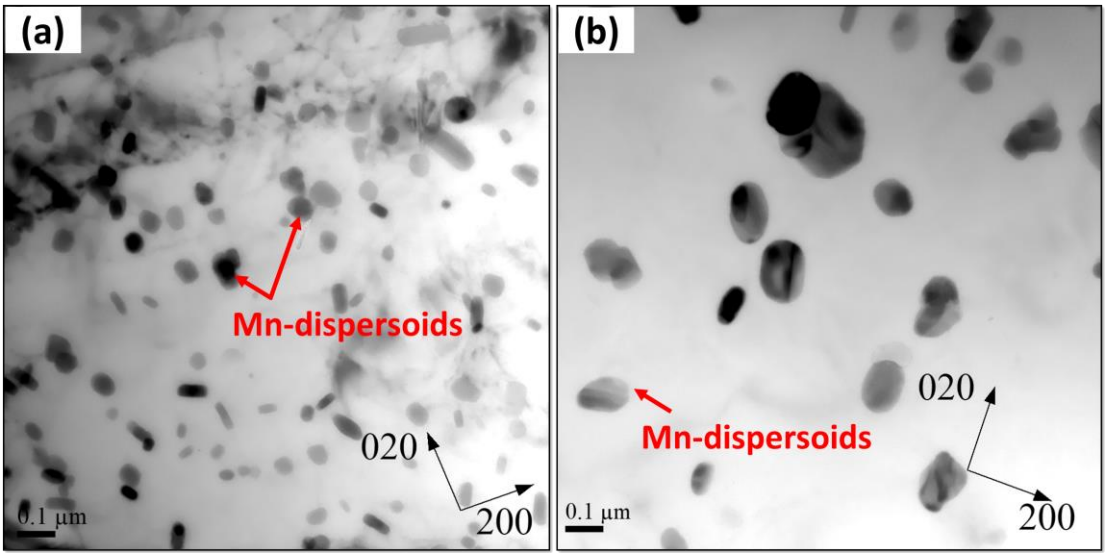

Figure 5.3: Bright field-TEM images showing the distribution of dispersoids after rolling and annealing (a) 3S and (b) Ind

Fig. 5.4 shows the deformed grain structure via the Euler orientation maps (Figs. 5.4a and 5.4b) and recrystallization fraction maps (Figs. 5.4c and 5.4d) after hot rolling and subsequent annealing (300 ^{o}C/5h). The quantitative analysis of the EBSD maps was performed, and the results are presented in Fig. 5.5. It can be seen that both samples exhibited the mixed deformed and recrystallized grains. Both samples showed a large fraction of low angle boundary (2^{o}-5^{o}) and medium boundary (5^{o}-15^{o}) resulting from the high dislocation density produced during the hot rolling. However, samples with the 3S-heat treatment showed fine equiaxed and recrystallized grains (blue color Fig. 5.4c) along the inter-dendritic regions with an average size of 17-20 µm. On the other hand, the recrystallized grain after the Ind-heat treatment could reach 30-50 µm (blue color Fig. 5.4d). As a result, samples with 3S display the higher fraction of deformed grains (67%) with the lower recrystallization fraction (23%) compared to the Ind-heat treatment (Fig. 5.5), indicating a higher recrystallization resistance. In addition, a lower fraction of HAB (23%) in the sample with 3S-heat treatment also confirms the higher recrystallization resistance. This can be related to

the evolution of Mn-dispersoids after hot rolling. Zener drag force (P_Z) commonly expresses the effectiveness of second phase particles (Mn-dispersoids) in inhibiting the growth of recrystallized grain [16, 30]. Generally, Pz is proportional to the ratio of the volume fraction to the particle size (V_f/r). The higher ratio of V_f/r leads to stronger Pz, which was the case for alloy treated after 3S. As shown in Fig. 5.3, samples treated with 3S-heat treatment show a higher number density of finer Mn-dispersoids, resulting in a larger P_Z and a resultant higher recrystallization resistance than the sample with Ind-heat treatment.

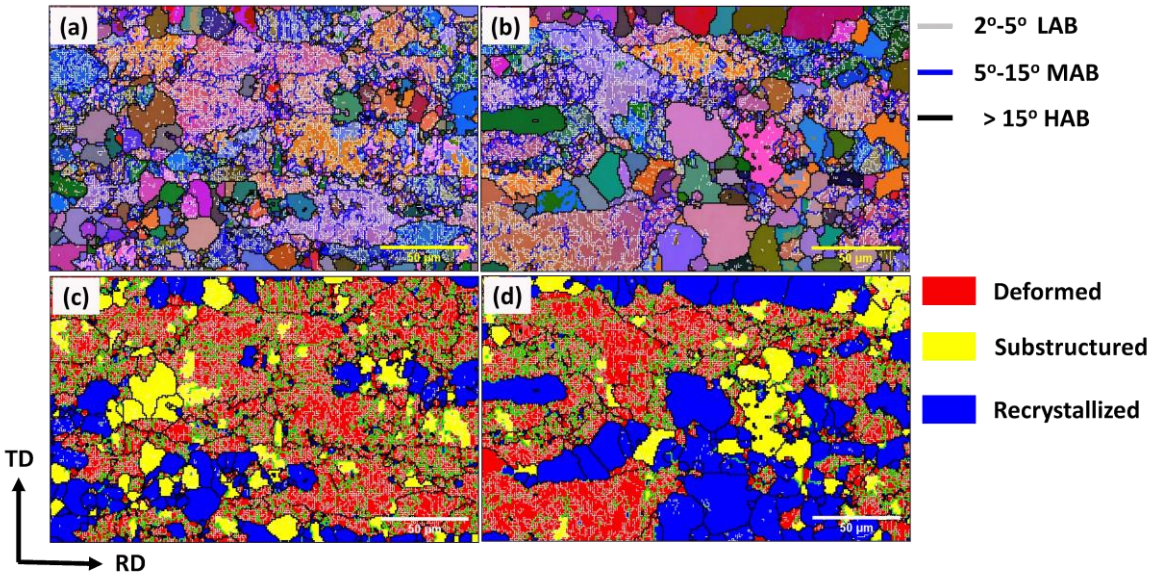

Figure *5.4*: Grain structure evolution after hot rolling and subsequent annealing after (a, c) 3S-heat treatment and (b, d) Ind-heat treatment. In Fig. 4a-b, white lines remark LAB (2–5 °), blue lines MAB (5–15 °) and black lines HAB (>15 °).

As shown in Figs 5.3-5.5, the distribution of dispersoids and grain structure after hot rolling is remarkable different between 3S-treated and Ind-treated samples. Therefore, it is expecting to have different mechanical properties. The tensile properties after hot rolling are shown in Fig.5.6. Fig. 5.6a shows the typical engineering stress-strain curves of the experimental samples, where the strength sharply increased reaching the maximum value

(UTS) and then dropped after a short plateau at the maximum strength (UTS). The average tensile data are listed in Fig. 5.6b. The YS and UTS of the 3S-treated samples were significantly higher than those of the Ind-treated samples, while the elongation of the 3S-treated samples decreased. For instance, the YS and UTS of samples with 3S-heat treatment reached 196 and 305 MPa, respectively, showing an improvement of 30% in YS and 6% in UTS compared to the samples with Ind-heat treatment. On the other hand, the elongation after 3S-heat treatment was decreased compared to the samples after Ind-heat treatment (19.1% vs 25.4%).

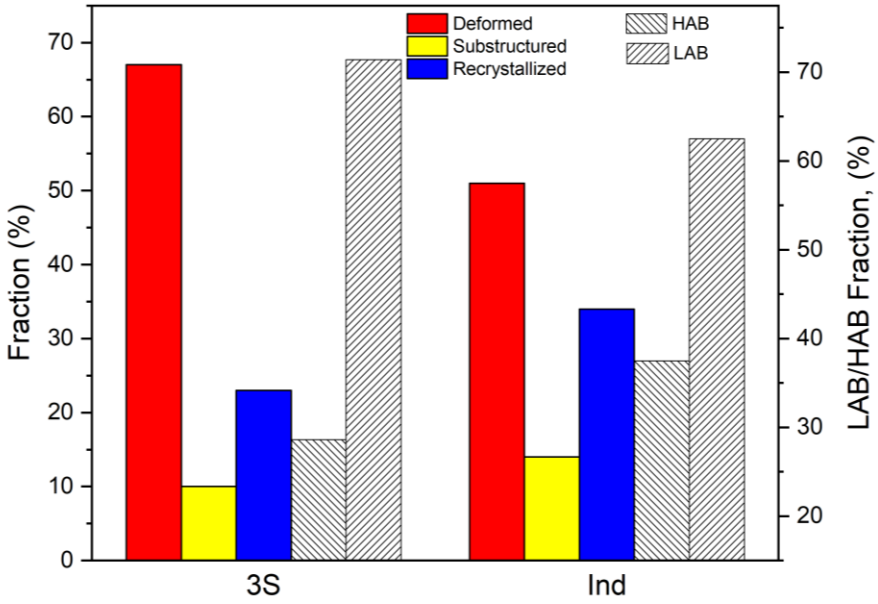

Figure 5.5: The quantitative results of EBSD maps after hot rolling and annealing. The low angle boundary LAB < 15^{o} and high angle boundary HAB ≥ 15^{o}.

After hot rolling and annealing, the solid solution hardening (due to Mg), second phase particles (Mn-dispersoids) and grain boundary hardening are the major strengthening mechanisms, controlling the alloy strength. However, the contribution of the solid solution hardening of Mg is almost the same in both conditions. Therefore, the higher tensile strength of 3S-treated samples after hot rolling could be explained by the presence of a higher number

density of finer dispersoids and the deformed grain structure relative to the Ind-treated samples. In addition, another factor may influence the mechanical properties is the dispersoid-free zones (DFZs) [31, 32]. As shown in Fig. 5.1d, the homogenization at a higher temperature (the Ind-treated samples) displayed a large fraction of DFZ compared to the 3S-treated samples. It is reasonable to assume that the area fraction of the DFZ did not change much before and after hot rolling. These areas had almost no Mn-dispersoids, making them favorable for the easy nucleation and growth of the new recrystallized grains during hot rolling and annealing. As shown in Fig. 5.4, the recrystallization was mainly concentrated along the inter-dendritic regions where DFZ exists. Due to the lower area fraction of DFZ after 3S-heat treatment, the samples show a less recrystallization fraction than the samples with Ind-heat treatment (Fig. 5.5), hence improving the tensile strength to some extent.

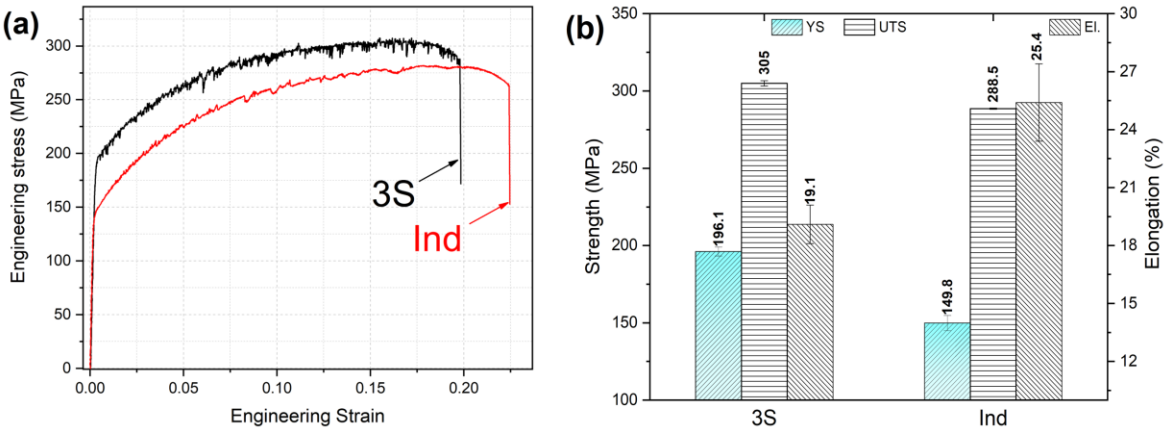

Figure 5.6: Typical stress-strain curves of the experimental alloys at room temperature (a), the tensile properties data obtained from the average of three samples (b).

5.3.3 Mechanical properties and microstructure evolution during cold rolling and annealing

The mechanical properties of the cold-rolled and annealed sheets as a function of the annealing temperature are shown in Fig. 5.7. After cold rolling, the mechanical properties are significantly higher than that after hot rolling (Fig. 5.6) due to the strong strain hardening

effect. During the annealing process, the YS and UTS decrease with increasing the annealing temperature with an increase in the elongation. As shown in Fig. 5.7, at relatively low annealing temperature (150-250 ^{o}C), the YS gradually decreases with increasing the temperature; however, there was a sharp decrease at 300-350 ^{o}C followed by a plateau until to 400 ^{o}C. This should be related to the evolution of deformed grain structure during annealing [20, 21, 33]. Fig. 5.8 shows the grain structure after annealing at different temperatures, revealed by the electrolytic etching. The grain structure was dominated by the elongated and recovered grains in the rolling direction up to 250 ^{o}C. However, at 300 ^{o}C, partially recrystallized grains occurred in the samples treated with both 3S and Ind treatments, resulting in a sharp decrease on the mechanical properties. When further increasing the annealing temperature to 400 ^{o}C, the recrystallization continued and the recrystallized grains slowly grew, making a plateau on the mechanical properties.

The YSs of the 3S-treated samples were always higher than those after Ind-treatment. As shown in Fig. 5.7, the YS difference between two conditions was almost constant until 250 ^{o}C, which can be attributed to the main contribution of Mn-dispersoids since the grain structures under two conditions were similar with elongated and deformed grains. When annealed at 300 ^{o}C, a remarkable increase in YS difference between two conditions was observed. For instance, it was 233 MPa in the 3S-treated sample, while it was 179 MPa in the Ind-treated sample. The difference of YS was 54 MPa that was much larger than that at 25-250 ^{o}C. For this large difference, apart from the contribution of Mn-dispersoids, the difference from the grain structure after annealing should be considered. As shown in Figs. 5.8e and 5.8f, the 3S-treated sample were less recrystallized and contained more deformed grains (shown with dash white lined in Fig. 5.8e) than the Ind-treated sample.

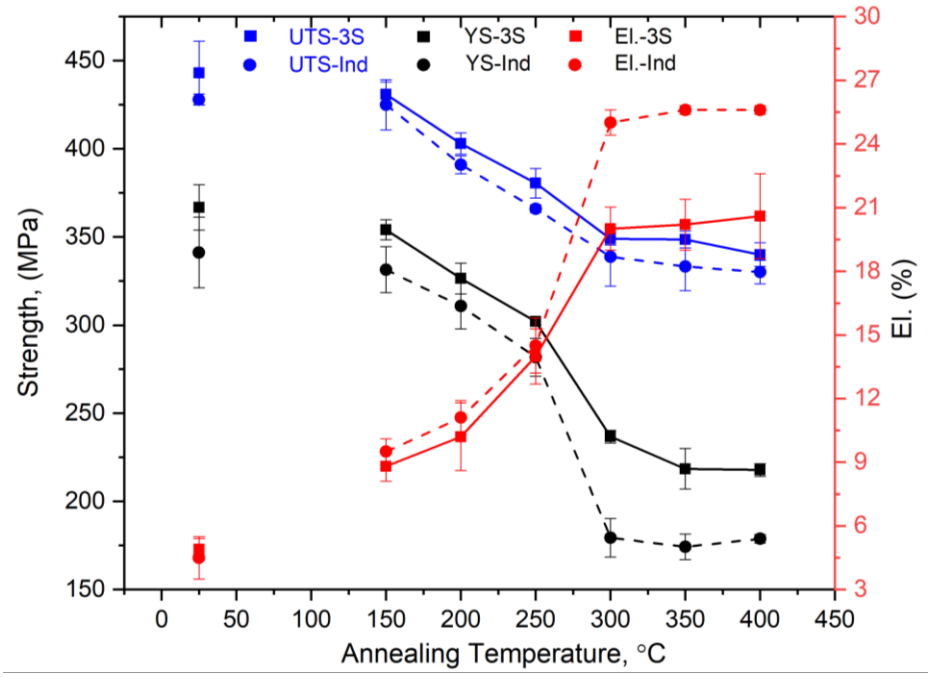

Figure 5.7: The mechanical properties after cold rolling as a function of the annealing temperature.

The samples after 300 ^{o}C annealing were further observed using EBSD technique, the results are presented via the Euler orientation maps and recrystallization maps in Fig. 5.9. As shown in Fig. 5.9, the sample with 3S-heat treatment shows a mixture of deformed grains with LAB and recrystallized grains, while the sample with Ind-treatment were almost fully recrystallized. The quantitative data of EBSD maps in Figs. 5.9c and 5.9d revealed that sample with 3S-heat treatment display a lower recrystallization fraction of 60% and higher deformed grain fraction of 18%. On the other hand, the samples with Ind-heat treatment show a higher recrystallization fraction of 79% with a negligible fraction of deformed grains. With further increasing the temperature, the difference between two conditions became constant but was still higher than that annealed at 150-250 ^{o}C, resulting from the different contributions of Mn-dispersoids and grain structure. The details of various strengthening mechanism will be discussed in the next section.

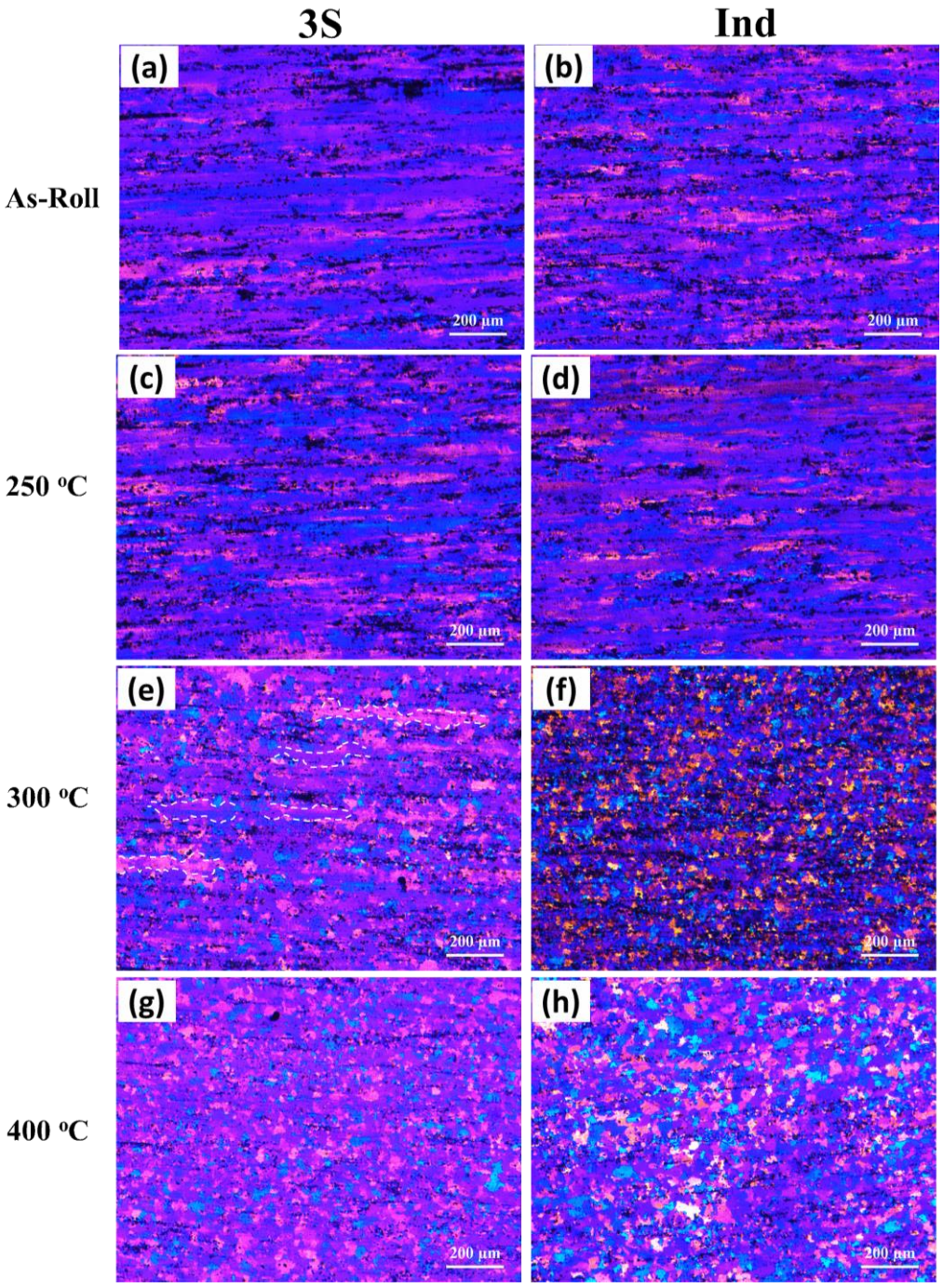

Figure 5.8: Optical microscopy images after electrolytic etching under polarized light of cold rolled and annealed samples under both 3S- and Ind-treated conditions.

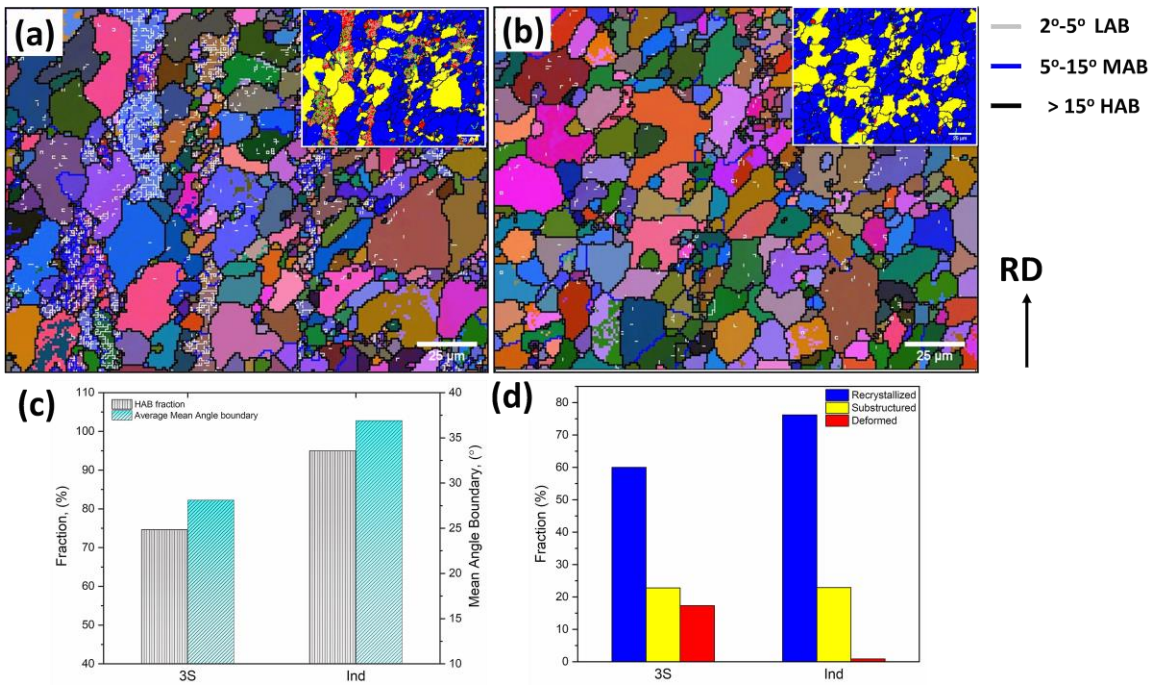

Figure 5.9: Euler orientation maps and recrystallization fraction maps of samples annealed at 300 °C/1h: (a) 3S-, (b) Ind-heat treatments. In Fig. 9a-b, white lines remark LAB (2–5°), blue lines MAB (5–15°) and black lines HAB (>15°). The Quantitative data of EBSD results (c and d).

5.3.4 Constitutive analysis of strengthening mechanisms

As shown in Figs. 5.6 and 5.7, the mechanical properties of hot-rolled and cold-rolled samples are varying with the alloy treated after 3S- and Ind-heat treatment. The yield strengths in the two cases - after hot rolling and annealing (300°C/5h) and cold rolling and annealing (300°C/1h) - were analytically calculated using constitutive equations, to better understand the contribution of different strengthening components, including the solid solution hardening, Mn-dispersoid strengthening, and grain/subgrain boundary strengthening [6, 17, 34, 35]. Assuming that the contributions of the strengthening mechanisms are independent and can be expressed as follows:

$$\Delta\sigma_{\text{overall YS}} = \sigma_{\text{o}} + \Delta\sigma_{\text{SS}} + \Delta\sigma_{\text{GB}} + \Delta\sigma_{\text{dispersoids}} \qquad (3)$$

where σ_o is the strength of the Al matrix (1100-O), equal to 34 MPa [36], and $\Delta\sigma_{SS}$, $\Delta\sigma_{GB}$, and $\Delta\sigma_{dispersoids}$, are the contributions of solid solution strengthening, grain/subgrain boundary strengthening, and the Mn-dispersoid strengthening.

The contribution of the solid solution is mainly from Mg solutes. Assume that all Mn atoms are consumed in the dispersoids, and the solid solution effect of other alloying elements is negligible due to their lower content. After heat treatment and hot rolling, most of Mg-containing phases dissolved and only primary Mg_2Si exist. Given the volume fraction and the composition of the primary Mg_2Si phase, the concentration of the Mg element in the α-Al solid solution could be estimated (Table 5.4). The strengthening contribution from the solid solution of Mg could be calculated according to Eq (4) [6].

$$\Delta\sigma_{ss} = HC_{Mg}{}^{\alpha} \qquad (4)$$

where C was the concentration of solute atoms wt.%, H_{Mg} =13.8 MPa/wt.%, α_{Mg} = 1.14.

Using Eq. 4 and the data in Table 5.4, the strengthening effect caused by Mg solute are 45.7 and 47 MPa for the samples with 3S- and Ind-treatments, respectively, as shown in Table 5.6 and Fig. 5.10.

Table 5.4: The volume fraction and the average Mg solid solution in Al matrix

	Volume fraction of Mg_2Si	Average Mg in solid solution, wt.%
3S	0.37	2.86
Ind	0.21	2.93

The contribution of Mn-dispersoids could be explained by Classical Orowan strengthening bypassing mechanism due to their large size [37, 38]. Assuming that, the size and volume fraction of Mn-dispersoids did not change during cold rolling and annealing, where there was no driving force for coarsening. Therefore, the contribution of Mn-dispersoids on the YS could be estimated using the following equation.

$$\Delta\sigma_{dispersions} = \frac{0.84MGb}{2\pi\sqrt{(1-\upsilon)}\,\lambda}\ln\left(\frac{r}{b}\right) \qquad \lambda = r\left(\sqrt{\frac{2\pi}{3V_f}}\right) \tag{5}$$

Where M =3 is the Taylor facto, G =27.4 GPa is the shear modulus of Al matrix at room temperature, b =0.286 nm is the Burgers vector, υ is the Poisson's ratio (υ =0.33), λ is the effective interparticle spacing, and r and V_f are the radius and volume fraction of Mn-dispersoids.

By substituting the data of Table 5.2 in Eq. 5, the contribution of Mn-dispersoids could be estimated, and the results are listed in Table 5.6 and Fig. 5.10. It can be seen then the contribution of Mn-dispersoids to the YS after 3S-heat treatment is two times that after Ind-heat treatment, owing to their higher number density and finer size (Table 5.2 and Fig 5.2). For instance, the Mn-dispersoids provided an increment of 90.1 MPa to the YS after 3S-treatment compared to 45.5 MPa after Ind-treatment.

The contribution of grain boundary strengthening to the YS was predicted using equation (6) [39]:

$$\Delta\sigma_{GB} = \frac{K_y}{\sqrt{d_{HAGs}}} + M\alpha G\sqrt{1.5bS_v\theta_{ave}^{LAB}f_{LAB}} \tag{6}$$

Where K_y Hall–Petch constant for alloy Al-3Mg equals 0.12 MPa.$m^{0.5}$ [40]. The term d_{HAB} is the average grain size of recrystallized grains (HAGBs, the angle higher than 15 °). The term α = 0.3 is a constant, G is the shear modulus (27.4 GPa), b is the Burgers vector (0.286 nm), and M=3 is the Taylor factor. The term $S_v = (\frac{4}{\pi} B_A)$ where B_A is the total boundary length per unit area (2-D micrograph). The terms (θ_{ave}^{LAB} and f_{LAB}) are the average misorientation angle of the LABs and the fraction of the LABs, respectively [39].

The parameters in Eq. 6 could be obtained from EBSD micrographs after hot and cold rolling, (Fig. 5.5 and 5.8), as listed in Table 5.5. The cut-off misorientation angle is setting for LABs and HABs to be 15°, below which is considered as LABs where the boundary contribution increases with increasing the misorientation angle [39]. Given the measured parameters and substituting in Eq. 6, the contribution of the grain boundary could be estimated, as shown in Table 5.6.

Table 5.5: Grain structure parameters based on EBSD micrographs for the experimental conditions

Rolling	Hot	Cold	Hot	Cold	Hot	Cold	Hot	Cold
	$\mathbf{d_{HABs}}$, μm		$\mathbf{f_{LAGBs}}$		$\boldsymbol{\theta_{ave}^{LAB}}$(°)		$\boldsymbol{S_v}$=4/π*$\mathbf{B_A}$	
3S-treatment	19.6	8.3	0.37	0.25	4.78	4.51	0.623	0.235
Ind-treatment	30	11.1	0.28	0.05	4.59	7.05	0.500	0.195

Table 5.6 displays the calculated YS increments of different strengthening components. It is evident that introducing a higher number density of finer dispersoids through the modified 3S-heat treatment results in the highest YS increment, reflecting the importance of Mn-dispersoid on the mechanical properties of Al-3Mg-0.8Mn alloy. In addition, fine

recrystallized grain due to the strong pining effect of dispersoids with corresponded large grain boundary area became an important strengthening mechanism at room temperature, increasing the YS increment [41]. Therefore, Mn-dispersoids are considered the primary strengthening component (90.1 MPa), followed by the influence of grain boundary and Mg solid solution. On the other hand, owing to the lower number density and larger size of dispersoids in the samples after the Ind-heat treatment (Fig. 5.2), the contribution of Mn-dispersoids and Mg solid solution and grain boundary are comparable. Fig. 5.10 compares the predicted and experimentally measured YSs for the experimental alloys. Generally, the predicted YS value follows the same trend as the experimental measurement results, showing the importance of Mn-dispersoids for improving the mechanical properties.

According to the above findings, controlling the characteristics of Mn-dispersoids in terms of the size, number density and volume fraction before hot rolling significantly impacts the mechanical properties and the recrystallization resistance during hot/cold rolling and subsequent annealing. However, during the hot rolling at relatively high temperature, the Mn-dispersoids become coarsening, as shown in Fig. 5.4. Therefore, it is crucial to avoid the coarsening of Mn-dispersoids in preserving the deformed grain structure after cold rolling and annealing, leading to superior mechanical properties.

Table 5.6: Predicted YS contributions and experimentally measured YS (MPa)

	Hot Rolling		Cold Rolling	
	3S	**Ind**	**3S**	**Ind**
Al matrix (1100-O)	34	34	34	34
Mg solid solution	45.7	47.0	45.7	47.0
Mn-dispersoids	90.1	45.5	90.1	45.5
Grain boundary	44.0	34.8	49.9	40.4
Predicted YS	213.8	161.3	219.7	166.9
Experimental results	196.1	149.8	233.6	179.5

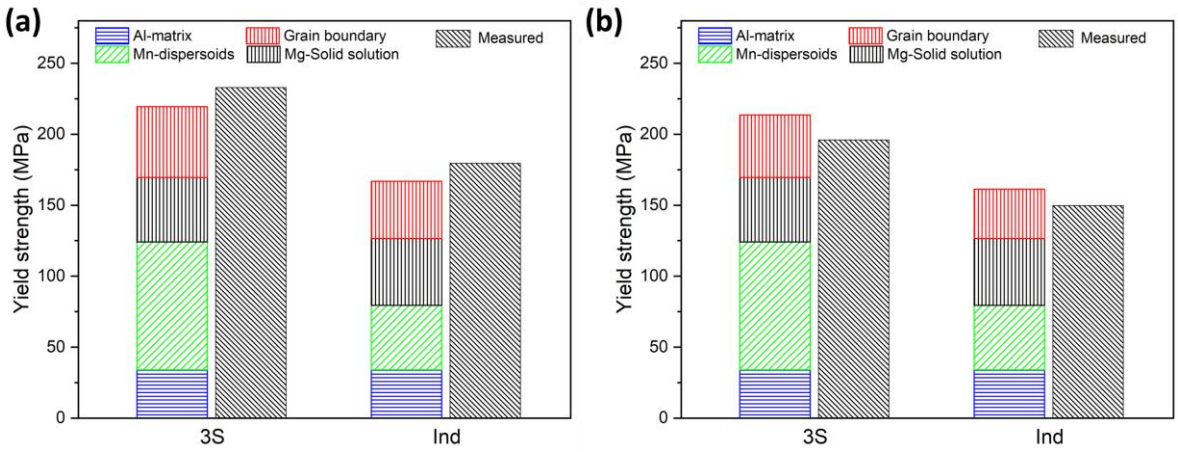

Figure 5.10: Comparison between predicted and experimental yield strengths under (a) hot rolling and (b) cold rolling.

5.4 Conclusions

1. During the heat treatment process, a number of Mn-bearing dispersoids precipitated in the dendrite cell/gain interiors. The high number density of Mn-bearing dispersoids with

fine size and low fraction of dispersoid free zone can be promoted with a modified low-temperature three-step heat treatment.

2. After hot rolling, the number density of dispersoids decreases, and their size increases, owing to the higher deformation temperature and interaction with dislocations. However, the samples subjected to the modified three-step heat treatment exhibited a higher number density and finer size of Mn-bearing dispersoids than those with the industrial heat treatment.
3. The mechanical properties of hot and cold rolled sheets subjected to the modified three-step heat treatment prior rolling were significantly improved compared to the conventionally industrial heat treatment. The yield strength of hot rolled and annealed sheets after the modified heat treatment reached 196 MPa, showing an improvement of 30% relative to the base industrial heat treatment. Furthermore, the yield strength of cold-rolled and annealed (300 ^{o}C/1hr) sheets reached 233 MPa, representing an improvement of 29.6% over the samples with the base industrial heat treatment, reflecting the importance of Mn-dispersoids on improving the mechanical properties of Al-3Mg-0.8Mn alloy.
4. The recrystallization resistance of both hot and cold rolled and annealed sheets was greatly improved the modified three-step heat treatment owing to the better dispersoid characteristics.
5. The yield strengths in two cases as example - after hot rolling and annealing (300^{o}C/5h) and cold rolling and annealing (300^{o}C/1h) - was quantitatively analyzed using constitutive equations to understand the contribution of various strengthening

mechanisms. The predicted yield strengths were in good agreement with the experimentally measured values.

Acknowledgments

The authors would like to acknowledge the financial support from the Natural Sciences and Engineering Research Council of Canada (NSERC) and Rio Tinto Aluminum under the Grant No. CRDPJ 514651-17 through the Research Chair in Metallurgy of Aluminum Transformation at the University of Quebec at Chicoutimi.

5.5 References

[1] S. Court, K. Gatenby, D. Lloyd, Factors affecting the strength and formability of alloys based on Al–3 wt.% Mg, Materials Science and Engineering: A 319 (2001) 443-447.
[2] J.R. Davis, Aluminum and Aluminum Alloys, Light Metals and alloys (2001) 66-66.
[3] J. Hirsch, Aluminium in innovative light-weight car design, Materials transactions 52(5) (2011) 818-824.
[4] J.A.V.D. Hoeven, L. Zhuang, A New 5xxx Series Alloy Developed for Automotive Applications, SAE TECHNICAL PAPER SERIES (724) (2002) 1-8.
[5] H. Fang, H. Liu, Y. Yan, Y. Li, X. Xu, X. Chu, Y. Lu, K. Yu, Microstructural and textural evolution of Al-4.5 Mg-0.7 Mn-0.2 Sc alloys during hot rolling, Materials Letters 292 (2021) 129600.
[6] E. Huskins, B. Cao, K. Ramesh, Strengthening mechanisms in an Al–Mg alloy, Materials Science and Engineering: A 527(6) (2010) 1292-1298.
[7] L. Tang, X. Peng, J. Huang, A. Ma, Y. Deng, G. Xu, Microstructure and mechanical properties of severely deformed Al-Mg-Sc-Zr alloy and their evolution during annealing, Materials Science and Engineering: A 754 (2019) 295-308.
[8] J. Hirsch, Aluminium Sheet Fabrication and Processing, Fundamentals of Aluminium Metallurgy: Production, Processing and Applications, R. Lumley, Ed, CSIRO, Australia, Woodhead Publishing Ltd., UK, 2010.
[9] O. Engler, Z. Liu, K. Kuhnke, Impact of homogenization on particles in the Al-Mg-Mn alloy AA 5454-Experiment and simulation, Journal of Alloys and Compounds 560 (2013) 111-122.
[10] H.J. McQueen, S. Spigarelli, M.E. Kassner, E. Evangelista, Hot deformation and processing of aluminum alloys, CRC press2011.
[11] C. Li, K. Liu, X. Chen, Improvement of elevated-temperature strength and recrystallization resistance via Mn-containing dispersoid strengthening in Al-Mg-Si 6082 alloys, Journal of Materials Science & Technology 39 (2020) 135-143.

[12] M. Mofarrehi, M. Javidani, X.-G. Chen, Effect of Mn content on the hot deformation behavior and microstructure evolution of Al–Mg–Mn 5xxx alloys, Materials Science and Engineering: A (2022) 143217.
[13] O. Engler, K. Kuhnke, J. Hasenclever, Development of intermetallic particles during solidification and homogenization of two AA 5xxx series Al-Mg alloys with different Mg contents, Journal of Alloys and Compounds 728 (2017) 669-681.
[14] Y. Li, W. Zhang, K. Marthinsen, Precipitation crystallography of plate-shaped Al6 (Mn, Fe) dispersoids in AA5182 alloy, Acta materialia 60(17) (2012) 5963-5974.
[15] M. Osman, O. Engler, K. Karhausen, L. Löchte, A. McLaren, Effect of homogenisation conditions on recrystallisation in Al–Mg–Mn alloy AA 5454, Materials science and technology 23(6) (2007) 688-698.
[16] Y. Wang, B. Yang, M. Gao, R. Guan, Deformation behavior and dynamic recrystallization during hot compression in homogenized Al–6Mg–0.8 Mn alloys, Materials Science and Engineering: A 840 (2022) 142953.
[17] A.Y. Algendy, K. Liu, X.G. Chen, Evolution of dispersoids during multistep heat treatments and their effect on rolling performance in an Al-5 % Mg-0 . 8 % Mn alloy, Materials Characterization 181(September) (2021) 111487-111487.
[18] H. Huang, F. Jiang, J. Zhou, L. Wei, M. Zhong, X. Liu, Hot deformation behavior and microstructural evolution of as-homogenized Al–6Mg–0.4 Mn–0.25 Sc–0.1 Zr alloy during compression at elevated temperature, Journal of Alloys and Compounds 644 (2015) 862-872.
[19] Z.H. Bai, B.H. Luo, The Effects of Annealing Temperature on the Microstructure and Properties of Cold-Rolled 5083 Aluminum Alloy, Advanced Materials Research, Trans Tech Publ, 2011, pp. 784-789.
[20] X. Fang, G. He, M. Ruiz, C. Zheng, Y. Wang, Z. Li, Y. Zhu, Influence of annealing parameters on the mechanical properties of heterogeneous lamella structured 5083 aluminum alloy, Letters on Materials 9(4s) (2019) 556-560.
[21] J. Wang, J. Xu, F. Pan, Effect of annealing on microstructure and properties of Er modified 5052 alloy, Results in Physics 10 (2018) 476-480.
[22] J.R. Davis, Aluminum and aluminum alloys, ASM international1993.
[23] K.M. Gatenby, J. Creek, D. Kang, S.K. Das, (12) Patent Application Publication (10) Pub . No .: US 2016 / 0355915 A1, 1(19) (2016).
[24] K. Liu, X.G. Chen, Development of Al-Mn-Mg 3004 alloy for applications at elevated temperature via dispersoid strengthening, Materials and Design 84 (2015) 340-350.
[25] S.M. Allen, Foil thickness measurements from convergent-beam diffraction patterns, Philos. Mag A 43(2) (1981) 325-335.
[26] A.Y. Algendy, K. Liu, X.G. Chen, Formation of intermetallic phases during solidification in Al-Mg-Mn 5xxx alloys with various Mg levels, MATEC Web of Conferences 326 (2020) 02002-02002.
[27] M. Cabibbo, E. Evangelista, M. Vedani, Influence of severe plastic deformations on secondary phase precipitation in a 6082 Al-Mg-Si alloy, Metallurgical and Materials Transactions A 36(5) (2005) 1353-1364.
[28] I. Lomaev, E. Elsukov, On the analysis of the mechanisms of the strain-induced dissolution of phases in metals, PHYSICS OF METALS AND METALLOGRAPHY C/C OF FIZIKA METALLOV I METALLOVEDENIE 102(2) (2006) 186.

[29] J. Rakhmonov, K. Liu, P. Rometsch, N. Parson, X.G. Chen, Effects of Al(MnFe)Si dispersoids with different sizes and number densities on microstructure and ambient/elevated-temperature mechanical properties of extruded Al–Mg–Si AA6082 alloys with varying Mn content, Journal of Alloys and Compounds 861 (2021) 157937-157937.
[30] C. Li, K. Liu, X.-G. Chen, Improvement of elevated-temperature strength and recrystallization resistance via Mn-containing dispersoid strengthening in Al-Mg-Si 6082 alloys, Journal of Materials Science & Technology 39 (2020) 135-143.
[31] Z. Guo, G. Zhao, X.-G. Chen, Effects of two-step homogenization on precipitation behavior of Al3Zr dispersoids and recrystallization resistance in 7150 aluminum alloy, Materials Characterization 102 (2015) 122-130.
[32] X. Qian, N. Parson, X.-G. Chen, Effects of Mn content on recrystallization resistance of AA6082 aluminum alloys during post-deformation annealing, Journal of Materials Science & Technology 52 (2020) 189-197.
[33] J.X. Wu, C. Gao, R.Y. Huang, Z.S. Liu, P.Z. Zhao, Effect of Cold Deformation and Annealing on Microstructure and Mechanical Properties of 5083 Aluminum Alloy Sheets, Materials Science Forum, Trans Tech Publ, 2018, pp. 49-54.
[34] P. Ebenberger, P.J. Uggowitzer, B. Gerold, S. Pogatscher, Effect of compositional and processing variations in new 5182-Type AlMgMn alloys on mechanical properties and deformation surface quality, Materials 12(10) (2019) 1645.
[35] Ø. Ryen, B. Holmedal, O. Nijs, E. Nes, E. Sjölander, H.-E. Ekström, Strengthening mechanisms in solid solution aluminum alloys, Metallurgical and Materials Transactions A 37(6) (2006) 1999-2006.
[36] Z. Li, Z. Zhang, X.G. Chen, Improvement in the mechanical properties and creep resistance of Al-Mn-Mg 3004 alloy with Sc and Zr addition, Materials Science and Engineering A 729(December 2017) (2018) 196-207.
[37] A.J. Ardell, Precipitation hardening, Metallurgical Transactions A 16(12) (1985) 2131-2165.
[38] J. Qin, Z. Zhang, X.G. Chen, Mechanical Properties and Strengthening Mechanisms of Al-15 Pct B4C Composites with Sc and Zr at Elevated Temperatures, Metallurgical and Materials Transactions A: Physical Metallurgy and Materials Science 47(9) (2016) 4694-4708.
[39] M. Zha, Y. Li, R.H. Mathiesen, R. Bjørge, H.J. Roven, Microstructure evolution and mechanical behavior of a binary Al–7Mg alloy processed by equal-channel angular pressing, Acta Materialia 84 (2015) 42-54.
[40] D. Lloyd, S. Court, Influence of grain size on tensile properties of Al-Mg alloys, Materials science and technology 19(10) (2003) 1349-1354.
[41] A.H. Chokshi, Grain boundary processes in strengthening, weakening, and superplasticity, Advanced Engineering Materials 22(1) (2020) 1900748.

Chapter 6: Conclusions and recommendations

General conclusions

In this project, the precipitation behavior of dispersoids under various heat treatments and microallying with Sc was systematically investigated. The evolution of rolling performance, mechanical properties at both room and elevated temperature as well as the recrystallization resistance with dipsersoids was evaluated. The following conclusions can be reached from experimental data and analyses:

1. During all heat treatments, a number of Mn-dispersoids with various morphologies were observed in the dendritic cells and grains. The dispersoids' size, number density, and distribution strongly depended on the heat treatment parameters/practice. Depending on the chemical composition and morphology, two different Mn-bearing dispersoids were identified as Al_4Mn and Al_6Mn, with a cube- and rod-like morphology, respectively.
2. Multistep heat treatments showed higher microhardness and a more significant fraction of dispersoid zones (DZ) than single-step treatments. However, two-step heat treatment at lower temperatures (2S-LT, 275 °C/12 h + 375 °C/48 h) introduced the highest density of Mn-dispersoids with the finest size among all heat treatments, but severe defects were created during the hot rolling process. Therefore, a modified three-step heat treatment (3S-LT54, 275 °C/12 h + 375 °C/48 h + 500 °C/4 h) is applicable to produce Al-Mg-Mn alloy sheet metal with a higher density of dispersoids.
3. Compared to conventional one-step heat treatment, the mechanical properties of rolled sheets subjected to the three-step heat treatment (3S-LT54) were remarkably improved,

providing a promising way to improve the mechanical properties of non-heat-treatable 5xxx wrought alloys.

4. With Sc and Zr addition, the average grain size was slightly decreased, whereas the volume fraction of primary Mg_2Si and Fe/Mn-rich intermetallics significantly increased.
5. During the three-step heat treatment, two populations of strengthening particles (AlMn dispersoids and $Al_3(Sc,Zr)$ precipitates) precipitated in the Sc/Zr-containing alloys. In addition, the density of Mn-dispersoids decreased by 46%, and their size increased with Sc and Zr addition. During hot rolling at 500 °C, the AlMn dispersoids and $Al_3(Sc,Zr)$ precipitates coarsened, and their density decreased.
6. The tensile properties of the rolled sheets at 25–200 °C were significantly improved with increasing Sc and Zr content, owing to the strong pining effect of $Al_3(Sc,Zr)$ precipitate. However, the YSs of the Sc/Zr-containing alloys at high temperatures (300–400 °C) drop at lower values than the base alloy, most likely due to dislocation losses and the accelerating of dynamic recrystallization (DRX) as a result of Sc/Zr additions and more preferred grain boundary sliding (GBS) during the hot-tensile.
7. The mechanical properties of both base and Sc/Zr-containing alloys were thermally stable during long-term thermal exposure at 300 °C for 500 h, indicating the great potential of this alloy for various elevated-temperature applications.
8. The YS contributions at 25 °C and 300 °C of the different strengthening mechanisms were quantitatively analyzed using the constitutive equations, and the predicted YSs were compared with experimentally measured values. The analytical predicted YSs at 25 ^{o}C were in good agreement with the experimentally measured values. By contrast, there was a discrepancy between the predicted and the measured YSs at 300 ^{o}C, particularly in Sc-

containing alloys, predominantly due to the GBS softening mechanism based on the EBSD results.

9. By increasing the Sc content (0.43 wt.%), a higher density of rod-like $Al_3(Sc,Zr)$ discontinuous precipitates (DCP) were formed during solidification with fan-and-line aggregation concentrated along the dendrite cell boundaries. The length of these precipitates ranged from 500 to 860 nm. Such discontinuous precipitation rarely occurred in the low Sc containing alloy (L-Sc).
10. During heat treatment, two types of precipitates (Mn-dispersoids and spherical $Al_3(Sc,Zr)$ precipitates were formed as the main strengthening phases. In case of high Sc alloy, the discontinuous precipitates were partially dissolved, and their length decreased to 200-350 nm. Furthermore, the density of spherical $Al_3(Sc,Zr)$ in high Sc was reduced because the discontinuous precipitates consumed much available Sc and Zr in the solid solution. As a result, the microhardness in high Sc alloy was lower than in low Sc alloy.
11. Both precipitates and dispersoids underwent coarsening during hot rolling with a complete dissolution of the discontinuous precipitates. The number density of spherical $Al_3(Sc,Zr)$ was less with larger size in high Sc than those in the low Sc alloy. The tensile properties were significantly improved in Sc-containing alloys, owing to the additional strengthening effect of spherical $Al_3(Sc,Zr)$ precipitates. However, both YS and UTS decreased by increasing Sc content, proving the negative impact of discontinuous precipitates. The low Sc alloy exhibited the highest YS and UTS, showing an improvement of 30% in YS and 11.8% in UTS relative to the base alloy.
12. The tensile properties of hot/cold rolled, and annealed sheets subjected to a modified 3S-heat treatment significantly improved compared to the Ind-heat treatment. The YS of

Al-3Mg alloy reached 196.1 and 233 MPa after hot and cold rolling, respectively, showing an improvement of 30% and 29.6% over samples with Ind-heat treatment at the same condition with a lower elongation.

13. A novel three-step heat treatment displays a higher recrystallization resistance after hot and cold rolled sheets than the conventional one-step heat treatment. Samples with 3S have a lower recrystallization fraction of 23% with a lower fraction of HAGB (28.3%) than Ind-heat treatment after hot rolling/annealing. After cold rolling and annealing (300 ^{o}C/1h), the recrystallization fraction of samples with 3S reached 60%, which is lower than the Ind-heat treatment of 79%.

Recommendations

Based on the recent findings of this study, the following recommendations could be given for future work in this area.

1. In the present study, the maximum Cu addition was added to the studied alloy considering that it would improve the precipitation of Mn dispersoids as reported in AA3xxx. However, all Cu was almost consumed in forming the low melting phase τ-Al_6CuMg_4 during solidification. Therefore, it would be better to lower the Cu content as possible to improve the rollability.
2. The Mn-dispersoids significantly improved the mechanical properties of Al-Mg-Mn alloy. Therefore, the addition of Cadmium (Cd) and Indium (In) to Al-Mg-Mn alloys might be interesting since the microalloying of these elements could improve the precipitation behavior of dispersoids (AA3xxx and AA6xxx); Hence, further improving the mechanical properties of Al-Mg-Mn alloy mat be expected.
3. Based on the recent study, reducing the rolling temperature to 400–425 °C is challenging to obtain a better synergetic strengthening effect of precipitated particles by reducing their coarsening rate. Hence, it is necessary to optimize the deformation process at lower temperature.
4. Sc and Zr addition negatively affect the precipitation behavior of Mn-dispersoids, lowering their synergetic effect on the mechanical properties. Therefore, solving this problem is interesting for further improving the mechanical properties of Al-Mg-Mn alloys.
5. The current study suggested that the benefit of Sc/Zr additions in improving the mechanical properties is limited to 200 ^{o}C in Al-Mg-Mn (AA5083) alloy. After 200 ^{o}C,

the Sc-addition has a negative impact on the mechanical properties by accelerating DRX and GBS as proposed. Therefore, further microstructure investigation during the tensile test is interested to understand the role of Al_3(Sc, Zr) precipitates on the mechanical properties at high temperatures.

6. There is a discrepancy between the predicted and experimental measured YS in the current study of Sc-containing alloy, mainly due to the GBS softening mechanism. Modifying the constitutive equations would be a hot topic for analytical calculations, considering the effect of grain size at a higher temperature.
7. In addition, Sc is cost-effective and then substituting the expensive Sc with other alloying elements such as Erbium (Er), Yttrium (Y), and Dysprosium (Dy) might be interesting since the microalloying of these elements has a positive effect on the creep resistance.

Appendix I: The general description of sample preparation before rolling

Fig. I.1 describes the general processing fabrication before hot rolling from the casting. As shown in Fig. I.1a, the alloys were first cast in a preheated steel permanent mold at 250 °C. to obtain cast ingots from Y-block (Fig. I.1a). Then the samples were scalped and cut into two rectangular cubes (Fig. I.1b). Subsequently, the homogenization process was carried out in the electrical resistance furnace, including single and multistep heat treatment. Before hot rolling, the homogenized samples were preheated at 500 °C/1.5h; the hot rolling process was performed in several passes, by which the thickness decreased from 26.5mm to 3.2 mm. It should be mentioned that the temperature of the samples was kept at 440-500 °C during the hot rolling process. The following sections will discuss detailed information on the hot rolling process.

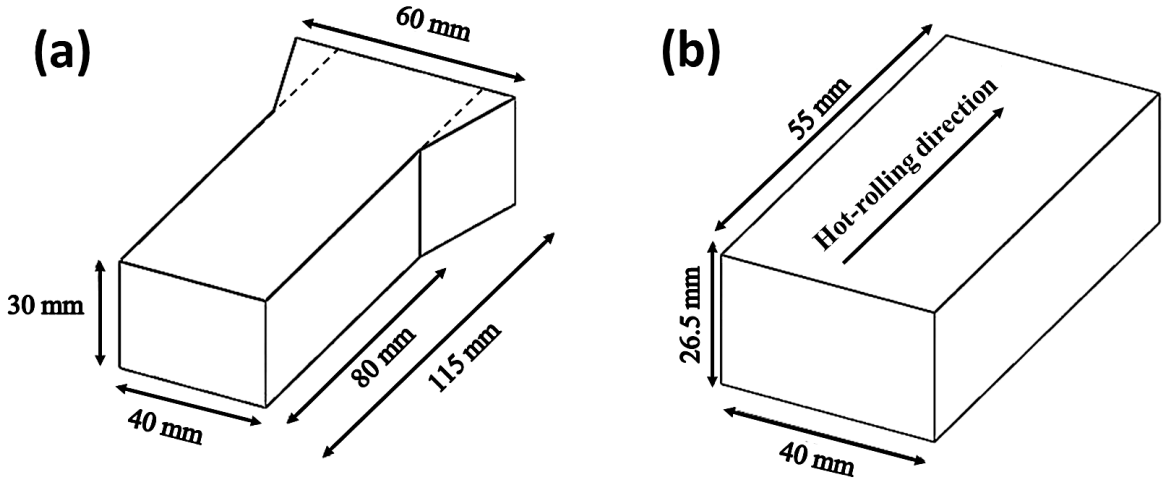

Figure I.1: (a) Casting the alloys in the shape of a Y-block; (b) Scalping (1.75mm from each side) and cut into two rectangular blocks (26.5mm×40mm×55 mm)

Appendix II: Supporting information for Chapter 2

The detailed description of the hot rolling process used in the first article is summarized in Table II.1. The samples underwent the final thickness in 10 passes within approximately 3 hrs. The final hot-rolled sheet with 3.2mm×42mm×380 mm, as shown in Fig. II.1

Table II.1: the detailed description of the hot rolling process

Starting Thickness	26.5 mm	**Furnace temperature**	500 ^{o}C
Rolling temperature	(460-500 ^{o}C)		
Total reduction	88%		
Passes	Thickness after rolling, mm	Reduction, mm	Holding Temperature, min
1	23.3	3.2	20
2	20.1	3.2	20
3	18.5	1.6	20
4	16.9	1.6	20
5	15.3	1.6	20
6	13.7	1.6	20
7	12.1	1.6	20
8	8.9	3.2	20
9	5.7	1.6	20
10	3.2	2.5	

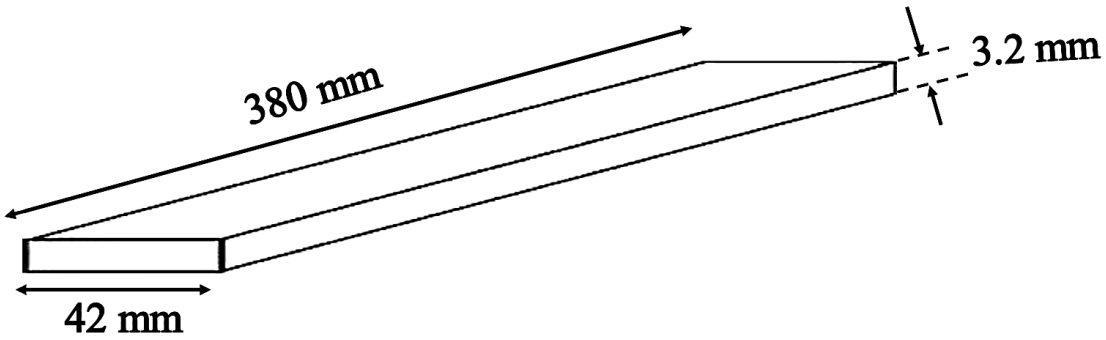

Figure II.1: Schematic for the final hot-rolled sheet.

Table II.2 displays the chemical analysis of various IMCs observed in in the as cast structure of Al5Mg0.8Mn alloy. The various types of Mn-Fe IMCs have been confirmed with the aid of SEM-EBSD phase identification, and the results were presented in Fig. II.2.

Table II.2: SEM-EDS results for various intermetallic phases found in as-cast microstructure of experimental alloys

Intermetallic phases		**Element, wt.%**							
		Mn	**Fe**	**Si**	**Mg**	**Cu**	**Cr**	**Ti**	**Al**
Mn-Fe IMCs	$Al_m(Fe,Mn)$	8.9	12.1	0	0	0	0	0	Bal.
	$Al_6(Mn,Fe)$	11.6	11.4	0	0	0	0	0	Bal.
	α-Al(Fe,Mn)Si	11.6	11.2	4.4	0	0	0	0	Bal.
	ε-$Al_{18}(Cr,Mn)_2Mg_3$	11.3	0	0	11.1	0	4.6	0	Bal.
	τ-Al_6CuMg_4	0	0	0	20.5	12.9	0	0	Bal.
	Mg_2si	0	0	15.8	18.4	0	0	0	Bal.
	$Al_7(Cr,Ti)$	0	0	0	11.0	0	7.9	5.8	Bal.

Fig. II.2 shows the various Fe/Mn intermetallics in the as-cast structure of the studied alloy. The mean angular deviation (MAD) between the observed and calculated patterns indicates the accuracy of the solution given by the software (Channel 5). A smaller value of MAD means a higher accuracy between the experimental and simulated patterns. For a desirable accurate solution, the MAD value should be at least lowly than 0.7.

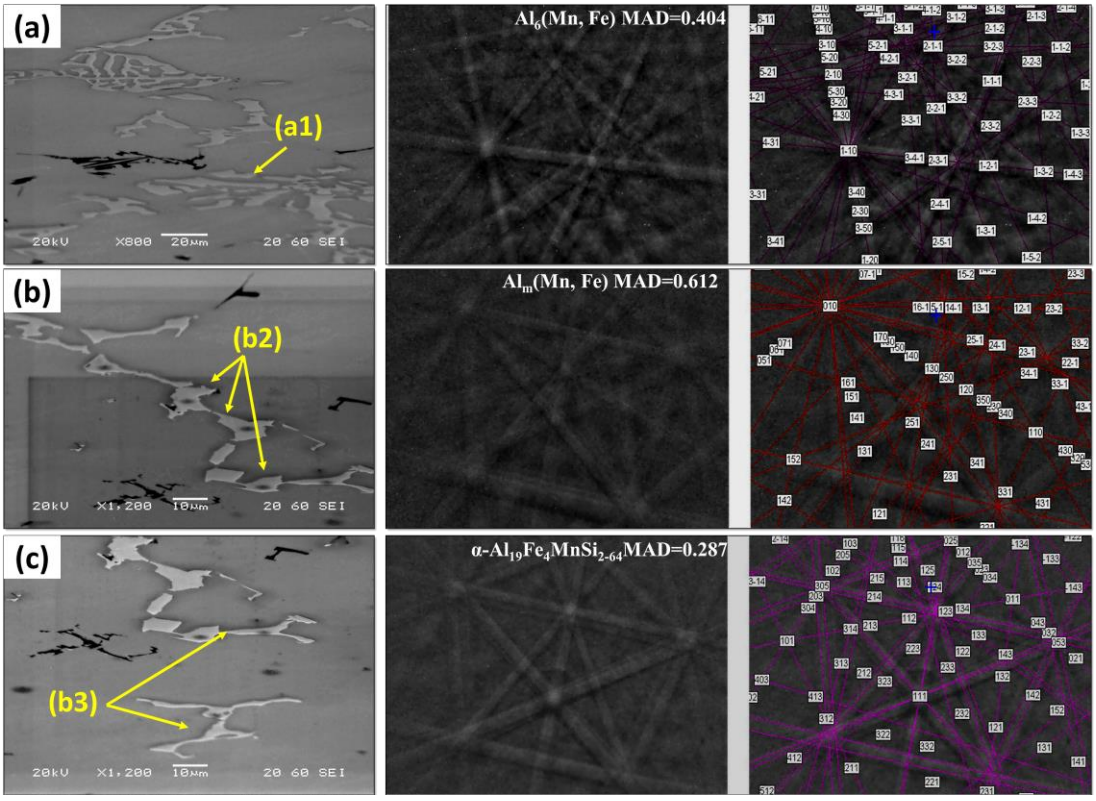

Figure II.2: SEM Micrographs and EBSD patterns of alloy M5 showing different Fe/Mn intermetallic phases with corresponding patterns and simulated results

Fig. II.3 displays the typical bright-field TEM image of the alloy after the hot rolling process and the characteristics of dispersoids, showing the coarsening of Mn-dispersoids.

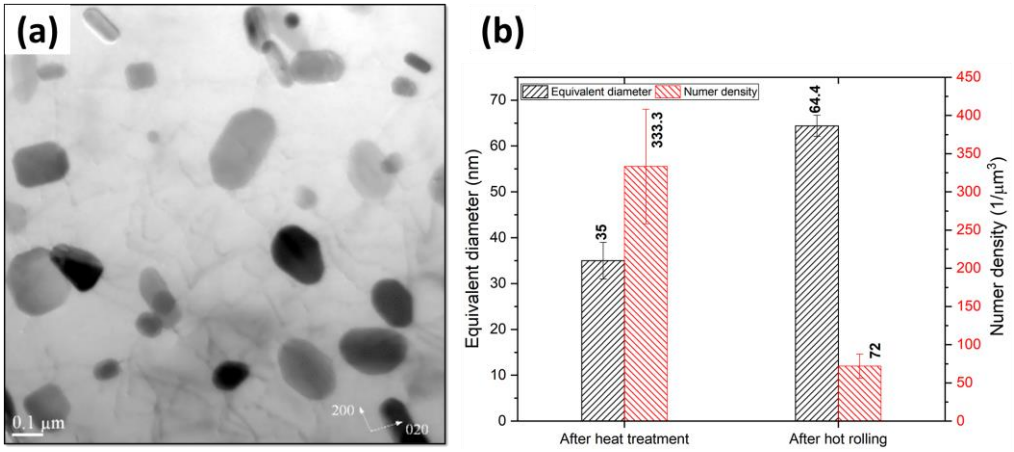

Figure II.3: (a) Typical bright-field TEM image along [001]Al and (b) characteristics of Mn-dispersoids before and after rolling

Appendix III: Supporting data for Chapter 3

The hot rolling parameters in this chapter were modified to avoid the coarsening of the dispersoids. The modifications include lower roll speed, the reduction rate, and lower times back to the furnace, as in Table III.1.

Table III.1: The modified hot rolling parameters

Starting Thickness	26.5 mm	**Furnace temperature**	500 ^{o}C
Rolling temperature	(430-500 ^{o}C)		
Total reduction	88%		
Passes	Thickness after rolling, mm	Reduction, mm	Holding Temperature, min
1	23.3	3.2	20
2	18.5	4.8	20
3	13.7	4.8	20
4	10.5	3.2	20
5	7.3	3.2	20
6	5.7	1.6	20
	3.2 mm	2.5	15

Fig. III.1 displays the typical bright-field TEM of studied alloys during the first step of heat treatment at 275 ^{o}C/12h, showing a lower density of β'-Mg_2Si could be formed in B15 alloy than alloy B.

Fig. III.2 shows the distribution of the Mn-dispersoids in alloy B and B15 at the beginning of the second step of heat treatment at 375 ^{o}C/6h. As a result, alloy B without Sc shows a higher density of fine Mn-dispersoids than alloy with Sc. In addition, In alloy with Sc, there is a coalescence of dispersoids in the same direction of previously formed β'Mg_2Si, as marked by a circle. Besides, a large number of nanosized Al_3(Sc, Zr) precipitates were observed in the dark field image with 1-2 nm.

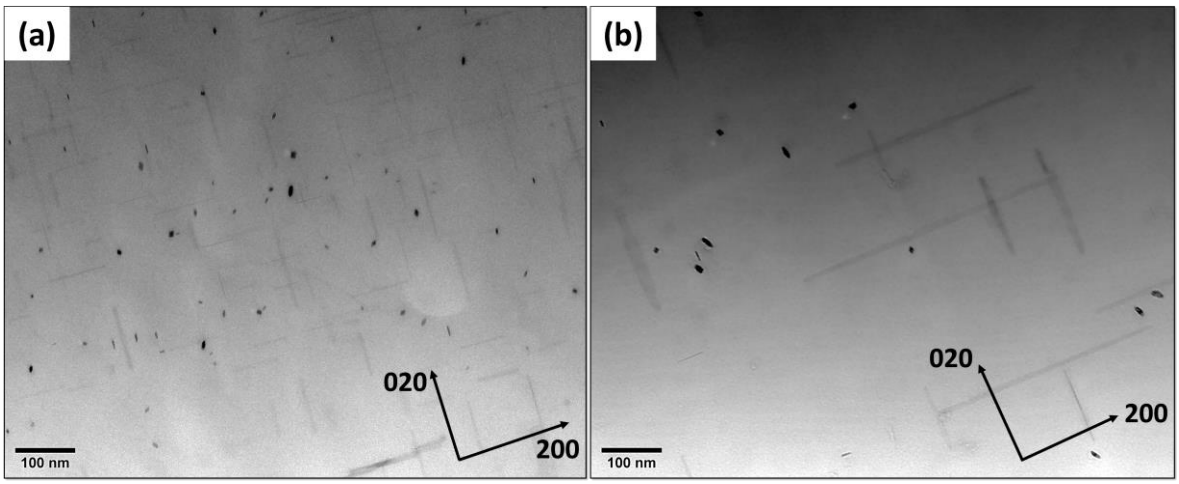

Figure III.1: Bright-field TEM image after the first heat treatment stage (275 °C/12h) of (a) alloy B (Sc-free) and (b) alloy B15

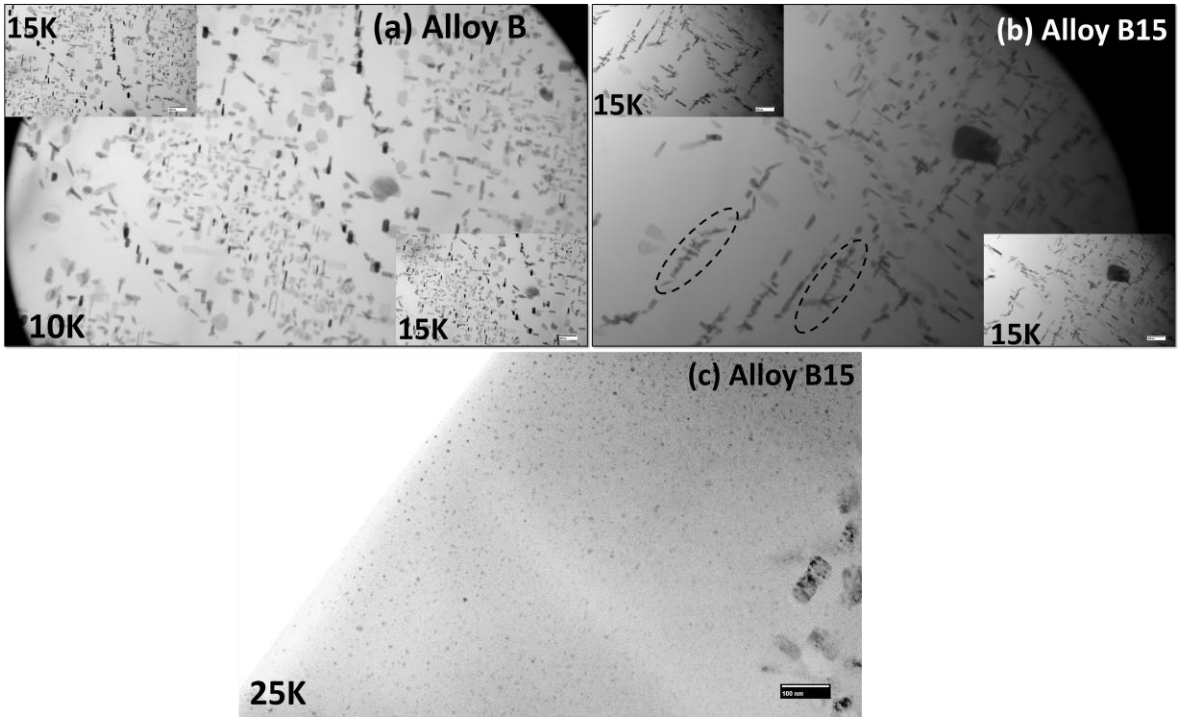

Figure III.2 : Bright-field TEM image after 275 °C/12h+375 °C/6h of (a) alloy B (Sc-free) and (c, b) alloy B15

Figure III.3 displays the EBSD Euler orientation and Quality maps of alloy B15 after hot tensile at 300 °C with different step sizes of localized area, revealing the features of the deformed samples. As shown in Fig. III.3, fine-recrystallized grains (less than 10 µm) are distributed close to the GBs formed during the hot-tensile from DRX.

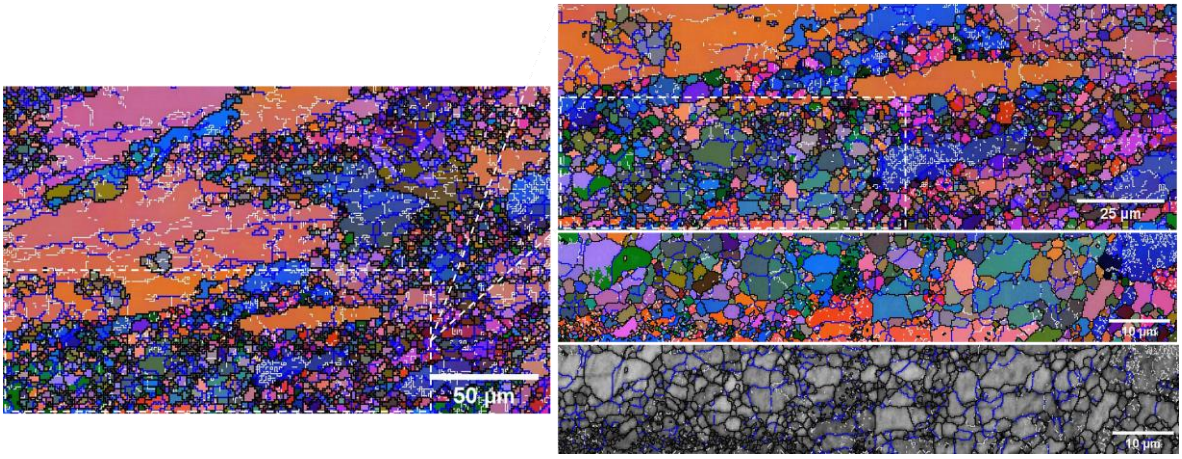

Figure III.3: EBSD Euler orientation and Quality maps of alloy B15 after hot-tensile at 300 °C, showing the features of the deformed samples with different step sizes.

Appendix IV: Supporting data for article 4

Fig. IV.1 displays the electrical conductivity (EC) and the microhardness (HV) measurements of as-cast samples. The minimum EC was recorded for alloy SZ15, indicating a higher solid solution level than the other alloys. By increasing the Sc content to 0.4 wt.%, the EC raises again, which is unexpected, confirming the observation of DCP in the as-cast sample. On the other hand, the microhardness increases with Sc addition, indicating the grain refinement effect, as shown in Fig. IV.2. Fig. IV.2 displays the microstructure of the studied alloys before and after heat treatment. After heat treatment, the grain boundaries (Fig. IV. 2f) are remarkably irregular compared with the straight ones observed in the base and SZ15 alloy Fig. IV.2e. The irregularity phenomenon indicates the migration of grain boundaries during the heat treatment.

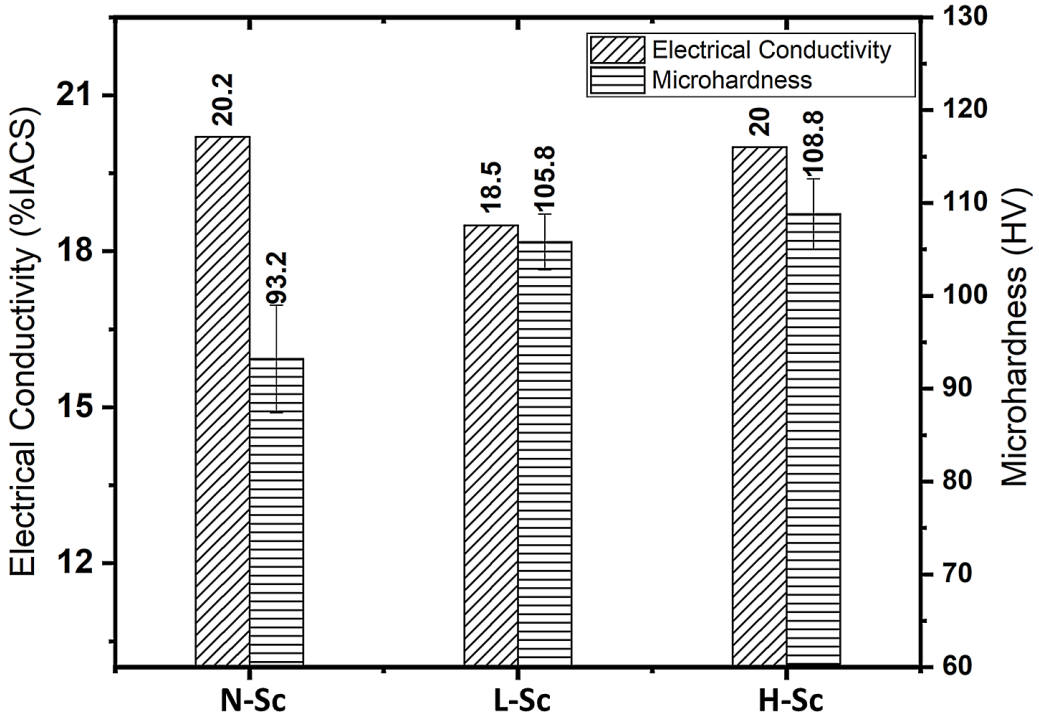

Figure IV.1: The microhardness (HV) and electrical conductivity (EC) measurements of the as-cast alloys

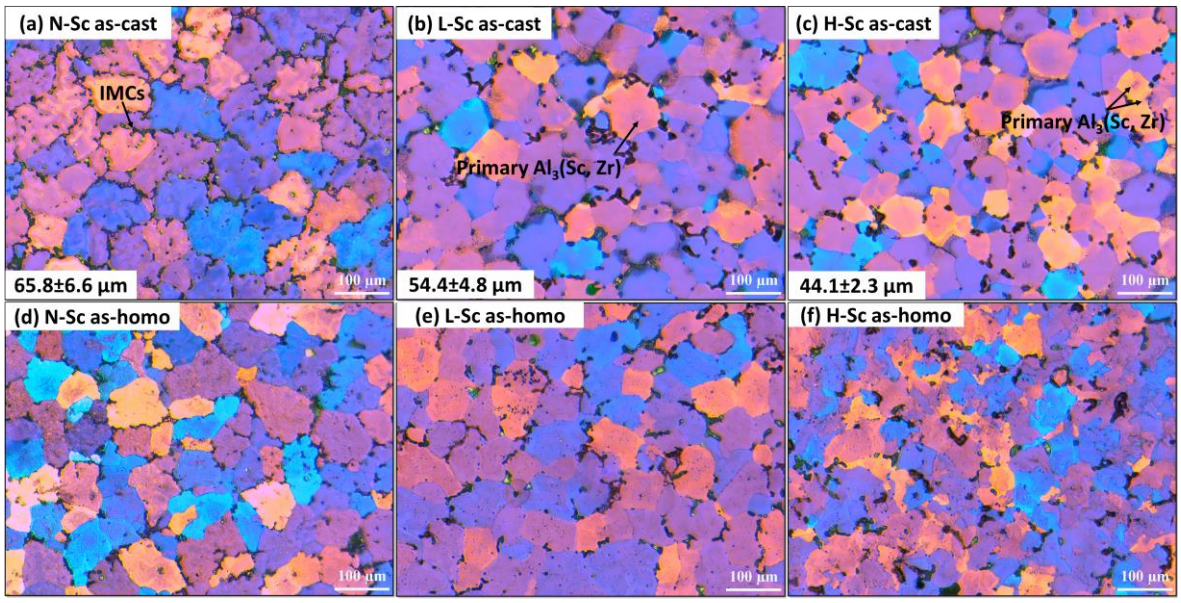

Figure IV.2: The grain structure of the experimental alloys (a, b, c) before and (d, e, f) after heat treatment

List of the publications

Journal and conference papers:

1. Formation of intermetallic phases during solidification in Al-Mg- Mn 5xxx alloys with various Mg levels, “Ahmed Y. Algendy, Kun Liu, X.-Grant Chen” **MATEC Web of Conferences 326, 02002 (2020).**
2. Evolution of dispersoids during multistep heat treatments and their effect on rolling performance in an Al-5% Mg-0.8% Mn alloy, “Ahmed Y. Algendy, Kun Liu, X.-Grant Chen” – **Material Characterization (181), 2021, 111487.**
3. Effects of AlMn dispersoids and Al3(Sc,Zr) precipitates on the microstructure and ambient/elevated-temperature mechanical properties of hot-rolled AA5083 alloys, “Ahmed Y. Algendy, Kun Liu, X.-Grant Chen” –submitted to **Material Science and Engineering A.**
4. Evolution of Discontinuous/Continuous Al_3(Sc,Zr) Precipitation during Thermomechanical Process and its Impact on Tensile Properties in Al-Mg-Mn 5083 Alloy, “Ahmed Y. Algendy, Kun Liu, X.-Grant Chen”– **Material Characterization (192), 2022, 112241.**
5. Evolution of microstructure and dispersoids in Al-Mg 5xxx alloys under wire + arc additive manufacturing and permanent mold casting, “Kun Liu, Ahmed Y. Algendy, X.-Grant Chen” **The Minerals, Metals & Materials Society 2021 TMS 2021.**
6. Role of Mn-bearing dispersoids on the tensile properties, and recrystallization resistance of Al-3Mg-0.8Mn rolled alloy, “Ahmed Y. Algendy, Kun Liu, X.-Grant Chen”-under internal review**.**

Posters

1. Evolution of Dispersoids during Heat Treatment of Al-Mg Alloys with Different Mg Levels, “Ahmed Y. Algendy, Kun Liu, X.-Grant Chen”–REGAL Students’ Day, Chicoutimi, Canada, October. 2019.
2. Evolution of microstructure and dispersoids in Al-Mg 5xxx alloys under wire + arc additive manufacturing and permanent-mold casting, “Ahmed Y. Algendy, Kun Liu, X.-Grant Chen”–REGAL Students’ Day, Chicoutimi, Canada, Novmber. 2020.
3. Evolution of Microstructure and Mechanical Properties of AA5083 Alloy by Sc and Zr Microalloying, “Ahmed Y. Algendy, Kun Liu, X.-Grant Chen”–REGAL Students’ Day, Chicoutimi, Canada, Novmber. 2021.